metals

MDPI

Review

Recent Advances in Additive Manufacturing of High Entropy Alloys and Their Nuclear and Wear-Resistant Applications

Sonal Sonal [1] and Jonghyun Lee [1,2,*]

[1] Department of Mechanical Engineering, Iowa State University, Ames, IA 50011, USA; sonal@iastate.edu
[2] Division of Materials Science and Engineering, Ames Laboratory, Ames, IA 50011, USA
* Correspondence: jolee@iastate.edu

Abstract: Alloying has been very common practice in materials engineering to fabricate metals of desirable properties for specific applications. Traditionally, a small amount of the desired material is added to the principal metal. However, a new alloying technique emerged in 2004 with the concept of adding several principal elements in or near equi-atomic concentrations. These are popularly known as high entropy alloys (HEAs) which can have a wide composition range. A vast area of this composition range is still unexplored. The HEAs research community is still trying to identify and characterize the behaviors of these alloys under different scenarios to develop high-performance materials with desired properties and make the next class of advanced materials. Over the years, understanding of the thermodynamics theories, phase stability and manufacturing methods of HEAs has improved. Moreover, HEAs have also shown retention of strength and relevant properties under extreme tribological conditions and radiation. Recent progresses in these fields are surveyed and discussed in this review with a focus on HEAs for use under extreme environments (i.e., wear and irradiation) and their fabrication using additive manufacturing.

Keywords: high entropy alloys (HEAs); additive manufacturing (AM); wear; nuclear applications; irradiation

Citation: Sonal, S.; Lee, J. Recent Advances in Additive Manufacturing of High Entropy Alloys and Their Nuclear and Wear-Resistant Applications. *Metals* **2021**, *11*, 1980. https://doi.org/10.3390/met11121980

Academic Editor: Babak Shalchi Amirkhiz

Received: 26 October 2021
Accepted: 1 December 2021
Published: 8 December 2021

1. Introduction

1.1. The History of High Entropy Alloys

Since the first copper-based alloy was developed around 7000 years ago, numerous metallic alloys have been utilized in various applications [1]. In traditional alloying engineering, the principal metal is used as a matrix to incorporate other alloying elements as solute. In most cases, alloying has been done to improve the strength and hardness of ductile metals. Until now, around 30 alloy systems have been introduced, based on the principal element alloying concept [2]. Increasing demands for advanced materials under harsher environments led to the innovative alloying strategies which improved the performance of existing materials against high temperatures, impact, fatigue fracture, corrosion, or wear. Heat treatments have also been used along with alloying to tailor the properties of materials for desired applications. In the 1970s, a new class of materials, named intermetallics, were developed to increase the specific hot hardness. In 1980s, another class of materials named super-alloys were developed. Inconel, Waspalloy, Hastelloy, MP35N, MP98T, Rene alloys, TMS alloys and CMSX single crystal alloys are widely used commercial superalloys. Figure 1 shows how engineering materials evolved over human history. In the beginning of the 21st century, when the alloying technology reached maturity and so did the capability of materials for more advanced applications, a new alloying concept emerged. These alloys were initially called by several different names, such as multi-principal elements alloys, equi-molar alloys, equi-atomic ratio alloys, substitutional alloys and multicomponent alloys. The most common name of these alloys is high

entropy alloys (HEAs) given by J. W. Yeh [3], because these alloys have higher mixing entropy in their liquid or solid solution states than any other alloying systems. Attractive structural properties, wide composition ranges and higher probability to find simpler microstructures enabled HEAs to gain rapidly growing attention from researchers. HEAs are considered one of three innovations in the alloying techniques along with bulk metallic glasses and metal rubbers [2].

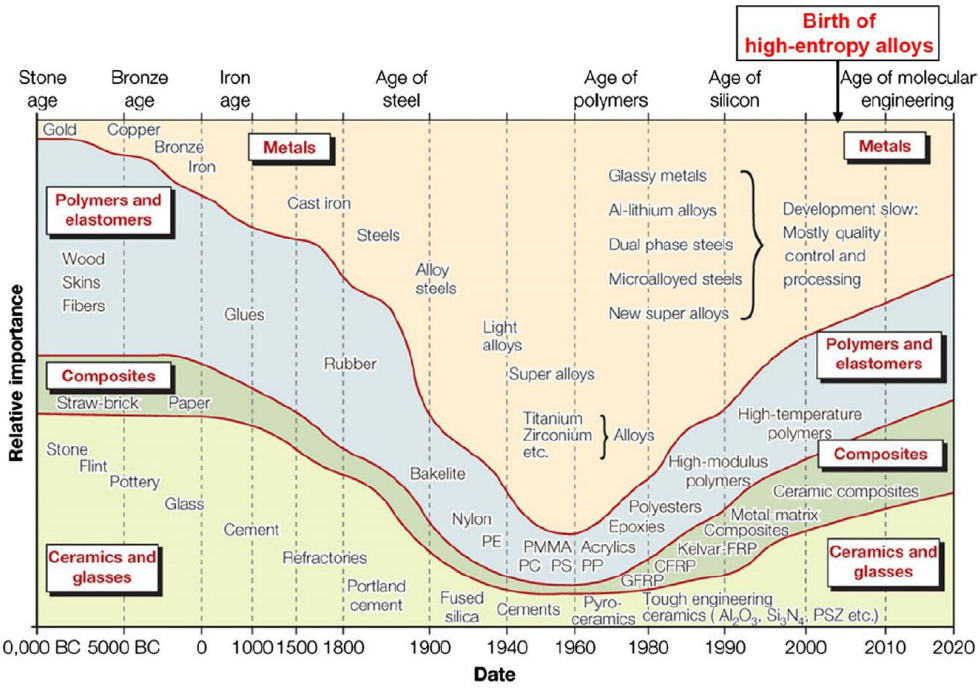

Figure 1. Evolution of Engineering Materials [2].

The Germen scientist Franz Karl Archard could be called the predecessor for HEAs research [2]. In the 18th century, Archard studied equi-mass multicomponent alloys containing five to seven different elements from Fe, Sn, Pb, Zn, Bi, Ag, Co, Sb, As and Cu. He tested these compositions for ductility, hardness, impact resistance, wear and density, etc. He published his work in a French book entitled, *Recherches sur les propriétés des alliages métalliques* [4,5]. In 1981, Brian Cantor and his student Alain Vincent started to work on Archard's idea again at University of Sussex in Sussex, England [6]. They explored various equi-molar combinations out of 20 different elements and found that the CoCrFeMnNi alloy formed a single face-centered cubic (FCC) structure. In another independent research (MS thesis of National Tsing Hua University, Taiwan, 1996 [7]), J. W. Yeh developed different HEAs based on a concept that high entropy of an alloy system reduces the number of phases that appear in the final product. S. Ranganathan is another notable pioneering researcher in the field who wrote a review paper on the concept of HEAs and talked about the possibility of fabricating HEAs in 2003 [8]. In 2004, two independent studies by Cantor et al. [9] and Yeh et al. [3] introduced the concept of HEAs properly with the experimental results. They developed metallic alloys having nearly equi-atomic composition of more than five elements.

The basic idea of HEAs is to use five or more principal elements in or near equi-atomic compositions. According to the Gibbs phase rule, the number of phases increases with the increasing number of elements. Most of these phases are expected to be intermetallics due to their strong negative enthalpies. Binary/ternary phase diagrams also indicate that an alloy having several principal elements would develop several phases including brittle intermetallics, resulting in complex microstructures which will limit their practical

applications [8,10]. For instance, Cu-Zn, Al-Cu and Al-Cu-Zn phase diagrams have 5, 13 and 20 intermetallics or intermediate phases, respectively [11]. By this reasoning, scientists had been reluctant to work with equi-atomic or near-equi-atomic composition made of several principal elements. This notion began to change as it was observed that the number of phases in HEAs was far less than predicted by the Gibbs phase rule [12]. The high configurational entropy of HEAs allowed for forming solid solutions rather than intermetallics, and thus, resulted in much simpler microstructures [3,9]. The main hypothesis to explain the much smaller number of phases in HEAs is that by forming an atomic configuration of high randomness (high entropy, ΔS), the Gibbs free energy of the system will be lowered ($\Delta G = \Delta H - T\Delta S$), and therefore, the formation of intermetallics is thermodynamically suppressed [3,13,14].

The performance of a HEA is difficult to predict as it often depends on the complicated interactions among the constituents instead of the rule of mixtures. Hence, the characterization of structure and stability under operational conditions is important before putting them into practical applications. Most of the literature mentions HEAs have been developed by "trials and errors" with an aim to get a single phase. The properties of HEAs are then compared to those of traditional alloys. For example, the wear resistance of $FeCo_{1.5}CrNi_{1.5}Ti$ and $FeAl_{0.2}Co_{1.5}CrNi_{1.5}Ti$ was reported to be higher by a factor of two compared to that of steels [15].

Since 2004, two books [2,11] and thousands of research papers on HEAs of numerous compositions have been published. Most of the review papers focused on basic understanding and development [12,13,15–26], four core effects [27,28], physical metallurgy [14], design strategies [29–31], phase stability [32,33], or thermodynamics [34] and microstructures [35–39]. As research on the properties of HEAs progressed, various research groups reviewed the mechanical performances [40–42], heat resistance [43,44], magnetic [45] and physical properties of HEAs [46,47]. As synthesis techniques for HEAs advanced, various reviews on simulations and modeling [48,49], fabrication methods [50,51], welding techniques [52–55], high pressure technology [56] were published. Due to the possibility of having a wide composition range, new HEAs and their properties were reported continuously beyond the existing literature. In recent years, more reviews focused on diffusion studies [57], deformation behavior [58,59], corrosion [60,61], fracture and fatigue [62,63], defects and radiation resistance [64–66], refractory HEAs [67], HEAs composites [68] and ceramics [69] were published. Moreover, high entropy alloys have applications in different fields such as biomedical [70,71], energy [72], wear [73,74], nuclear [75,76] and creep [63], corrosion [60,77–79].

In this context, this paper discusses as illustrated in Figure 2 recent updates on the fabrication of HEAs by additive manufacturing (AM) and the HEAs for applications under extreme environments (i.e., wear behavior and nuclear applications). Moreover, unlike previous reviews on these topics, this review would provide more convenience to readers who have just stepped in this field as well, since the reviewed research publications on AM, wear behavior and nuclear applications of HEAs are enlisted in a detailed tabular form with their results. Section 2 discusses additive manufactured HEAs in terms of their composition, microstructure and their mechanical properties, such as ultimate tensile strength (UTS), tensile elongation (ε), yield strength (YS), hardness (H), compressive strength (CS), compressive yield strength (CYS) and the amount of compression (C). In Section 3, the behaviors of HEAs under ion irradiation are analyzed in terms of dislocation, microstructure, irradiation resistance, hardness, phase stability, swelling resistance and self-healing. Furthermore, the tribological studies of HEAs are surveyed in terms of HEAs content variation, particle reinforcement, media and nitriding/carburizing/sulfurizing, in comparison with conventional materials. The wear behaviors of HEAs at higher temperatures and oxides formation are also reviewed.

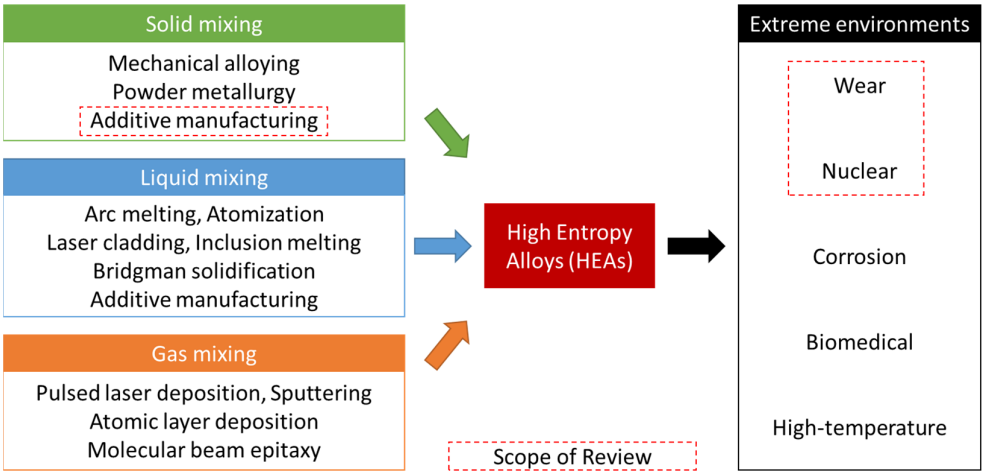

Figure 2. HEAs manufacturing methods and extreme environment applications. The scope of review includes recent advances in additive manufacturing of HEAs and their applications for wear-resistant and nuclear materials.

In this context, this paper discusses recent updates on the fabrication of HEAs by additive manufacturing (AM) and the HEAs for applications under extreme environments (i.e., wear behavior and nuclear applications). Moreover, unlike previous reviews on these topics, this review would provide more convenience to readers who have just stepped into this field as well, since the reviewed research publications on AM, wear behavior and nuclear applications of HEAs are listed in a detailed tabular form with their results. Section 2 discusses additive manufactured HEAs in terms of their composition, microstructure and their mechanical properties, such as ultimate tensile strength (UTS), tensile elongation (ε), yield strength (YS), hardness (H), compressive strength (CS), compressive yield strength (CYS) and the amount of compression (C). In Section 3, the behaviors of HEAs under ion irradiation are analyzed in terms of dislocation, microstructure, irradiation resistance, hardness, phase stability, swelling resistance and self-healing. Furthermore, the tribological studies of HEAs are surveyed in terms of HEAs content variation, particle reinforcement, media and nitriding/carburizing/sulfurizing, in comparison with conventional materials. The wear behaviors of HEAs at higher temperatures and oxides formation are also reviewed.

1.2. The Definitions of High Entropy Alloys

The first ever definition of HEA was given by Yeh et al. [3] as a class of alloys composed of five or more principal elements having concentration between 5% to 35% for each element. The second definition was also proposed by the same group [13]. In the second definition, the three categories of alloys were introduced on the basis of the configurational entropy: low entropy alloys (configurational entropy alloys (ΔS_{conf}) ≤ 0.69R), medium entropy alloys (0.69R ≤ ΔS_{conf} ≤ 1.61R) and high entropy alloys (ΔS_{conf} ≥ 1.61R) [30], where R is the universal gas constant. Here, the low entropy alloys are mostly conventional alloys with one or two major elements and the medium entropy alloys have two to four major elements. The high entropy alloys contain five or more major elements. The second definition does not require equi-atomic composition. For example, $Ti_2ZrHfV_{0.5}Mo_{0.2}$ [80], $FeCoNiCrTi_{0.2}$ [81] and $Al_{0.1}CoCrFeNi$ [82,83] are categorized as HEAs according to the second definition.

Moreover, these definitions are not strict, and it is not clarified which one should be used to categorize an alloy. For example, an alloy having composition of 5% A, 5% B, 20% C, 35% D and 35% E has the configuration entropy of 1.36R according to Equation (1) derived from Boltzmann's entropy formula [30].

$$\Delta S_{conf} = -R[c_1 \ln c_1 \dots \dots \dots c_n \ln c_n] \quad (1)$$

where c_n is the atomic fraction of the nth element. In case of equi-atomic composition, Equation (1) reduces to [30]:

$$\Delta S_{conf} = R\ln(n) \quad (2)$$

For example, an alloy having 25 components with equi-atomic concentration has $\Delta S_{conf} = R\ln(n = 25) = 3.22R$. This material has the concentration of each element out of the range suggested by the first definition (between 5% to 35%), but it has sufficiently high entropy according to the second definition [15].

Considering both definitions together may often be confusing. In the past, researchers have also limited HEAs to have equi-atomic compositions or single-phase microstructures [26]. HEAs lack a standard definition that embraces all possible conditions. Both definitions are used frequently but neither clarifies the conditions of its usage. Generally, a metallic alloy with multiple principal elements and high configurational entropy is considered as a HEA.

2. Manufacturing of HEAs

2.1. Background and Conventional Methods

Brian Cantor estimated the total number of possible metallic alloys with different compositions to be up to around 1078 [12]. This means many new alloys are yet to be discovered. For the manufacturing of HEAs, the initial synthesis strategy was to choose equi-atomic concentration of principle elements to maximize the entropy of the system. However, later, HEAs in non-equi-molar ratios were also developed for various applications. Arc melting was mostly preferred to produce HEAs thanks to its convenience, availability and simplicity. Furthermore, developing a HEA became more complex as more non-equi-atomic compositions were considered and several other manufacturing techniques were used. Alshataif et al. [84] covered almost all kinds of processing techniques used so far for HEAs synthesis. They detailed solid state processing (i.e., powder atomization methods, ball milling, cold/hot pressing, sintering, spark plasma sintering), liquid state processing (i.e., arc melting, vacuum induction melting, directional solidification, infiltration, electromagnetic stirring), thin film deposition (i.e., magnetron sputtering, pulsed laser deposition, plasma spray deposition) and additive manufacturing. Most of these manufacturing techniques are commercially available. That means most HEAs would not require a special manufacturing process and mass-producing HEAs would be possible with the existing alloying technologies and facilities.

The influence of process parameters, such as temperature and pressure, on the properties of HEAs were also studied. The effects of temperature on the properties of HEAs were studied through processes such as: annealing and heat treatments [85–104] and thermomechanical processing [105–108]. A number of research groups reported how temperature affected the microstructures and mechanical properties of HEAs in various manufacturing processes [96,109–112]. Moreover, the physical or chemical responses of various HEAs under a variety of thermal histories during manufacturing were studied: thermal aging behavior [86,113–115], TaNbHfZrTi synthesis by hydrogenation–dehydrogenation reaction and thermal plasma treatment [116], martensite formation [117–120], Al_x-CoCrFeNi formation with high gravity combustion from oxides [121], laser surface melting [122], precipitation behavior [123–126] and WTaMoNbV synthesis using inductively coupled thermal plasma [127].

Researchers have also attempted to alter the microstructures and properties of HEAs by high pressure treatments. Regulating pressure during fabrication of HEAs can considerably alter the interaction between the atoms by changing the interatomic distance, bonding nature and packing densities. These changes often convert the microstructures and affect the mechanical and structural properties. Dong et al. [56] reviewed the applications

of high pressure technology for HEAs. They reviewed the use of dynamic high pressure, diamond anvil cells, high pressure torsion and hexahedron anvil press. Zhang et al. [128] reviewed high pressure induced phase transitions in HEAs. Application of high pressure torsion [37,129–142] is more frequent than other pressure techniques [136,143–150].

Furthermore, various researchers successfully welded/brazed HEAs [52–55,151]. Guo et al. [52] reviewed arc welding, laser welding, electron beam welding, friction stir welding to join HEAs and conducted the microstructural analysis on the welded structures. Filho et al. [54] gave a general review on the properties of welded HEAs parts and Tillmann et al. [151] reviewed HEAs brazing. Lopez et al. [53] reviewed fusion based welding (i.e., for CoCrFeNiMn and other related HEA systems) and solid state welding. Scutelnicu et al. [55] reviewed friction stir, electron and laser beam, tungsten inert gas welding techniques for CoCrFeMnNi, AlCoCrCuFeNi, AlCrFeCoNi and CoCrFeNi alloys.

2.2. Additive Manufacturing of HEAs

3-D printing in manufacturing industries, when properly applied, not only makes a design phase more efficient and economic but also brings thoughtful impacts on product design. Recent advances in additive manufacturing (AM) made it more influential throughout the supply chain which generates revenue as well [152]. The additive manufactured HEAs showed improvement in their mechanical properties in comparison to as-cast HEAs [153–160]. Higher cooling rates in AM processes help suppress diffusional phase transformation and increase the chemical homogeneity of HEAs [161]. Under certain circumstances, AM gives a better control over the material processing and helps tailor application-specific microstructures which become more important for the parts for applications under extreme environments. For example, it was demonstrated that fine and tailorable microstructures in HEAs were obtained using AM techniques [162–169], which implies AM can improve the mechanical performance of at least some HEAs. However, this may not be a trivial task as a good understanding of the AM technique and material behavior during the AM process is required [170].

AM of HEAs has been discussed briefly in a few review papers [51,161,171,172] and books [2,173]. Xiaopeng Li [161] discussed the requirements and challenges of AM of HEAs and bulk metallic glasses. Chen et al. [51] examined the microstructural evolution and mechanical properties of AM-processed CoCrFeNi, Al_xCoCrFeNi, CoCrFeMnNi and $Ti_{25}Zr_{50}Nb_{50}Ta_{25}$. Fabricating HEAs by spark plasma sintering (SPS) and their property analyses were discussed in the book chapter "Spark Plasma Sintering of High Entropy Alloys" of [174]. SPS followed by mechanical alloying has largely been used to develop HEAs, which was reviewed in detail by Vaidya et al. [175]. Therefore, SPS studies are not included here.

In this review, studies on the AM of HEAs are tabulated and the mechanical properties of these HEAs are discussed. Tables 1–3 detail the HEAs synthesized by selective laser melting (SLM), electron beam melting (EBM) and direct energy deposition (DED), respectively. The performances of these HEAs are discussed in terms of their composition, their microstructure and their mechanical properties, such as ultimate tensile strength (UTS), % elongation at fracture (ε), yield strength (YS), hardness (H), compressive strength (CS), compressive yield strength (CYS), bending strength (BS), bending elongation (δ_b) and % compression at fracture (C).

Table 1. The compositions, microstructures and mechanical properties of SLM manufactured HEAs.

Source	Alloy Composition	Microstructure (Grain Size)	Result UTS (MPa), YS (MPa), BS (MPa), δ_b (mm), ε (%), H, CS (MPa), C (%)
Chen et al. [176]	CoCrFeMnNi	FCC (53.1 μm)	UTS = 281 ± 18, YS = 12.5 ± 0.5, H = 261 ± 7 HV
Niu et al. [169]	CoCrFeMnNi	FCC (<5 μm)	CS = 2447.7
Li et al. [177]	CoCrFeMnNi + TiNp nanoparticles	FCC	UTS = 601–1036, ε = 12–30
Li et al. [178]	CoCrFeMnNi + Fe based metallic glass	FCC	UTS = 916–1517
Li et al. [179]	CoCrFeMnNi + TiN nanoparticles	FCC	-
Kim et al. [180]	(CoCrFeMnNi)C	FCC (180–330 nm)	YS = 800–900, ε = 25–30
Li et al. [181]	CoCrFeMnNi + 12 wt% nano-TiNp	FCC (<2 μm)	UTS = 1100
Piglione et al. [182]	CoCrFeMnNi	FCC (0.52–0.64 μm)	H = 212 HV
Zhu et al. [153]	CoCrFeMnNi	FCC	-
Xu et al. [183]	CoCrFeMnNi	FCC (1–2 μm)	H = 2.84 ± 0.13 GPa
Park et al. [154]	CoCrFeMnNi +1 at%C	FCC (20–35 μm)	UTS = 829–989, YS = 741, ε = 24.3
Ren et al. [184]	CoCrFeMnNi	-	-
Dovgyy et al. [185]	CoCrFeMnNi	FCC & cubic (0.2–0.8 μm)	-
Zhou et al. [155]	CoCrFeNi + 0.5 at%C	FCC (40–50 μm)	UTS = 776–797, YS = 630–656, ε = 7.7–13.5
Wu et al. [186]	CoCrFeNi + 0.5 at%C	FCC (40–50 μm)	UTS = 795, YS = 638
Lin et al. [98]	CoCrFeNi	FCC	
Sun et al. [187]	CoCrFeNi	-, ~3 mm in length and ~200 μm in width	UTS = 676.7–691, YS = 556.7–572, ε = 12.4–17.9
Song et al. [188]	CoCrFeNi + N (1.8%)	FCC	UTS = 600–853, YS = 520–650, ε = 27
Zhou et al. [189]	$(CoCrFeNi)_{1-x}$ $(WC)_x$	FCC	H = 603–768 HV
Brif et al. [156]	CoCrFeNi	FCC	UTS = 480–745, YS = 402–600, ε = 8–32, H = 205–238
Niu et al. [190]	AlCoCrFeNi	Disordered (A2) + Ordered (B2) BCC	H = 632.8 HV
Karlsson et al. [170]	AlCoCrFeNi	FCC & BCC (<20 μm)	-
Peyrouzet et al. [157]	$Al_{0.3}$CoCrFeNi	FCC (width~13 and length~70–120 μm)	UTS = 896, YS = 730, ε = 29
Sun et al. [158]	$Al_{0.5}$CoCrFeNi	FCC & BCC (1 μm)	UTS = 878, YS = 609, H = 270HV
Zhou et al. [160]	$Al_{0.5}$CoCrFeNi	FCC	UTS = 721, YS = 579, ε = 22
Luo et al. [191]	AlCrCuFeNi	BCC (avg. width~4 μm)	CS = 1655.2–2052.8, C = 6.5–6.8
Luo et al. [192]	$AlCrCuFeNi_x$ ($2 \le x \le 3$)	FCC (thickness~490 nm) & BCC (~140 nm) Avg. thickness of both ~ 650 nm	UTS = 957, ε = 14.3
Li et al. [112]	AlCoCuFeNi	BCC	YS = 744, ε = 13.1, CS = 1600
Yao et al. [193]	AlCrFeNiV	FCC (width~15 μm, length~75–200 μm)	UTS = 1057.47, ε = 30.3
Wang et al. [194]	AlCoCrCuFeNi	FCC & BCC	H = 710.4 HV
Wang et al. [195]	AlMgScZrMn	Al3 (Sc, Zr) (1–10 nm + 7 μm)	UTS = 394, ε = 10.5
Sarawat et al. [196]	$AlCoFeNiV_{0.9}Sm_{0.1}$ $AlCoFeNiSm_{0.1}TiV_{0.9}$ $AlCoFeNiSm_{0.05}TiV_{0.95}Zr$, AlCoFeNiTiVZr	FCC	H~42.8–86.7 HV
Agrawal et al. [197]	$Fe_{40}Mn_{20}Co_{20}Cr_{15}Si_5$	HCP	UTS = 1100, YS = 530, ε = 30
Zhang et al. [198,199]	NbMoTaW	BCC (13.4 μm)	H = 826 HV
Yang et al. [200,201]	$Ni_6Cr_4WFe_9Ti$	FCC (300–1000 nm) + unknown phase	UTS = 972, YS = 742, ε = 12.2
Chen et al. [202]	CoCrFeNiMn	FCC + Mn_2O_3 particles	YS = 620, UTS = 730, ε~12
Litwa et al. [203]	CoCrFeNiMn	FCC	H~320 HV
Zhang et al. [204]	CoCrFeNiMn	FCC	YS~729.6
Kim et al. [205]	CoCrFeNiMn	FCC	YS = 752.6
Choi et al. [206]	CoCrFeNiMn	FCC	
Su et al. [207]	$CrCuFeNi_2$ $Al_{0.5}CrCuFeNi_2$ $Al_{0.75}CrCuFeNi_2$ $AlCrCuFeNi_2$	FCC FCC FCC + BCC/B2 FCC + BCC/B2	
Peng et al. [208]	CoCrFeNi + Ti coated diamond CoCrFeNi + diamond	FCC + diamond particles FCC + Cr7C3+ diamond particles	H = 622 HV, BS = 530, δ_b = 0.64 H = 615 HV, BS = 925, δ_b = 0.48
Wang et al. [209]	CoCrFeNiMn	FCC	H = 164–370 HV
Sun et al. [210]	$Al_{0.1}$CrCuFeNi	FCC	

	$Al_{0.5}CrCuFeNi$ AlCrCuFeNi	FCC FCC + BCC/B2 (NiAl)	
Ishimoto et al. [211]	$Ti_{1.4}Nb_{0.6}Ta_{0.6}Zr_{1.4}Mo_{0.6}$	BCC	YS = 1690,
Park et al. [212]	$(CoCrFeMnNi)_{99}C_1$	FCC	YS~741, UTS~874
Lin et al. [213]	CoCrFeNi	FCC	YS = 701 ± 14, UTS = 907 ± 25
Kim et al. [214]	CoCrFeNiMn	FCC	-
Jin et al. [215]	CoCrFeNiMn	FCC	YS = 520 ± 10, UTS = 770 ± 10, ε~25
Lin et al. [216]	$Al_{0.2}Co_{1.5}CrFeNi_{1.5}Ti_{0.3}$	FCC + σ + L12	YS = 1235, UTS = 1550
Peng et al. [217]	CoCrFeNiMn	FCC	-
Vogiatzief et al. [218]	$AlCrFe_2Ni_2$ Heat treatment (750–950 °C, 3 h & 6 h)	FCC + BCC	H = 276–483 HV
Liao et al. [219]	$Al_{0.5}FeCrNi_{2.5}V_{0.2}$	FCC	H = 220–240 HV
Guo et al. [220]	CoCrFeNiMn	FCC	YS = 622, UTS = 763, ε~16
Kim et al. [221]	$(CoCrFeNiMn)_{100-x}C_x$	FCC (15–22 μm)	YS = 653–753, UTS = 766–911
Zhao et al. [222]	CoCrFeNi	FCC	H = 238–525 HV
Gu et al. [223]	$CoCr_{2.5}FeNi_2TiW_{0.5}$	FCC	YS = 449–581, CS = 823–893, ε = 4.4–9.9, H = 436.7–499.2 HV

Table 2. The compositions, microstructures and mechanical properties of EBM manufactured HEAs.

Source	Alloy Composition	Microstructure (Grain Size)	Result UTS (MPa), YS (MPa), ε (%), H, CS (MPa), C (%)
Peng et al. [224]	CoCrFeNiMn	FCC	YS = 196
Wang et al. [225]	CoCrFeMnNi	FCC (65)	UTS = 497, 205, H = 157.1HV
Kuwabara et al. [226]	AlCoCrFeNi	BCC & FCC	UTS = 1073, YS = 769, ε = 0–1.2 YS = 944–1015, CS = 1447–1668, C = 14.5–26.4
Wang et al. [227]	AlCoCrFeNi	BCC	-
Fujieda et al. [228]	CoCrFeNiTi	FCC + Cubic	UTS = 1178, YS = 773, ε = 25.8
Popov et al. [229]	$Al_{0.5}CrMoNbTa_{0.5}$	BCC	

Table 3. The compositions, microstructures and mechanical properties of DED manufactured HEAs.

Scheme	Alloy Composition	Microstructure (Grain Size)	Result UTS (MPa), YS (MPa), ε (%), H, CS (MPa), C (%)
Guan et al. [230]	CoCrFeMnNi	FCC (13 μm)	YS = 517, ε = 26
Melia et al. [231]	CoCrFeMnNi	FCC (~4 μm)	UTS = 647–651, YS = 232–424
Li et al. [232]	CoCrFeMnNi	FCC	
Gao et al. [233]	CoCrFeMnNi	FCC (30–150 μm) + BCC	UTS = 620, YS = 448
Xiang et al. [234,235]	CoCrFeNiMn	FCC	UTS = 400–600
Chew et al. [236]	CoCrFeNiMn	FCC (3.68 ± 0.85 μm)	UTS = 660, YS = 518
Qiu et al. [237]	CoCrFeMnNi	FCC	UTS = 891, YS = 564
Li et al. [238]	CoCrFeMnNi + WC (0–10 wt%)	FCC	UTS = 550–845, YS = 300–675, ε = 9
Amar et al. [239]	CoCrFeMnNi + TiC (0–5 wt%)	FCC	UTS = 550–723, YS = 300–385, ε = 32
Guan et al. [240]	CoCrFeMnNi $AlCoCrFeNiTi_{0.5}$	FCC (24 μm) BCC (7 μm) + FCC	YS = 888–1100, H = 197–657 HV
Wang et al. [241]	$CoCrFeNiMo_{0.2}$	FCC	UTS = 532–928, ε = 37
Zhou et al. [242]	$CoCrFeNiNb_x$ (x = 0–0.2)	FCC	UTS = 400–820, YS = 220–750
Gwalani et al. [243]	AlxCoCrFeNi (x = 0.3–0.7)	FCC	
Nartu et al. [244]	$Al_{0.3}CoCrFeNi$	FCC	YS = 410–630, ε = 18–28
Mohanty et al. [245]	AlxCoCrFeNi (x = 0.3–0.7)	FCC + BCC	H = 170–380 HV
Vikram et al. [246]	AlCoCrFeNi2.1	FCC & BCC	YS = 309–711, H = 278 ± 11–316 ± 14 HV
Gwalani et al. [247]	$AlCrFeMoV_x$ (x = 0–1)	BCC (68–165 μm)	H = 485–581 HV
Guan et al. [248]	$AlCoCrFeNiTi_{0.5}$	BCC (12 μm)	-
Malatji et al. [249]	AlCrCuFeNi	BCC & FCC	H = 350 HV,
Dada et al. [250,251]	AlCoCrFeNiCu AlTiCrFeCoNi		H = 600 HV, H = 850 HV
Moorehead et al. [252]	NbMoTaW	BCC	-

Kunce et al. [253]	TiZrNbMoV	BCC	-
Dobbelstein et al. [254]	TiZrNbHfTa	BCC	H = 509 $HV_{0.2}$
Pegues et al. [255]	CoCrFeNiMn	FCC	-
Li et al. [256]	CoCrFeNiMn	FCC	-
Tong et al. [257]	CoCrFeNiMn Vacuum arc melting 1 impact Laser shock peening 3 impact Laser shock peening 5 impact Laser shock peening	FCC	YS = 320.7, UTS = 531.7 YS = 427.4, UTS = 570.7 YS~435, UTS~600 YS = 489.9, UTS = 639.9
Shen et al. [258]	CoCrFeNi $(SiC)_x$	FCC + Cr_7C_3 (1 μm)	UTS = 2155–2499, YS = 142–713, H = 139–310
Cai et al. [259]	CoCrFeNi AlCoCrFeNi	BCC (102.27 μm) BCC (18.75 μm)	YS = 318, UTS = 440, ε = 8.56 YS = 383, UTS = 533, ε = 10.6
Zhang et al. [260]	NbMoTa NbMoTaTi NbMoTaNi $NbMoTaTi_{0.5}Ni_{0.5}$	BCC BCC + α-Ti BCC BCC + Ni_3Ta + β-Ti	YS = 1252, CS = 1282, ε = 15 YS = 1200, CS = 1350, ε = 23 YS = 1350, CS = 1380, ε = 11 YS = 1750, CS = 2277.79, ε = 15 CS of $NbMoTaTi_{0.5}Ni_{0.5}$ at 600, 800 and 1000 °C is 1699.75 MPa, 1033.63 MPa and 651.36 MPa
Peng et al. [261]	$Al_{0.3}CoCrFeNi$	FCC + B2	YS = 373–476, CS = 473–508, ε = 0.6–2.96, H = 208–221 HV
Kuzminova et al. [262]	CoCrFeNi	FCC	YS = 456–551, UTS = 637–658, H = 209–259 HV
Malatji et al. [263]	AlCuCrFeNi Heat treated (800–1100 °C)	FCC + BCC	H = 310–381 HV
Dong et al. [264]	$AlCoCrFeNi_{2.1}$	FCC + BCC	YS = 388, UTS = 719, ε~27, H = 221–228
Zhou et al. [265]	$CoCrFeNb_{0.2}Ni_{2.1}$ Solution treatment (2 h,1250 °C) 96 h aged (650 °C)	FCC + HCP (Laves C14) + Nb rich carbide	YS~340, UTS~735 YS~239, UTS~607 YS~896, UTS~1127, ε~17
Zheng et al. [266]	CoCrFeNiMn	FCC	YS = 330, UTS = 630

Cantor alloy (i.e., CoCrFeMnNi) and its variants have been largely investigated. Apart from SPS, SLM is the most widely studied AM technique for HEAs [196–231]. HEAs that were successfully fabricated by SLM include CoCrFeNiMn [153,154,169,176–185,188,202–206,209,212,214,215,217,220,221], AlCrFeNiV [193], AlCoCrFeNi [170,190], AlCoCrCuFeNi [194], CoCrFeNi [98,155,186,187,189,208,213,222], $CoCr_{2.5}FeNi_2TiW_{0.5}$ [223], $Fe_{40}Mn_{20}Co_{20}Cr_{15}Si_5$ [197], $Al_xCoCrFeNi$ [157,158,160] AlCoCuFeNi [112,192], Al_x-CrCuFeNi [207,210], $AlCrCuFeNi_x$ [267], $AlCrFe_2Ni_2$ [218], $Al_{0.2}Co_{1.5}CrFeNi_{1.5}Ti_{0.3}$ [216], $Ni_6Cr_4WFe_9Ti$ [200], $Ti_{1.4}Nb_{0.6}Ta_{0.6}Zr_{1.4}Mo_{0.6}$ [211], $Al_{0.5}FeCrNi_{2.5}V_{0.2}$ [219] and NbMoTaW [198,199].

Meanwhile, EBM was used to manufacture CoCrFeNiMn [225], AlCoCrFeNi [226,227], CoCrFeNiTi [228] and $Al_{0.5}CrMoNbTa_{0.5}$ [229]. DED techniques were used to fabricate CoCrFeNiMn [230–240,255–258,266], CoCrFeNi [258,259,262], $Al_{0.3}CoCrFeNi$ [261], $CoCrFeNiMo_{0.2}$ [241], $CoCrFeNiNb_x$ [242], $Al_xCoCrFeNi$ [243–245,259,264], $AlCoCrFeNi_{2.1}$ [246,264], $AlCrFeMoV_x$ [247], AlCoCrFeNiTi$_{0.5}$ [248], AlCrCuFeNi [249,263], AlCoCrFeNiCu/AlTiCrFeCoNi [250,251], NbMoTaW [252], TiZrNbMoV [253], $NbMoTaTi_xNi_x$ [260], $CoCrFeNb_{0.2}Ni_{2.1}$ [265] and TiZrNbHfTa [254].

The microstructures and mechanical behaviors of the HEAs produced by different AM processes are still under investigation by several research groups. The HEAs listed in Tables 1–3 mainly have either FCC or BCC microstructures except $Co_{20}Cr_{15}Fe_{40}Mn_{20}Si_5$ which has HCP. Improvement in mechanical properties was reported when HEAs were fabricated with AM [158,169,177,180,188,193,268]. These improvements are mostly attributed to grain refinement. Grain refinement in HEAs is claimed to be due to the high cooling rates as it happens in various other materials [158,200,230]. Moreover, the wear behavior [189,249], thermo-mechanical analysis [199,246], effect of annealing [98], creep behavior [183], residual stresses [232], corrosion behavior [176,198,226,228,231,241,249], strengthening mechanisms [153] and deformation mechanism [237] of additive manufactured HEAs have also been reported.

Particle reinforcement in a HEA matrix with AM has been an area of interest for many researchers lately who expect microstructure refinement and mechanical properties enhancement [123,177,208,212,220,221,269–280]. Li et al. [177] introduced nano TiN ceramic particles in a CoCrFeMnNi matrix, which led to equiaxed grains of 5 μm. The same group [179] also fabricated the same composition with SLM followed by laser remelting and obtained ultrafine grains (80% grains less than 2 μm and 90% grains less than 3.5 μm). Song et al. [188] showed that the YS and ductility of CoCrFeNi increased by 25% and 34%, respectively, when doped with 1.8 at% nitrogen. Fu et al. [279] noticed that adding Ti-C-O particles into NbTaTiV increased the UTS, YS and fracture strain up to 2270 MPa, 1760 MPa and 11%, respectively. Amar et al. [239] added TiC into CoCrFeNiMn and found the YS and UTS increased from 300 MPa to 385 MPa and from 550 MPa to 723 MPa, respectively. Similarly, Li et al. [238] embedded WC particles into CoCrFeNiMn alloy and observed improvement in YS from 300 to 675 MPa and UTS from 550 to 845 MPa due to the formation of $Cr_{23}C_6$ precipitates. Li et al. [181] noticed that TiC reinforcement CoCrFeNiMn gave the UTS of around 1100 MPa. Rogal et al. [271] increased the UTS of CoCrFeNiMn up to 1600 MPa by introducing nano-Al_2O_3 particles. Carbon doping was attempted [154,155,180,186] to enhance the mechanical properties of HEAs. Peng et al. [208] added diamond particles into CoCrFeNi and found out the bending strength was 925MPa. Park et al. [212] added carbon into CoCrFeNiMn ((CoCrFeNiMn)$_{99}C_1$) and noticed that the YS and UTS were ~741 MPa and ~874 MPa, respectively. Similarly, Kim et al. [221] also added carbon into CoCrFeNiMn in a ratio $(CoCrFeNiMn)_{100-x}C_x$ (x = 0.5–1.5). The YS for x = 0.5, 1, 1.5 was measured to be 653, 752 and 753 MPa respectively. The UTS for x = 0.5, 1, 1.5 was found to be 766 ± 318.5, 895 ± 22.3 and 911 ± 125.1 MPa, respectively. Shen et al. [258] discussed the effect of SiC particles added to CoCrFeNi. They noticed that adding SiC particles changed the microstructure from the FCC phase to the FCC/Cr_2C_7 dual phase. The hardness and YS improved significantly from ~139 HV to ~310 HV and ~142 MPa to ~713 MPa, respectively.

Various HEAs have exhibited significant improvement in their mechanical properties after AM synthesis as compared to the as-cast structures of the same compositions [153,154]. Zhou et al. [155] reported that arc-melted CoCrFeNi had the YS of 225 MPa whereas SLM-manufactured CoCrFeNi had the YS of 656 MPa. Brif et al. [156] observed that SLM-manufactured CoCrFeNi showed noticeable improvement in YS from 188 MPa (as-cast) to 600 MPa and in UTS from 457 MPa (as-cast) to 745 MPa. Peyrouzet et al. [157] showed that the YS of $Al_{0.3}$CoCrFeNi increased from 275 MPa (as-cast) to 730 MPa and the UTS from 502 MPa (as-cast) to 896 MPa when manufactured with SLM. The UTS of as-cast $Al_{0.3}$CoCrFeNi was 522 MPa and it was increased to 878 MPa with SLM processing [158]. Arc-melted $Al_{0.5}$CoCrFeNi had the YS of 334 MPa and the UTS of 709 MPa [159]. SLM increased the YS up to 579 MPa and the UTS up to 721 MPa [160].

Moreover, the CS of AlCrCuFeNi was 2052 MPa when fabricated with SLM and 1750 ± 15 MPa [281] with arc-melting. The hardness of AlCoCrCuFeNi improved from 500 to 710 Hv [194] by using SLM. The YS of AlMgScZrMn manufactured with arc melting, SPS, and SLM is 188 ± 2.3 MPa, 231 ± 3 Mpa and 394 Mpa respectively [195]. Agrawal et al. [197] reported that the YS of as-cast and SLM-printed $Fe_{40}Mn_{20}Co_{20}Cr_{15}Si_5$ was 420 ± 20 Mpa and 530 ± 40 Mpa, respectively. The YS of CoCrFeNiMn was 2.5 times higher (around 518 Mpa) [236] with DED in comparison to that of cast parts (209 Mpa) [282] at room temperature (RT). Furthermore, the as-cast AlCoCrFeNi had the UTS of 956 MPa, and the EBM specimen had the UTS of 1073 MPa [226]. Similarly, Fujieda et al. [228] reported that EBM-synthesized CoCrFeNiTi showed the improved tensile strength of around 1178 MPa, which is much stronger than various commercial high corrosion resistant materials such as duplex stainless steel: 655 MPa, super duplex stainless steel: 750–800 MPa and Ni-based super alloys (i.e., Alloy C276: 690 MPa, Alloy 718: 1275 MPa).

Refractory HEA NbMoTaW has shown a drastic reduction in grain size when made with AM. The average grain size of BCC phase was 200 μm in as-cast sample [283] and

13.4 μm in SLM-processed sample. Additionally, this alloy did not follow the rule of mixtures. Instead, it showed the cocktail effect for the hardness of the final structure. The hardness of Nb, Mo, Ta and W was in the range of 85–410 HV but the final hardness of SLM processed NbMoTaW was measured to be 826 HV [198]. Senkov et al. [284] commented that NbMoTaW did not have any abrupt hardness changes at high temperatures, consistently exhibiting better hardness properties than superalloys. Moreover, SLM-processed $Ni_6Cr_4WFe_9Ti$ (UTS = 972 MPa, YS = 742 MPa, ε = 12.2%) had ~93% increase in YS, ~50% increase in UTS, and ~77% increase in tensile ductility as compared to the vacuum arc melted samples (UTS = 649 MPa, YS = 385 MPa, ε = 6.9%) [200,201].

In summary, various studies have successfully manufactured SLM, EBM and DED techniques. They have also shown that the properties of HEAs could be altered by changing the input parameters for AM process. For example, CoCrFeNiMn was manufactured with SLM by multiple researchers [153,154,169,176–185,188,202–206,209,212,214,215,217,220,221] and many of them acquired different mechanical properties for CoCrFeNiMn by changing input parameters in AM processes (refer Tables 1–3).

3. Applications under Extreme Environments

3.1. Nuclear Applications

Nuclear energy is contributing to around 13% of electricity demand worldwide [285] with negligible carbon emission. The safety, reliability and economy of these nuclear power plants depends heavily on the performances of advanced structural materials under high-energy irradiation and elevated temperatures [286,287]. Radioactive waste handling units also require radiation-tolerant materials. Not to mention nuclear applications, radiation-resistant materials are in great demand in medical and aerospace fields as well.

The typical range of operating temperatures of nuclear reactors spans from 350 to 900 °C as listed in Table 4 [288]. At high temperatures, several effects come into play such as thermal expansion, vacancy concentration, diffusion rate, phase transformation, precipitation, recovery, recrystallization, dislocation climb, creep, grain weakening/migration/growth, oxidation and intergranular oxygen dispersion. With conventional alloys, design strategies for nuclear reactor materials were mostly concerned with tuning the microstructures by various heat treatments, precipitation, cold working and solute atoms to get desired properties. HEAs, though, introduce the concept of modifying compositional complexity of the structural materials to make them suitable for nuclear applications.

Table 4. Core outlet temperature of different gen-IV nuclear reactor coolant [288].

Reactor System	Core outlet Temperature (°C)	Coolant
Super critical water-cooled reactor	350–620	Water
Sodium-cooled fast reactor	~550	Na liquid metal
Lead-cooled reactor	550–800	Pb, Pb-Bi liquid Metals
Molten salt reactor	700–800	Fluoride salts
Gas-cooled fast reactor	~850	Helium gas
Very high temperature reactor	>900	Helium gas

Currently, reduced activation ferritic/martensitic steels (RAFM) (e.g., F82H, EUROFER 97), are the most popular option for irradiation-resistant structural materials. Oxide dispersion strengthened (ODS) RAFM steels (i.e., EUROFER 97 reinforced with 0.3 wt.% Y_2O_3 particles), C/C, SiC/C, SiC/SiC, refractory metals/alloys (W, Cr), V and Ti-based alloys are also being used [289,290]. HEAs are considered to be potential candidates for nuclear applications [2,291–293]. Yeh et al. [294] mentioned that HEAs are potential candidates for structural materials of the 4th generation nuclear reactor. Previously, the irra-

diation responses and defect behaviors [65,66], intrinsic transport properties [66], irradiation induced structural changes [295] of HEAs were reviewed. Building upon these reviews, this section mainly focuses on ion irradiation resistance of HEAs.

The majority of the previous ion irradiation studies on HEAs are listed in Table 5 where phases, irradiation conditions and important findings are summarized. These HEAs were studied under Ni, Au, Ag, Ar, He, Kr, or Xe ions irradiation. The most popular strategy to design single-phase HEAs of high irradiation resistance used elements having low activation or thermal neutron absorption cross section [296–300].

Table 5. Summary of irradiation studies on HEAs.

Source	Material (Fabrication)	Phase	Irradiation conditions (Energy, Ion, Fluence, Temperature)
Jawaharram et al. [301]	CoCrFeNiMn	FCC	2.6 MeV, Ag^{3+}, 1.5×10^{-3} & 1.9×10^{-3} dpa^{-1} s^{-1}, 23–500 °C
Lu et al. [302]	NiCoFeCr, CoCrFeNiMn	FCC	3 MeV, Ni^{2+}, 5×10^{16} ions·cm^{-2}, 500 °C
Barr et al. [303]	CoCrFeNiMn	FCC	3 MeV, Ni^{2+}, 3×10^{15} ions·cm^{-2}, 500 °C
Lu et al. [304]	CoCrFeNi, CoCrFeNiMn	FCC	1.5 MeV, Ni^{+}, 4×10^{14} & 3×10^{15} ions·cm^{-2} (peak dose~4 dpa), 500 °C 3 MeV, Ni^{+}, 5×10^{16} ions·cm^{-2} (peak dose~60 dpa), 500 °C
Tong et al. [305]	CoCrFeNiMn CoCrFeNi CoCrFeNiPd	FCC	16 MeV, Ni^{5+}, 8 MeV Ni^{3+}, 4 MeV Ni^{1+}& 2 MeV Ni^{1+}, 0.1–1 dpa, 420 °C
Jin et al. [306]	CoCrFeNi, CoCrFeNiMn	FCC	3 MeV, Ni^{2+}, 5×10^{16} ions·cm^{-2} (peak dose~53 dpa), 500 °C
Chen et al. [307]	CoCrFeMnNi $Al_{0.3}$CoCrFeNi	FCC FCC	1 MeV, Kr ions, 6.3×10^{15} ions·cm^{-2}, 300 °C
Wang et al. [308]	CoCrFeNiCu	FCC	100 keV, He^{+}, 2.5×10^{17}, 5×10^{17} & 1×10^{18} ions·cm^{-2}, RT
He et al. [309]	CoCrFeNi, CoCrFeNiMn, CoCrFeNiPd	FCC	electrons, 5×10^{18} e·cm^{-2}·s^{-1}, 400 °C
Yang et al. [310]	CoCrFeNiMn, CoCrFeNiPd	FCC	3MeV, Ni^{2+}, 5×10^{16} ions·cm^{-2}, 420, 500 & 580 °C
Yang et al. [311]	CoCrFeNiMn	FCC	-, He ion, -, RT & 450 °C
Hashimoto et al. [312]	CoCrFeNiMn, $CoCrFeNiAl_{0.3}$	FCC	1250 keV, 1.5 dpa, 300–400 °C
Zhang et al. [313]	CoCrFeNiCu	FCC	3 MeV Ni^{2+}, 10^{14} ions·cm^{-2}, RT
Yang et al. [314]	CoNi, FeNi, CoCrFeNi	- FCC	3 MeV, Ni^{2+}, 1.5×10^{16} (peak dose~17 dpa) & 5.0×10^{16} (peak dose~53 dpa) ions·cm^{-2}, 500 °C
Abhaya et al. [315]	CrCoFeNi	FCC	1.5 MeV, Ni^{2+}, 1×10^{15} (peak dose~2 dpa) & 5×10^{16} (peak dose~96 dpa) ions·cm^{-2}, RT
Sellami et al. [316]	CoCrFeNi		1.5 MeV, Ni^{2+}, 1×10^{13}–1×10^{14} ions·cm^{-2} 21 MeV, Ni^{2+}, 2×10^{13} & 1×10^{14} ions·cm^{-2}, RT
Chen et al. [317]	CoCrFeNi	FCC	275 keV, He^{+}, 5.14×10^{20} ions·m^{-2}, 250, 300, 400 °C
Kombaiah et al. [318]	CoCrFeNi, $Al_{0.12}$CoCrFeNi	FCC	3 MeV, Ni^{2+}, 1×10^{17} ions·cm^{-2} (peak dose~100 dpa), 500 °C
Lu et al. [319]	CoCrFeNiPd	FCC	3 MeV, Ni^{2+}, 5×10^{16} ions·cm^{-2}, 580 °C
Tunes et al. [320]	CrFeNiMn	FCC	30 keV, Xe^{+}, 2.6×10^{16} ions·cm^{-2}, 500 °C
Edmondson et al. [321]	CrFeNiMn	BCC	30 keV, Xe^{+}, 9.3×10^{16} ions·cm^{-2} 6 keV He^{+}, 6.4×10^{16} ions·cm^{-2}, RT
Fan et al. [322]	CoCrFeNi	FCC	3 MeV, Ni ions, 5×10^{16}–8×10^{16} ions/cm^{-2}, 580 °C
Chen et al. [81]	$CoCrFeNiTi_{0.2}$	FCC	275 keV, He^{2+}, 5.14×10^{20} ions·m^{-2}, 400 °C
Lyu et al. [323]	$CoCrFeNiMo_{0.2}$	FCC	27 keV, electrons, -, RT
Xu et al. [324]	$(CoCrFeNi)_{95}Ti_1Nb_1Al_3$	FCC	2.5 MeV, Fe ions, 1.5×10^{19} ions·m^{-2}, RT-500 °C
Cao et al. [325]	$(CoCrFeNi)_{94}Ti_2Al_4$	FCC	4 MeV, Au ions, 10–49 dpa, RT
Tolstolutskaya et al. [326]	$Cr_{0.18}Fe_{0.4}Mn_{0.28}Ni_{0.14}$ $Cr_{0.18}Fe_{0.28}Mn_{0.27}Ni_{0.28}$ $Cr_{0.2}Fe_{0.4}Mn_{0.2}Ni_{0.2}$	FCC	1.4 MeV, Ar ions, 0, 0.3, 1 & 5 dpa, RT
Kumar et al. [327]	$Fe_{0.27}Ni_{0.28}Mn_{0.27}Cr_{0.18}$	FCC	3 MeV, Ni^{2+}, 4.2×10^{13}, 4.2×10^{14} & 4.2×10^{15} ions·cm^{-2}, RT & 500 °C 3 MeV, Ni^{2+}, 2.43×10^{15} & 2.43×10^{16} ions·cm^{-2}, 400–700 °C
Li et al. [328]	$Cr_{0.18}Fe_{0.27}Ni_{0.28}Mn_{0.27}$	FCC	Neutron, 8.9×10^{14} n·cm^{-2}.s, 60 °C
Voyevodin et al. [329]	$Cr_{0.2}Fe_{0.4}Mn_{0.2}Ni_{0.2}$+ Y_2O_3 + ZrO_2	FCC	1.4 MeV, Ar ions, 2.2×10^{15} ions·cm^{-2}, RT
Dias et al. [330]	$Cu_xCrFeTiV$ (x = 0.21–1.7)	BCC + FCC	300 keV, Ar^{+}, 3×10^{20} at·m^{-2}, RT

Yang et al. [298]	$Al_{0.3}CoCrFeNi$	FCC	3 MeV, Au ions, 6×10^{15} ion·cm^{-2} (peak dose ~31 dpa), 250–650 °C
Gromov et al. [331]	AlCoCrFeNi	-	18 keV, electrons, -, RT
Zhang et al. [299]	AlCrMoNbZr, (AlCrMoNbZr)N	FCC	400 keV, He^+, 8×10^{15} & 8×10^{16} ion·cm^{-2}, RT
Yang et al. [82]	$Al_{0.1}CoCrFeNi$, $Al_{0.75}CoCrFeNi$, $Al_{1.5}CoCrFeNi$,	FCC FCC + B2 A2 + B2	3 MeV, Au ions, 1×10^{14}–1×10^{16} ions·cm^{-2}, RT
Xia et al. [83]	$Al_{0.1}CoCrFeNi$, $Al_{0.75}CoCrFeNi$, $Al_{1.5}CoCrFeNi$	FCC FCC + B2 B2 + A2	3 MeV, Au ions, 1×10^{14}–1×10^{16} ions·cm^{-2}, RT
Yang et al. [332]	$Al_{0.1}CoCrFeNi$	FCC	3 MeV, Au ions, 6×10^{15} ions·cm^{-2}, 250–650 °C
Zhou et al. [333]	$Al_xCoCrFeNi$ (x = 0–2)	FCC + BCC	1 MeV, Kr^{2+}, -, RT
Zhou et al. [334]	$Al_xCoCrFeNi$, HfNbTaTiZrV	FCC Amorphous	MeV Kr & 200 KeV, electrons, 2 dpa, RT & 150 °C
Zhou et al. [335]	HfNbTaTiZrV	BCC	1 MeV Kr^{2+}, -, RT-150 °C
Moschetti et al. [336]	HfNbTaTiZr	BCC	5 MeV, He^{2+}, 1.6×10^{12}–4.4×10^{17} ions·cm^{-2}s, 50 °C
Sadeghilaridjani et al. [337]	HfTaTiZrV	BCC	4.4 MeV, Ni^{2+}, 1.08×10^{17} ion·cm^{-2}, RT
Li et al. [338]	HfNbTiZr	BCC	1.5 MeV, He ions, 5×10^{15}–$1 \cdot 10^{17}$ ions·m^{-2}, 700 °C
Kareer et al. [339]	TaTiVZr, TaTiVCr, TaTiVNb	BCC BCC BCC	2 MeV, V^+, 2.26×10^{15} ions·cm^{-2}, 500 °C
Wang et al. [340]	ZrTiHfCuBe, ZrTiHfCuBeNi, ZrTiHfCuNi	Amorphous	100 keV, He ions, 5.0×10^{17}, 1.0×10^{18} & 2.0×10^{18} ions·cm^{-2}, RT
Lu et al. [80]	$Ti_2ZrHfV_{0.5}Mo_{0.2}$	BCC	3 MeV, He^+, 5×10^{15}, 1×10^{16} & 3×10^{16} ions·cm^{-2}, 600 °C
Atwani et al. [341]	$W_{0.38}Ta_{0.36}Cr_{0.15}V_{0.11}$	BCC	1 MeV, Kr^{+2}, 0.0006–8 dpa·s^{-1}, 800 °C
Komarov et al. [342]	(TiHfZrVNb)N	-	500 KeV He^{2+}, 5×10^{16}–3×10^{17} ions·cm^{-2}, 500 °C
Gandy et al. [343]	SiFeVCrMo SiFeVCr	sigma BCC+ sigma	5 MeV, Au^{2+}, 5×10^{15} ions·cm^{-2}, RT
Patel et al. [344]	$V_{2.5}Cr_{1.2}WMoCo_{0.04}$	BCC	5 MeV, Au^+, 5×10^{15} ion·cm^{-2} (peak dose~42 dpa), RT
Zhang et al. [345]	$Mo_{0.5}NbTiVCr_{0.25}$, $Mo_{0.5}NbTiV_{0.5}Zr_{0.25}$	BCC	400 He^{2+}, 1×10^{17}–5×10^{17} ions·m^{-2}, 350 °C
Zhang et al. [346]	$Mo_{0.5}NbTiVCr_{0.25}$, $Mo_{0.5}NbTiV_{0.5}Zr_{0.25}$	BCC	400 keV, He^{2+}, peak dose~10.5 dpa, 350 °C
Atwani et al. [347]	WtaCrV	BCC	2 keV, He^+, 1.65×10^{17} ions·cm^{-2}, 950 °C

3.1.1. Dislocation

Neutrons generated from fission/fusion reactors induce atomic displacements in structural materials and may introduce point defects. Development of interstitial and vacancy defects will change local lattice parameters of the original phase. This will lead to deterioration of structural materials, namely, hardening, phase instability, irradiation-induced segregation, irradiation-induced creep, volumetric swelling and H/He embrittlement [290,348,349]. For instance, Yang et al. [332] noticed various defects (i.e., dislocation loops, long dislocations and stacking-fault tetrahedra) were induced by irradiation of 3 MeV Au ion on $Al_{0.1}CoCrFeNi$ but they did not observe void formation. They noticed that defect density decreased and defect size increased with the increasing temperature. Chen et al. [81] investigated the effect of irradiation of He^+ 275 KeV on $FeCoNiCrTi_{0.2}$ at 400 °C. They reported that high pressure He bubbles generated at the peak damage region and faulted dislocation loops (1/3<111>) formed. Perfect loops were rarely noticed and the size of the faulted loops was observed to be abnormally large. They also determined stalking fault energy (SFE) and reported the upper limit for SFE at 400 °C for FeCoNiCr and $FeCoNiCrTi_{0.2}$ was estimated approximately to be ~80 mJ·m^{-2} for the largest radius of a faulted loop of ~15 nm and ~30 mJ·m^{-2} for the largest radius of a faulted loop of ~55 nm, respectively. This showed that adding Ti significantly reduced the SFE.

Yang et al. [314] studied the irradiation behavior of CoCrNiFe with 3 MeV Ni^{2+} ions at 500 °C. They investigated the defects (dislocation loops and void distribution) as a function of depth. The defects were found at the depth of 200–600 nm and 1100–2000 from the

surface. Overall, the average defect diameter was measured to be <10 nm. Lu et al. [302] observed the irradiation behavior of FeNi, CoFeNi, CoCrFeNi and CoCrFeNiMn under 3 MeV Ni^{2+} ions at 500 °C. In SEM images, they noticed faulted (1/3<111>) dislocation loops in all of these alloys as a result of irradiation. These loops increased with the increasing number of principal elements. Yang et al. [298] studied $Al_{0.3}$CoCrFeNi under 3 MeV Au ion irradiation. Average dislocation loop size was found to be ~12 nm at 250 °C and ~32 nm at 500 °C. Dislocation loop density was ~$18 \cdot 10^{21}$ m^{-3} at 250 °C and ~$2 \cdot 10^{21}$ m^{-3} at 500 °C. Hence, the average defect size increased and defect density decreased with irradiation temperature.

3.1.2. Hardness

Various researchers claimed that ion irradiation increased the hardness of the HEAs [306,307,326,327,329,337,343] although there are a few cases that reported some deviant behaviors [80,336,341]. HEAs showed better resistance to hardening by irradiation than stainless steels [326,329]. For instance, Sadeghilaridjani et al. [337] reported that the hardness of HfTaTiVZr increased by 20% under Ni^{2+} ion irradiation, but under the same condition, the hardness of SS304 increased by around 50%. Such superior resistance to irradiation hardening was attributed to the reduced mobility of the point defects due to sluggish diffusion and self-healing ability. Similarly, Tolstolutskayaet et al. [326] irradiated CrFeNiMn, $Cr_{0.18}Fe_{0.4}Ni_{0.28}Mn_{0.14}$ and $Cr_{0.18}Fe_{0.28}Ni_{0.27}Mn_{0.28}$ with 1.4 MeV and found out that the hardness increased by 22–45%. They also reported that the hardness of austenitic steels, such as X18H10T and SS316, almost doubled under similar irradiation conditions.

3.1.3. Phase Stability

The microstructure of a material under irradiation could be affected by formation of defect clusters, dislocation loops, stacking faults, precipitates, voids, or He bubbles. These phenomena may even alter local chemical compositions. Such microstructural changes could lead to deterioration in properties such as conductivity, ductility, fracture toughness or creep strength. Irradiation damage also can cause material swelling, irradiation-induced creep (IIC), irradiation-assisted stress corrosion cracking or irradiation growth. The attractive properties of the HEAs typically come from specific phases acquired with suitable compositions. Moreover, there are various potential intermetallics compositions present in HEAs. Therefore, the phase stability analysis becomes of utmost importance. Taking advantage of recent advancement in microstructure characterization technologies, most of the studies mentioned in Table 5 focused on the phase stability and microstructural changes after ion irradiation. Phase stability after irradiation was observed for several HEAs such as CoCrFeNiMn, CoCrFeNiPd and high entropy metallic glasses such as ZrTiHfCuBe and ZrTiHfCuBeNi [340] and Al_xCoCrFeNi (x = 0.1–1.5) [82,83]. Such high phase stability was mainly attributed to sluggish diffusion and high configurational entropy that kinetically restrains precipitation by reducing thermodynamic driving force. Moreover, Kumar et al. [327] reported that $Fe_{0.27}Ni_{0.28}Mn_{0.27}Cr_{0.18}$ alloy exhibited higher phase stability and higher resistance to radiation swelling and void formation in comparison to austenitic stainless steels. No micro-void formed in CoCrFeNi irradiated by 1.5 MeV Ni^{2+} ion. Thanks to its superior interface stability during irradiation, AlCrMoNbZr/(AlCrMoNbZr)N was considered a promising candidate for an accident-tolerant fuel cladding material [299].

On the other hand, Wang et al. [308] noticed a reduction in crystallinity resulted from He ion irradiation on CoCrFeCuNi alloy. Yang et al. [298] observed that precipitation of the L12 phase was suppressed due to irradiation-induced ballistic mixing at temperatures less than or equal to 500 °C. Additionally, precipitation of the B2 phase was favored at 650 °C due to improved diffusion by irradiation. They found that the swelling resistance of CoCrFeNiMn was less than 0.5% for temperatures up to 680 °C. They attributed the improved resistance to the void-induced swelling of these alloys to the complex arrangements of different atoms in the lattice structure. Gandy et al. [343] reported irradiation-

induced phase transformation in SiFeVCrMo from the tetragonal sigma phase to BCC. This BCC phase formed at high temperatures as well as after ion irradiation. Under irradiation of 3 MeV Ni^{2+} ion, NiCoFeCr maintained its phase stability; however, $Al_{0.12}$NiCoFeCr showed phase change. $Al_{0.12}$NiCoFeCr microstructure changed from single FCC to FCC matrix, nanoprecipitates (i.e., Ni_3Al) and ordered structure (i.e., L12) [318]. Irradiation of 3 MeV Ni^{2+} ion on the CoCrFeNiMn alloy induced Mn depletion and Co/Ni enrichment at grain boundaries [303]. He et al. [309] studied the phase stability of CoCrFeNi, CoCrFeNiMn and CoCrFeNiPd under electron radiation. They concluded that Cr, Fe, Mn and Pd elements were most likely to deplete and Co/Ni preferred to accumulate at defect clusters (i.e., dislocation loops). Atwani et al. [341] irradiated CrTaVW HEA with 1 MeV Kr^{+2} ions at 800 °C. This HEA showed the segregation of Cr and V at the triple junction and grain boundaries after irradiation. Yang et al. [332] and Lu et al. [302] also noticed that Ni and Co tended to enrich, but Cr, Fe and Mn preferred to deplete at defect clusters in $Al_{0.1}$CoCrFeNi under 3 MeV Au ion irradiation.

3.1.4. Irradiation-Induced Creep (IIC)

Irradiation-induced creep is another important aspect since nuclear reactors operate at high temperatures as shown in Table 5. Jawaharram et al. [301] studied both thermal creep and irradiation-induced creep (IIC) of Cantor alloy (CoCrFeMnNi). For IIC measurement, CoCrFeNiMn was irradiated with 2.6 Mev Ag^{3+} ion in the temperature range of 23–650 °C. They reported that over the temperature range investigated, ICC was more dominant that thermal creep.

3.1.5. Swelling Resistance

Density reduction by volume increase due to formation of voids and defects is the mechanism behind material swelling. In order to maintain the structural integrity and mechanical strength, reasonably high swelling resistance is required for structural materials for nuclear applications. Several HEAs showed adequate swelling resistance under irradiation. Yang et al. [332] reported negligible void formation in $Al_{0.1}$CoCrFeNi under 3 MeV Au ion irradiation. Moreover, Yang et al. [314] noticed that dislocation loops and void distribution varied as a function of depth in CoCrFeNi under 3 MeV Ni^{2+} ion irradiation. Jin et al. [306] suggested that compositional complexity, including the number and type of components, be taken into consideration to improve swelling resistance. They concluded that adding Fe and Mn would be more effective to reduce swelling than adding Co and Cr. Their results showed that NiCoFeCrMn exhibited 40 times higher swelling resistance than Ni.

3.1.6. Self-Healing

HEAs showed the ability to absorb and heal radiation-induced damages. Self-healing of HEAs was explained by Egami et al. [350] in detail. Xia et al. [83] reported that defect clustering in disordered FCC or BCC happened in smaller size than in the ordered B2 phase. They attributed this effect to the reduced defect mobility and large atomic stress in the disordered phases which might have led to self-healing. Patel et al. [344] investigated the phase stability of $V_{2.5}Cr_{1.2}WMoCo_{0.04}$ under 5 MeV Au^{+} ion irradiation. They noticed that 96% of the BCC phase of the as-cast alloy remained intact up to the irradiation dose of 42 displacement per atom (dpa). The remaining 4% converted to another BCC phase with a little larger lattice parameter. Their energy dispersive X-ray (EDX) analysis detected no element segregation. Such phase stability was attributed to the self-healing capability [350]. Tong et al. [305] concluded that the local lattice distortion could be relaxed by lattice expansion with low dose of irradiation. Sellami et al. [316] irradiated CoCrFeNi with 1.5 MeV and 21 MeV Ni Ions. They reported elastic strain values of ~0.035% and 0% for 1.5 MeV Ni ion and 21 MeV Ni ion irradiations, respectively. They suggested that the

complex composition of HEAs induced higher chemical disorder that reduced the mobility of defects generated by low energy (i.e., 1.5 MeV Ni) ion irradiation; therefore, a small elastic strain of ~0.035% was obtained. Furthermore, when low energy irradiation CoCrFeNi alloy was further subjected to high-energy (i.e., 21 MeV Ni) irradiation, elastic strain relaxation (resulted into ~0% elastic strain) was observed which could be attributed to the mechanisms such as defect annealing, recombination and rearrangement.

3.1.7. Miscellaneous

Lu et al. [80] reported an unexpected decrease in lattice parameter by 0.676% after He ion irradiation on $Ti_2ZrHfV_{0.5}Mo_{0.2}$. Similarly, TiZrNbHfTa showed insignificant changes in hardness but a considerable increase in UTS and YS without loss of ductility [336]. Li et al. [328] noticed an increase in electrical resistivity of $Fe_{0.27}Mn_{0.27}Ni_{0.28}Cr_{0.18}$ after neutron irradiation.

3.2. Wear Behavior

The wear properties of HEAs were studied mostly with pin/ball on a disc set up with antagonist materials such as Al_2O_3, steels (i.e., SKH51, GCr15, 100Cr6), Si_3N_4, SiC, ZrO_2, 1Cr18Ni9Ti, BN, inconel-718 and WC. For lubrication, mostly dry conditions were used but some studies also used H_2O_2, deionized water and acid rain (pH = 2). Previously, Tsai and Yeh et al. [351], Kasar et al. [352], Senkov et al. [67], Sharma et al. [16], Zhang et al. [37], Li et al. [42], Menghani et al. [353] and Ayyagari et al. [354] discussed the wear behaviors of HEAs. In this review, we will analyze the tribological studies of HEAs in terms of HEAs content variation, particle reinforcement, media and nitriding/carburizing/sulfurizing, temperature effects and oxide formation. Table 6 provides the details of the compositions, microstructures, methods and results (i.e., wear rate or wear resistance, hardness, friction coefficient) of the wear studies performed so far on HEAs.

Table 6. Wear studies of HEAs.

Source	Composition	Microstructure	Method, Medium, Antagonist Material, Temperature, Wear Rate
Joseph et al. [355]	CoCrFeNiMn	FCC	Pin-on-disc, dry, Al_2O_3, 600–800 °C, RT, 0.5×10^{-4}–3.8×10^{-4} $mm^3 \cdot N^{-1} \cdot m^{-1}$
Wang et al. [356]	CoCrFeNiMn	FCC	Ball-on-disc, MoS_2-oil lubrication, GCr15, RT-140 °C
Xiao et al. [357]	CoCrFeNiMn	FCC	Ball-on-flat, dry, WC-Co, RT, 0.5×10^{-4}–5.4×10^{-4} $mm^3 \cdot N^{-1} \cdot m^{-1}$
Jones et al. [358]	CoCrFeNiMn	FCC	Rotary tribometer, -, -, ~0.5×10^{-6} $mm^3 \cdot N^{-1} \cdot m^{-1}$
Zhu et al. [359]	CoCrFeNiMn CoCrFeNiMnV CoCrFeNiMnNb CoCrFeNiMnNbV	FCC + HCP (Laves) + σ	Ball-on-disc, dry, Si_3N_4, RT, 1.85×10^{-5}–6.39×10^{-5} $mm^3 \cdot N^{-1} \cdot m^{-1}$
Deng et al. [360]	$CoCrFeNiMo_x$ (x = 0–0.3)	FCC	Ball-on-disc, dry, GCr15, RT, 0.33×10^{-3}–0.53×10^{-3} $mm^3 \cdot N^{-1} \cdot m^{-1}$
Lindner et al. [361]	CoCrFeNiMn CoCrFeNi	FCC FCC	Ball-on-disc, dry, Al_2O_3, RT
Sha et al. [362]	(CoCrFeNiMn)N	FCC + BCC	Ball-on-disc, dry, ruby, RT, 1×10^{-7}–1.4×10^{-6} $mm^3 \cdot N^{-1} \cdot m^{-1}$
Xiao et al. [363]	$CoCrFeNiMnC_x$ (x = 0–1.2)	FCC	Ball-on-disk, dry, Si_3N_4, RT, 0.47×10^{-5}–6.5×10^{-5} $mm^3 \cdot N^{-1} \cdot m^{-1}$
Zhu et al. [277]	CoCrFeNiMn + TiN-Al_2O_3	FCC + TiN	Ball-on-disc, dry, 440C steel, RT
Cheng et al. [364]	CoCrFeNiMn $Al_{0.5}$CoCrFeNiMn AlCoCrFeNiMn	FCC FCC + BCC FCC + BCC	Ball-on-disc, dry, Si_3N_4, RT-800 °C, 0.5×10^{-4}–3.8×10^{-4} $mm^3 \cdot N^{-1} \cdot m^{-1}$
Joseph et al. [365]	CoCrFeNiMn $Al_{0.3}$CoCrFeNi $Al_{0.6}$CoCrFeNi AlCoCrFeNi	FCC FCC FCC + BCC BCC	Pin-on-disc, dry, Al_2O_3, 25 & 900 °C
Liu et al. [366]	CoCrFeNiMn + Y_2O_3	FCC + Y_2O_3 (particles)	Ball-on-disc, dry, GCr15, RT

Wang et al. [367]	$(CoCrFeMnNi)_{85}Ti_{15}$	FCC + BCC	Ball-on-disc, dry, Si_3N_4, RT-800 °C, 4×10^{-6}–2.23×10^{-5} $mm^3 \cdot N^{-1} \cdot m^{-1}$
Zhang et al. [368]	CoCrFeNi + (Ag or BaF_2/CaF_2)	FCC	Ball-on-disk, dry, Inconel-718, RT, ~4×10^{-5}–40×10^{-5} $mm^3 \cdot N^{-1} \cdot m^{-1}$
Geng et al. [369]	CoCrFeNi	FCC	Pin-on-disc, vacuum (4 Pa) & air, Inconel 718, RT, 0.6×10^{-4}–8×10^{-4} $mm^3 \cdot N^{-1} \cdot m^{-1}$
Zhang et al. [370]	CoCrFeNi + (graphite or MoS_2)	FCC	Ball-on-disk, dry, Si_3N_4, RT-800 °C, ~1×10^{-5}–23×10^{-5} $mm^3 \cdot N^{-1} \cdot m^{-1}$
Zhou et al. [371]	$CoCrFeNiMo_{0.85}$ $Al_{0.5}CoCrFeNi$	FCC FCC	Slurry jet test-rig, HCl+NaCl, -, 40 °C, -
Zhang et al. [372]	CoCrFeNiMo	FCC	Ball-on-disc, dry, -, RT
Huang et al. [373]	$FeCoCrNiSi_x$	FCC + BCC	Ball-on-disk, dry, GCr15, RT
Cui et al. [374]	CoCrFeNiMo Sulfurized at 260 °C for 2 h	FCC + FeS/MoS_2 film	Pin-on-disk, dry, GCr15, RT
Li et al. [375]	$CoCrFeNiMo_{0.2}$	FCC	Ball on disc, dry, GCr15, RT, 3.9×10^{-4}–5.4×10^{-4} $mm^3 \cdot N^{-1} \cdot m^{-1}$
Ji et al. [376]	CoCrFeNiCu + 2%MoS_2 CoCrFeNiCu + 5%MoS_2 CoCrFeNiCu + 20%WC CoCrFeNiCu + 50%WC CoCrFeNiCu + 80%WC	FCC + MoS_2 (particles) FCC + MoS_2 (particles) FCC + WC (particles) FCC + WC (particles) FCC + WC (particles)	Ball-on-disk, dry, Si_3N_4, RT
Verma et al. [377]	$CoCrFeNiCu_x$ (x = 0–1)	FCC	Pin-on-disk, dry, -, RT & 600 °C, ~1.3×10^{-5}–2.5×10^{-5} $mm^3 \cdot N^{-1} \cdot m^{-1}$
Liu et al. [378]	$CoCrFeNiB_x$ (x = 0.5–1.5)	FCC + Borides	Roller friction wear tester, dry, $W_{18}Cr_5V$, RT
Jiang et al. [379]	$CoCrFeNiNb_x$ (x = 0–1.2)	FCC + HCP (Laves) HCP (Co_2Nb)	Ball-on-disc, dry, BN, RT
Yu et al. [380]	$CoCrFeNiNb_x$ (x = 0.5–0.8)	FCC + HCP (Laves)	Pin-on-disk, dry, Si_3N_4, RT-800 °C, ~1.8×10^{-4}–9×10^{-4} $mm^3 \cdot N^{-1} \cdot m^{-1}$
Liu et al. [381]	$Co_{10}Cr_{10}Fe_{50}Mn_{30}$ + graphene nanoplatelets (0.2–0.8 wt%)	FCC	Ball-on-plate, dry, GCr15, RT
Wang et al. [382]	$Co_{10}Cr_{10}Fe_{40}Mn_{40}$ + WC (10 wt%)	FCC+ WC + $M_{23}C_6$	Ball-on-disc, dry, Si_3N_4, RT
Derimow et al. [383]	$(CoCrCuTi)_{100-x}Mn_x$ (x = 5–10) $(CoCrCuTi)_{100-x}Mn_x$ (x = 10–20)	FCC + BCC FCC + HCP (Laves)	Ball-on-disc, dry, GCr15, RT
Guo et al. [384]	$CoCrFeNiCuSi_{0.2}$ (Ti or C)$_x$ (x = 0-.5)	FCC + TiC	Brooks sliding friction & wear tester, dry, RT
Zhang et al. [385]	$(CoCrFeNiTi_{0.5})C_x$ (x = 3–12 wt%)	BCC + $Cr_{23}C_6$ + TiC	ML-100 friction and wear tester, -, -, RT
Erdoğan et al. [386]	$CoCrFeNiTi_{0.5}$ $CoCrFeNiTi_{0.5}Al_{0.5}$ $CoCrFeNiTi_{0.5}Al$	FCC BCC BCC	Ball-on-disc, dry, WC, RT
Liu et al. [387]	CoCrFeNiMo $CoCrFeNiMo_x$ (x ≥ 0.3) $CoCrFeNiMo_x$ (x ≥ 1)	FCC FCC + σ FCC + σ + μ	Pin-on-disk, dry, YG6, RT, 1×10^{-5}–8.5×10^{-5} $mm^3 \cdot N^{-1} \cdot m^{-1}$
Moazzen et al. [388]	$CoCrFe_xNi$ (x = 1–1.6)	FCC + BCC	Pin-on-disk, dry, AISI52100 steel, 20–30 °C, -
Yang et al. [389]	$CoCrFeNiMoSi_x$ (x = 0.5–1.5)	FCC	Pin-on-disk, dry, Si_3N_4, RT, 0.292×10^{-4}–0.892×10^{-4} $mm^3 \cdot N^{-1} \cdot m^{-1}$
Li et al. [390]	$CoCrFeNi_2V_{0.5}Ti_x$ (x = 0.5–1.25)	BCC + $(Co,Ni)Ti_2$	Ball-on-disc, dry, Si_3N_4, RT, 4.4×10^{-5}- 37.5×10^{-5} $mm^3 \cdot N^{-1} \cdot m^{-1}$
Islak et al. [391]	CrFeNiMoTi	FCC	Ball-on-flat, dry, 100Cr6, RT, 2.7×10^{-3}–9.4×10^{-3} $mm^3 \cdot N^{-1} \cdot m^{-1}$
Wen et al. [392]	CrCoNiTiV	FCC + BCC + TiO	HT-1000 tribometer, -, WC, RT & 600 °C
Wang et al. [393]	CuNiSiTiZr	BCC	CJS111A wear tester, dry, -, RT
Cheng et al. [394]	$(Fe_{25}Co_{25}Ni_{25}(B_{0.7}Si_{0.3})_{25})_{100-x}Nb_x$ (x = 0–4 wt%)	BCC + HCP (Laves) + FCC	Ball-on-disc, dry, GCr15, RT, ~1.5×10^{-6}–3.6×10^{-6} $mm^3 \cdot N^{-1} \cdot m^{-1}$
Yadav et al. [395]	$(CuCrFeTiZn)_{1-x}Pb_x$ (x = 0.05–0.2)	FCC + BCC + Pb (particles)	Ball-on-disk, dry, -, SAE 52100, RT, 1.17×10^{-5}–50×10^{-5} $mm^3 \cdot N^{-1} \cdot m^{-1}$
Gou et al. [396]	CoCrFeNi + WC + Mo_2C + NbC	FCC	Ball-on-disc, dry, GCr15, 700 °C
Yadav et al. [397]	$(CuCrFeTiZn)_{100-x}Pb_x$ (x = 0–10) $(CuCrFeTiZn)_{100-x}Bi_x$ (x = 0–10)	FCC + BCC BCC	Ball-on-disk, dry, steel, RT
Cui et al. [398]	$Al_xCoCrFeNiMn$ (x = 0–0.75)	FCC + BCC	MDW- 02 abrasive wear tester, RT
Gwalani et al. [399]	$Al_{0.5}CoCrFeNi$	FCC + B2	Pin-on-disc, dry, Si_3N_4, RT, 1.8×10^{-5}–11×10^{-5} $mm^3 \cdot N^{-1} \cdot m^{-1}$
Chen et al. [400]	$Al_{0.6}CoCrFeNi$	FCC + BCC	Ball-on-plate, dry, Si_3N_4, RT-600 °C, ~0.5×10^{-4}–5×10^{-4} $mm^3 \cdot N^{-1} \cdot m^{-1}$

Du et al. [401]	$Al_{0.25}CoCrFeNi$	FCC	Universal wear testing machine, dry, Si_3N_4 20–600 °C, ~1.5×10^{-4}–3.5×10^{-4} $mm^3 \cdot N^{-1} \cdot m^{-1}$
Chen et al. [402]	$Al_{0.6}CoCrFeNi$	FCC + BCC	Ball-on-block, deionized water & acid rain (pH = 2), seawater, GCr_{15}, RT, 1.58×10^{-4}–6.52×10^{-4} $mm^3 \cdot N^{-1} \cdot m^{-1}$
Ji et al. [403]	$Al_3CoCrFeNi$		Jet erosion testing machine, water and 15 wt% SiO_2 particles (350–600 mm), RT
Haghdadi et al. [404]	$Al_{0.3}CoCrFeNi$ $AlCoCrFeNi$	FCC BCC	Scratch testing, dry, -, RT
Fang et al. [405]	$Al_{0.3}CoCrFeNi$	FCC	Pin-on-disc, dry, -, 900 °C
Wu et al. [406]	$Al_{0.1}CoCrFeNi$	FCC	Ball-on-block, dry and deionized water, Si_3N_4, RT, ~0.2×10^{-4}–1.86×10^{-4} $mm^3 \cdot N^{-1} \cdot m^{-1}$
Nair et al. [407]	$Al_{0.1}CoCrFeNi$ $AlCoCrFeNi$ $Al_3CoCrFeNi$	FCC FCC + BCC (B2) BCC (B2) + A2 + σ	Ball-on-disc, dry, WC, RT
Kumar et al. [408]	$Al_{0.4}Co_xCrFeNi$ (x = 0–1)	-	Pin-on-disc, demineralized water & (demineralized water + 3.5 wt% NaCl), EN-31, RT, 0.81×10^{-4}–1.86×10^{-4} $mm^3 \cdot N^{-1} \cdot m^{-1}$
Mu et al. [409]	$AlCoCrFeNi$	BCC + FCC	Ball-on disc, dry, Si_3N_4, RT
Wu et al. [410]	$AlCoCrFeNi$ $AlCoCrFeNiTi_{0.5}$	BCC	Pin-on-disc, dry, Si_3N_4, RT
Zhao et al. [411]	$Al_{0.8}CoCrFeNi$	FCC + BCC	Ball-on-disk, dry, deionized water + 0.5 wt% NaCl, RT, ~2×10^{-5}–7.5×10^{-5} $mm^3 \cdot N^{-1} \cdot m^{-1}$
Kumar et al. [412]	$Al_{0.4}Co_xCrFeNi$ (x = 0–0.5) $Al_{0.4}Co_xCrFeNi$ (x = 1)	FCC + BCC FCC	Pin-on-disk, engine oil (SAE Grade:20W-40), EN-31 steel, RT, 2.1×10^{-5}–11×10^{-5} $mm^3 \cdot N^{-1} \cdot m^{-1}$
Li et al. [413]	$Al_{0.8}CoCrFeNiCu_{0.5}Si_x$ (x = 0–0.5)	FCC + BCC1 + BCC2	-, -, CGr_{15}, RT, 0.9×10^{-6}–1.19×10^{-6} $mm^3 \cdot N^{-1} \cdot m^{-1}$
Li et al. [272]	$(AlCoCrFeNi)_{100-x}$ $(NbC)_x$ (x = 0–30 wt%)	FCC + BCC	Reciprocating tester, dry, N_4Si_3, RT
Kafexhiu et al. [414]	$AlCoCrFeNi_{2.1}$	BCC + FCC	Ball-on-plate, dry, 100Cr6 steel, RT, 7×10^{-5}–11×10^{-5} $mm^3 \cdot N^{-1} \cdot m^{-1}$
Miao et al. [415]	$AlCoCrFeNi_{2.1}$	FCC (L12) + BCC (B2)	Ball-on-disk, dry, Al_2O_3/Si_3N_4/SiC/GCr15, RT-900 °C, ~1×10^{-4}–4.2×10^{-4} $mm^3 \cdot N^{-1} \cdot m^{-1}$
Ye et al. [416]	$AlCoCrFeNi_{2.1}$ + TiC (0–15 wt%)	FCC + B2 + TiC	MM-200 wear testing machine, dry, -, RT
Wang et al. [417]	(AlCoCrFeNi)N	BCC + nitrides (AlN,CrN,Fe_4N)	Ball-on block, dry, deionized water & acid rain (pH = 2), Si_3N_4, RT, 2.8×10^{-5}–7×10^{-5} $mm^3 \cdot N^{-1} \cdot m^{-1}$
Liu et al. [418]	$AlCrCuFeNi_2$		Ball-on-block, dry, simulated rainwater & deionized water, Si_3N_4, RT, 2.163×10^{-3}–0.23×10^{-3} $mm^3 \cdot N^{-1} \cdot m^{-1}$
Kong et al. [419]	$Al_{1.8}CrCuFeNi_2$	BCC	MMS-2A roller friction wear tester, dry, -, RT
Malatji et al. [263]	$AlCrCuFeNi$	FCC + BCC	Ball-on-disk, dry, SiC, RT
Wang et al. [420]	$Al_{1.3}CoCuFeNi_2$	FCC + BCC	Ball-on block, dry, deionized water & acid rain (pH = 2), Si_3N_4, RT, 1×10^{-4}–12×10^{-4} $mm^3 \cdot N^{-1} \cdot m^{-1}$
Xiao et al. [421]	$Al_xCoCrFeNiSi$ (x = 0.5–1.5)	FCC + BCC	Ball-on-flat, distilled water, WC-12Co, RT, 6.7×10^{-6}–5.5×10^{-5} $mm^3 \cdot N^{-1} \cdot m^{-1}$
Liu et al. [422]	$AlCoCrFeNiSi_x$ (0–0.5)	BCC	Pin-on-disk, dry, ZrO_2, RT, 1.3×10^{-4}–5.1×10^{-4} $mm^3 \cdot N^{-1} \cdot m^{-1}$
Hsu et al. [423]	$Al_{0.5}CoCrFeNiCuBx$ (x = 0–1)	FCC + boride precipitates	Pin-on-disk, dry, Al_2O_3, RT
Chen et al. [424]	$Al_{0.5}CoCrFeNiCuTi_x$ (x = 0–0.2) $Al_{0.5}CoCrFeNiCuTi_x$ (x = 0.4–1) $Al_{0.5}CoCrFeNiCuTi_x$ (x = 1.2–2)	FCC FCC + BCC FCC + BCC + Ti_2N	Pin-on-disk, dry, Al_2O_3, RT
Lobel et al. [425]	$AlCoCrFeNiTi$	BCC	Ball-on-disc, dry, Al_2O_3, RT
Lobel et al. [426]	$AlCoCrFeNiTi$	BCC	Ball-on-plate, dry, 100Cr6 Steel, RT
Wu et al. [427]	$AlCoCrFeNiTi_x$ (x = 0.5–1) $AlCoCrFeNiTi_x$ (x = 1.5) $AlCoCrFeNiTi_x$ (x = 2)	FCC + BCC FCC + BCC + Ti_2Ni FCC + BCC + Ti_2Ni + ordered BCC	Cavitation erosion tests, Distilled water+ 3.5 wt% NaCl, RT
Erdogan et al. [428]	$Al_xCoCrFeNiTi_y$ (x = 0–0.5, y = 0–0.5)	FCC + BCC	Ball-on-disc, dry, WC, RT, 0.25×10^{-4}–1.78×10^{-4} $mm^3 \cdot N^{-1} \cdot m^{-1}$, 0.25×10^{-4}–1.78×10^{-4} $mm^3 \cdot N^{-1} \cdot m^{-1}$
Xin et al. [429]	$Al_{0.2}Co_{1.5}CrFeNi_{1.5}Ti_{0.5}$ + TiC	FCC	Ball-on-disc, dry, Si_3N_4, RT, 0.3×10^{-5}–12.6×10^{-5} $mm^3 \cdot N^{-1} \cdot m^{-1}$
Gouvea et al. [430]	$Al_{0.2}Co_{1.5}CrFeNi_{1.5}Ti$	FCC	Ball-on-plate, dry, AISI 52,100 steel, RT, 1.6×10^{-8}–7.5×10^{-5} $mm^2 \cdot N^{-1}$

Chuang et al. [431]	$Al_xCo_{1.5}CrFeNi_{1.5}Ti_y$ (x = 0–0.2, y = 0.5–1)	FCC	Pin-on-disk, dry, SKH51 steel, RT, ~4 × 10^{-4}–1.8 × 10^{-4} $mm^3 \cdot N^{-1} \cdot m^{-1}$
Liu et al. [432]	$AlCoCrFeNiTi_{0.8}$	BCC + B2	Ball-on-disc, dry, Si_3N_4, RT, 1.36 × 10^{-6}–6.96 × 10^{-6} $mm^3 \cdot N^{-1} \cdot m^{-1}$, 0.7 × 10^{-4}–6 × 10^{-4} $mm^3 \cdot N^{-1} \cdot m^{-1}$
Yu et al. [433]	$AlCoCrFeNiTi_{0.5}$	BCC1 + BCC2	Pin-on-disk, H_2O_2, SiC & ZrO_2, RT
Lobel et al. [434]	$AlCoCrFeNiTi_{0.5}$	BCC (A2 + B2)	SRV-Tribometer, dry, Al_2O_3, 22–900 °C
Chen et al. [435]	$Al_{0.6}CoCrFeNiTi$	BCC	Pin-on-disc, Dry, Al_2O_3 RT-500 °C
Yu et al. [436]	$AlCoCrFeNiTi_{0.5}$ AlCoCrFeNiCu		Pin-on-disc, dry, Si_3N_4
Yu et al. [437]	AlCoCrFeNiCu $AlCoCrFeNiTi_{0.5}$	FCC + BCC1 BCC1 + BCC2	Pin-on-disk, H_2O_2, 1Cr18Ni9Ti steel & ZrO_2/SiC ceramic, RT
Jin et al. [438]	AlCoFeNiCu	FCC + BCC	Ball-on-disk, dry, WC, 200–800 °C
Zhu et al. [439]	AlCoFeNiCu + TiC (10–30 wt%)	FCC + BCC	Ball-on-disk, dry, $Si_3N_4$20–600 °C, ~0.1 × 10^{-5}–6.5 × 10^{-5} $mm^3 \cdot N^{-1} \cdot m^{-1}$
Wu et al. [440]	$Al_{0.5}CoCrFeNiCu$ $Al_{1.0}CoCrFeNiCu$ $Al_{2.0}CoCrFeNiCu$	FCC FCC + BCC BCC	Pin-on-disk, dry, SKH-51 steel, RT
Yan et al. [441]	AlCoCrFeNiSi + Ti (C, N)	BCC + FCC	Ball-on-disc, dry, GCr15, RT, -
Li et al. [442]	AlCoCrFeNi + Ti (C,N) + TiB_2	FCC	Ball-on-disc, dry, WC-6Co, 200–800 °C, 2.69 × 10^{-5}–8.66 × 0^{-5} $mm^3 \cdot N^{-1} \cdot m^{-1}$
Kumar et al. [443]	$AlCoCrCuFeNiSi_{0.3}$ $AlCoCrCuFeNiSi_{0.6}$	FCC + BCC FCC + BCC + σ	Pin-on-disk, dry, -, RT, -
Xin et al. [444]	$Al_{0.2}Co_{1.5}CrFeNi_{1.5}Ti_{0.5}$	FCC	Pin-on-disk, dry, Si_3N_4, 25–800 °C, 1.21 × 10^{-5}–6.7 × 10^{-5} $mm^3 \cdot N^{-1} \cdot m^{-1}$
Karakaş et al. [445]	$Al_{0.07}Co_{1.26}Cr_{1.80}Fe_{1.42}Mn_{1.35}Ni_{1.1}$	FCC	Ball-on-disc, 3.5%NaCl & 5%H_2SO_4, -, RT, 16.26 × 10^{-9}–77.84 × 10^{-8} $mm^3 \cdot N^{-1} \cdot m^{-1}$
Xin et al. [446]	$Al_{0.2}Co_{1.5}CrFeNi_{1.5}Ti_{(0.5+x)} + C_x$ (x = 0)	FCC	Pin-on-disk, dry, Si_3N_4, 25–800 °C, 3.12 × 10^{-6}–12.59 × 10^{-5} $mm^3 \cdot N^{-1} \cdot m^{-1}$
Zhao et al. [447]	$AlCrCoFeNiCTa_x$ (x = 0–1)	BCC	Pin-on-disk, 3.5%NaCl & air, Si_3N_4, RT, 1.67 × 10^{-6}–2.22 × 10^{-5} $mm^3 \cdot N^{-1} \cdot m^{-1}$
Ghanbariha et al. [448]	AlCoCrFeNi + ZrO_2	FCC + BCC	Pin-on-disk, dry, WC, RT, 1.11 × 10^{-3}–2.52 × 10^{-3} $mm^3 \cdot N^{-1} \cdot m^{-1}$
Li et al. [449]	$Al_xCrFeCoNiCu$ (x = 0–0.5) $Al_xCrFeCoNiCu$ (x = 0.5–2)	FCC FCC + BCC	-, dry, GCr15, RT, 6.64 × 10^{-7}–2.26 × 10^{-4} $mm^3 \cdot N^{-1} \cdot m^{-1}$
Cai et al. [450]	AlCrTiV, AlCrTiVSi	BCC	Nanoindenter G200, dry, CGr15 &Al_2O_3, RT, -
Chandrakar et al. [451]	$AlCoCrCuFeNiSi_x$ (x = 0–0.9)	BCC	Pin-on-disk, dry, -, RT, -
Erdogan et al. [452]	AlCrFeNiSi $AlCrFeNi_x$ (x = Cu,Co)	BCC BCC + FCC	Ball-on-disc, dry, WC, RT, -
Duan et al. [453]	AlCoCrFeNiCu	-	Pin-on-disc, H_2O_2, Si_3N_4, RT
Chen et al. [454]	$Al_{0.5}CoCrFeNiCuV_x$ (x = 0–0.2) $Al_{0.5}CoCrFeNiCuV_x$ (x = 0.4–0.8) $Al_{0.5}CoCrFeNiCuV_x$ (x = 1–2)	FCC FCC + BCC BCC	Pin-on-disk, dry, Al_2O_3, RT, 1 × 10^{-4}–2.7 × 10^{-4} $mm^3 \cdot N^{-1} \cdot m^{-1}$
Gu et al. [455]	$Al_xMo_{0.5}NbFeTiMn_2$ (x = 1–2)	BCC	Pin-on-disk, dry, Al_2O_3, RT
Hsu et al. [456]	$AlCoCrFe_xNiMo_{0.5}$ (x = 0.6–2)	BCC + σ	Pin-on-disk, dry, SKH51 steel, RT
Liang et al. [457]	$AlCrFe_2Ni_2W_{0.2}Mo_{0.75}$	BCC	Ball-on-disc, deionized water, Al_2O_3, RT, ~5 × 10^{-6}–22 × 10^{-6} $mm^3 \cdot N^{-1} \cdot m^{-1}$
Qui et al. [458]	$Al_2CoCrFeCuTiNi_x$ (x = 0–2)	FCC + BCC	Tribometer, -, -, RT
Kanyane et al. [459]	AlTiSiMoW	BCC + $TiSi_2$ (ordered FCC)	Ball-on-disc, dry, stainless steel, RT
Huang et al. [460]	AlTiSiVCr	BCC+ $(Ti,V)_5Si_3$ precipitates	Ball-on-disc, dry, GCr15 steel, RT, 2 × 10^{-5}–2.5 × 10^{-5} $mm^3 \cdot N^{-1} \cdot m^{-1}$
Zhang et al. [461]	AlTiSiVNi	B2 (NiAl) + (Ti,V)5Si_3 + TiN	Ball-on-disc, dry, Si_3N_4, RT & 800 °C
Lin et al. [462]	AlCoCrNiW AlCoCrNiSi	W + AlNi + $Cr_{15.58}Fe_{7.42}C_6$ BCC	Pin-on-disc, dry, AISI 52100, RT
Yadav et al. [463]	AlCrFeMnV $(AlCrFeMnV)_{90}Bi_{10}$ $(AlCrFeMnV)_{90}Bi10$ + 10 wt% TiB_2 $(AlCrFeMnV)_{90}Bi_{10}$ + 15 wt% TiB_2	BCC BCC + AlV_3 + Bi BCC + AlV_3 + Bi + TiB_2 BCC + AlV_3 + Bi + TiB_2	Ball-on-disk, dry, SAE 52,100 steel, RT, 1.02 × 10^{-5}–7.02 × 10^{-5} $mm^3 \cdot N^{-1} \cdot m^{-1}$
Bhardwaj et al. [464]	AlTiZrNbHf	BCC	Pin-on-disk, dry, CGr15, RT, -
Zhao et al. [465]	$AlNbTaZr_x$ (x = 0.2–1)	BCC + HCP	Ball-on-disc, dry, Si_3N_4, RT, 1.85 × 10^{-4}–2.41 × 10^{-4} $mm^3 \cdot N^{-1} \cdot m^{-1}$
Tuten et al. [466]	TiZrHfNbTa	Amorphous	Ball-on-disc, dry, Al_2O_3, RT

Pole et al. [467]	TiZrHfTaV, TiZrTaVW	BCC	Ball-on-disk, dry, Si_3N_4, RT-500 °C, ~1 × 10^{-4}–8 × 10^{-4} $mm^3 \cdot N^{-1} \cdot m^{-1}$
Ye et al. [468]	TiZrHfNb	BCC	Nano-scratch, dry, diamond indenter, RT
Pogrebnjak et al. [469]	(TiZrHfNbV)N	FCC	Ball-on-disc, dry, Al_2O_3, 20 °C
Gong et al. [470]	TiZrHfBeCu TiZrHfBeNi $Ti_{20}Zr_{20}Hf_{20}Be_{20}Cu_{10}Ni_{10}$ $Ti_{13.8}Zr_{41.2}Ni_{10}Be_{22.5}Cu_{12.5}$	Amorphous	Nano-scratch, dry, diamond indenter, RT
Zhao et al. [471]	TiZrNiBeCu	Amorphous	Nano-scratch, dry, diamond indenter, RT
Jhong et al. [472]	$(TiZrNbCrSi)C_x$ (x = 36.7–87.8 at.%)	FCC	Ball-on-disc, dry, $100Cr_6$ steel, RT, 0.2 × 10^{-3}–3.3 × 10^{-6} $mm^3 \cdot N^{-1} \cdot m^{-1}$
Mathiou et al. [473]	TiZrNbMoTa	BCC + HCP	Ball-on disc, dry, $100Cr_6$ steel, Al_2O_3, RT, 0.154 × 10^{-1}–0.199 × 10^{-1} $mm^3 \cdot N^{-1} \cdot m^{-1}$
Petroglou et al. [474]	$MoTa_xNbVTi$ (x = 0.25–1)	BCC	Ball-on-disk, dry, $100Cr_6$ steel, RT, 0.19 × 10^{-6}–0.38 × 10^{-6} $g \cdot N^{-1} \cdot m^{-1}$
Poulia et al. [475]	MoTaNbVW	BCC	Ball-on-disc, dry, $100Cr_6$ steel & Al_2O_3, RT
Poulia et al. [476]	MoTaNbVW	BCC	Ball-on-disc, dry, $100Cr_6$ steel & Al_2O_3, RT, 1.05 × 10^{-4}–4.89 × 10^{-4} $mm^3 \cdot N^{-1} \cdot m^{-1}$
Poulia et al. [477]	MoTaNbVTi	BCC + hexagonal C14 Laves + cubic C15 laves	Ball-on disc, dry, $100Cr_6$ steel, Al_2O_3, RT
Alvi et al. [478]	MoTaWVCu	BCC	Ball-on-disc, dry, E52100 steel & Si_3N_4, RT-600 °C, 2.3 × 10^{-2}–5 × 10^{-2} $mm^3 \cdot N^{-1} \cdot m^{-1}$
Hua et al. [479]	$Ti_xZrNbTaMo$ (x = 0.5–2)	BCC	HSR-2M tester, dry, Si_3N_4, RT, 2.22 × 10^{-7}–2.42 × 10^{-7} $mm^3 \cdot N^{-1} \cdot m^{-1}$
Gu et al. [480]	$Ni_{1.5}CrFeTi_2B_{0.5}Mo_x$ (x = 0–0.25) $Ni_{1.5}CrFeTi_2B_{0.5}Mo_x$ (x = 0.5–0.25)	BCC BCC + FCC	Ball-on-disc, dry, Al_2O_3, RT, 7.99 × 10^7–2.7 × 10^7 μm^3

3.2.1. Content Variation

Tribological studies on HEAs are mostly conducted with variations in content of one element and finding the optimum concentration of the element for minimum wear rate [360,363–365,371,377–380,383,384,386,390,394,395,397,398,407,408,412,421,422,424,427,428,431,440,454,455,463,470,472,474]. Furthermore, the effect of Al content on wear properties and hardness has been studied more than any other metal. For instance, the wear resistance of CoCrFeNiCu [440], $CoCrFeNiTi_{0.5}$ [386], CoCrFeNiSi [421] and CoCrFeNiMn [364] was improved with Al addition. This was primarily ascribed to the oxide formation and hardness increase due to phase transformation, grain refinement and precipitation. Similarly, Cui et al. [398] studied the effect of $Al_xCoCrFeNiMn$ (x = 0–0.75) coatings on 4Cr5MoSiV alloys. This alloy experienced FCC to FCC + BCC transition and grain refinement when Al content increased, which in turn raised the hardness from 224 HV to 344 HV. The wear weight loss of 4Cr5MoSiV coated with $Al_xCoCrFeNiMn$ with x = 0, 0.25, 0.5 and 0.75 was measured to be 6.0 mg, 4.1 mg, 3.2 mg and 1.1 mg, respectively. Under the similar wear condition, the amount of wear weight loss of the uncoated 4Cr5MoSiV was around 10 mg. Meanwhile, Gu et al. [455] analyzed $Al_xMo_{0.5}NbFeTiMn_2$ (x = 1–2) coating on Q235 steel and found that the microhardness and wear were positively correlated to the Al content. As the Al content increased, the grain size reduced and the hardness and wear resistance increased. Kumar et al. [412] studied the wear behavior of $Al_{0.4}FeCrNiCo_x$ (x = 0–1) under oil lubricated conditions. The hardness of this alloy reduced with the increasing Co content from 377 HV (x = 0) to 199 HV (x = 1). The wear resistance of $Al_{0.4}FeCrNiCo$ was found to show a minimum among all other conditions. This alloy did not show any phase transformation until 1000 °C.

Erdogan et al. [428] investigated the influence of the Al and Ti content on the hardness and wear resistance of $Al_xCoCrFeNiTi_y$ (x = 0–0.5, y = 0–0.5). Increasing Al and Ti improved the hardness from 210 HV (for CoCrFeNi) to 859 HV (for $Al_{0.5}CoCrFeNiTi_{0.5}$). The wear rate also reduced from $2.1 \cdot 10^{-13}$ $mm^3 \cdot N^{-1} \cdot m^{-1}$ (for CoCrFeNi) to $0.25 \cdot 10^{-13}$ $mm^3 \cdot N^{-1} \cdot m^{-1}$ (for $Al_{0.5}CoCrFeNiTi_{0.5}$). CoCrFeNi initially had the FCC phase. The added Al induced and stabilized the BCC phase in the FCC matrix. Additionally, Al and Ti

formed some beneficial intermetallic phases such as AlNi and AlNiTi, which improved the hardness and wear resistance. Similarly, Chuang et al. [431] examined the influence of the Al and Ti content on the wear performance of the $Al_xCo_{1.5}CrFeNi_{1.5}Ti_y$ (x = 0–0.2, y = 0.5–1.0) alloy. They reported that the wear resistance of $Co_{1.5}CrFeNi_{1.5}Ti$ and $Al_{0.2}Co_{1.5}CrFeNi_{1.5}Ti$ was at least twice that of SUJ2 and SKH51 with the similar hardness values. Li et al. [390] studied the wear resistance of $CoCrFeNi_2V_{0.5}Ti_x$ (x = 0.5–1.25). They observed that the wear resistance and the hardness improved with the Ti content until x = 0.75 and started to decrease thereafter. $CoCrFeNi_2V_{0.5}Ti_{0.75}$ had the maximum hardness of ~960 HV and the minimum wear rate of $4.43 \cdot 10^{-5}$ $mm^3 \cdot N^{-1} \cdot m^{-1}$. Chen et al. [424] reported that the wear resistance of $Al_{0.5}CoCrFeNiCuTi_x$ (x = 0–2) increased with the Ti content until x = 1, and thereafter, it started to decrease. Here, a small content of Ti did not have much impact on wear rate, when Ti content reached x = 0.4, the BCC phase began to form which improved the hardness and wear resistance. With a Ni content of x = 0.8–1.2, the CoCr-like phases formed, which improved the wear resistance. However, after x = 1, the Ti_2Ni-like and ordered BCC phases started to appear and the alloy became harder with the increasing Ti content, which reduced the wear resistance.

Increasing the Cu content from x = 0 to x = 1 reduced the wear rate of $CoCrFeNiCu_x$ (x = 0–1) alloy from $2.3 \cdot 10^{-5}$ to $1.7 \cdot 10^{-5}$ $mm^3 \cdot N^{-1} \cdot m^{-1}$ at RT and from $2.5 \cdot 10^{-5}$ to $1.3 \cdot 10^{-5}$ $mm^3 \cdot N^{-1} \cdot m^{-1}$ at 600 °C [377]. The wear rate of CoCrFeNi (x = 0) increased with the increasing temperature. This resulted from the enhanced plastic deformation and abrasive wear due to thermal softening at higher temperatures. In contrast, the wear rate of CoCrFeNiCu (x = 1) decreased at higher temperatures. This was attributed to the self-lubricating effect of Cu. Cu also tended to form protective oxide layer which prevented direct metal to metal contact [481]. Hsu et al. [423] showed the improved wear resistance of $Al_{0.5}CoCrFeNiCuB_x$ (x = 0–1) with boron addition. $Al_{0.5}CoCrFeNiCuB$ showed the hardness of 736 HV and the maximum wear resistance of 1.76 $mm^3 \cdot N^{-1} \cdot m^{-1}$ which was higher than that of SKD61 cold-work mold (1.39 $m \cdot mm^3$) and SUJ2 bearing (1.52 $m \cdot mm^3$). The improved wear resistance was attributed to the boride formation. Similarly, Liu et al. [378] analyzed the wear resistance of $CoCrFeNiB_x$ (x = 0.5–1.5). They noticed that the increased boron reduced the wear volume from 19 down to 4.5 mm^3. The hardness increased from 550 to 1025 $HV_{0.2}$ as well with increasing boron, which was attributed to the increase in the fraction of the hard boride phase with B content. The maximum hardness was measured to be 1025 HV0.2 for $FeCoCrNiB_{1.5}$ which was higher than that of Q245R steels. Kumar et al. [408] reported that the wear rate of $Al_{0.4}FeCrNiCo_x$ (x = 0–1 mol) increased with the increasing Co content from $0.81 \cdot 10^{-4}$ $mm^3 \cdot N^{-1} \cdot m^{-1}$ (x = 0) to $1.86 \cdot 10^{-4}$ $mm^3 \cdot N^{-1} \cdot m^{-1}$ (x = 1). This was attributed to the hardness decrease form 377 HV (x = 0) to 199 HV (x = 1). As hardness decreases the wear resistance also decreases according to the Archard's law [482]. Chen et al. [454] reported how the variation of V in $Al_{0.5}CoCrFeNiCuV_x$ (x = 0–1) affected the wear performance. Here, increasing V from x = 0.6 to x = 1.2 improved the wear resistance by 20%. However, increasing V beyond x = 1.2 did not show a considerable effect. This was in line with the hardness results of this HEA. The hardness increased while x increased from x = 0.4 to x = 1 exhibiting its maximum value at x = 1. The optimal V addition was suggested to be in the range of x = 1–1.2 to improve the wear resistance.

Furthermore, improvements in the wear resistance of $CoCrFeNiNb_x$ (x = 0–1.2) [379], $(CuCrFeTiZn)_{1-x}Pb_x$ (x = 0.05–0.2) [395], $CoCrFeNiCu_x$ (x = 0–1) [377], $MoTa_xNbVTi$ (x = 0.25–1) [474] were reported. Wu et al. [410] analyzed the wear resistance of the $AlCoCrFeNiTi_x$ (x = 0, 0.5) alloy. They noticed that AlCoCrFeNi had the plate-like disordered Fe-Cr rich BCC phase embedded in the ordered Al-Ni rich BCC phase. $AlCoCrFeNiTi_{0.5}$ had the similar microstructure, but the Ti introduced honeycomb-like interdendrites which could play an important role in hindering dislocation motion. As a result, the hardness of this alloy increased from 887 $HV_{0.5}$ to 1147 $HV_{0.5}$. Additionally, the atomic radius of Ti was 1.76 Å which was larger than those of Ni (1.49 Å) and Al (1.18 Å). Hence, adding Ti to the Al-Ni-Ti rich phase might have resulted in lattice expansion or distortion.

Liu et al. [422] varied the concentration of Si in $AlCoCrFeNiSi_x$ (x = 0–0.5) coatings and found out that the microhardness of the coatings was linearly proportional to the Si concentration. The wear rate reduced significantly from ~$5.2 \cdot 10^{-4}$ to ~$1.3 \cdot 10^{-4}$ $mm^3 \cdot N^{-1} \cdot m^{-1}$ with the increasing Si content. This was attributed to the formation of wear-resistant SiO and SiO_2 layers on the wear surface. Huang et al. [373] studied $FeCoCrNiSi_x$ (x = 0–1) and found out that increasing Si content improved the hardness and wear resistance by promoting the transformation of FCC to BCC. Its microhardness increased significantly from 89.52 HV (x = 0) to 653.71 HV (x = 1) and the wear track depth decreased from 22.14 μm (x = 0) to 5.29 μm (x = 1).

Hsu et al. [456] reported that in $AlCoCrFe_xNiMo_{0.5}$ (x = 0.6–2), the wear resistance (at 500 °C) of x = 2 was much lower than that of x = 1.5 although both had similar hardness values. This was attributed to the fact that the x = 2 alloy formed a thicker oxide layer than x = 1.5 and more loose oxides abraded away from the surface. By this reasoning, the Fe content of x = 0.6–1 was recommended as over x = 1.5–2 for optimum wear resistance. Qiu et al. [458] described that the wear resistance of $Al_2CoCrFeCuTiNi_x$ (x = 0–2) first increased with the Ni content (i.e., x = 0–1) and then decreased for x = 1–2. However, the hardness monotonically increased with the increasing Ni content from ~900 HV (x = 0) to ~1100 HV (x = 2). They said that toughness and brittleness also affect the wear resistance of this alloy apart from the hardness. In this alloy, when Ni is added from x = 0–1 at% then the wear resistance increases because hardness increases. For Ni content x = 1–2 at%, the wear resistance starts to reduce because the material becomes brittle and wear happens through small brittle fracture on the surface. Beng et al. [360] analyzed the $CoCrFeNiMo_x$ (x = 0–0.3) alloy and noticed that CoCrFeNi had the FCC phase. The FCC phase was maintained even after Mo addition, but the lattice parameter (denoted by a) altered ($a_{CoCrFeNi}$ = 3.5733 Å, $a_{CoCrFeNiMo0.1}$ = 3.6016 Å, $a_{CoCrFeNiMo0.3}$ = 3.5854 Å) due to atomic size misfit between Mo and other constituents. The atomic size of Mo (1.363 Å) is distinctively larger than those of Co (1.251 Å), Cr (1.249 Å), Fe (1.241 Å) and Ni (1.246 Å) [93]. This Mo-induced lattice distortion increased the hardness from 415.2 to 465.9 HV and reduced the specific wear rate from $0.59 \cdot 10^{-3}$ to $0.33 \cdot 10^{-3}$ $mm^3 \cdot N^{-1} \cdot m^{-1}$.

Yadav et al. [397] reported the influence of Pb and Bi content in $(CuCrFeTiZn)_{100-x}Pb_x$, $(CuCrFeTiZn)_{100-x}Bi_x$ on their wear properties. Here, reductions in wear rate achieved by adding Pb and Bi were 21% and 25%, respectively. This was attributed to the fact that the soft dispersoids acted as lubricants [483]. Li et al. [413] studied $Al_{0.8}CoCrFeNiCu_{0.5}Si_x$ (x = 0–0.5) coatings. They found the specific wear rate in the range of $1.19 \cdot 10^{-6}$–$8.99 \cdot 10^{-6}$ $mm^3 \cdot N^{-1} \cdot m^{-1}$, the hardness in the range of 479–592 HV which was almost 5 to 7 times higher than the hardness of substrate 5083 Al alloy (79 $HV_{0.2}$).

Cheng et al. [394] noticed that the wear resistance and hardness of $(Fe_{0.25}Co_{0.25}Ni_{0.25}(B_{0.7}Si_{0.3})_{0.25})_{100-x}Nb_x$ (x = 0–2) coating (on Q235 steel) increased with the Nb content from x = 0 to x = 2. The measured hardness values were 587.1 $HV_{0.1}$ and 821.5 $HV_{0.1}$ for Nb content of x = 0 and x = 1, respectively. This HEA had the FCC microstructure and the grain size was refined from 3.5 μm (x = 0) to 1 μm (x = 2). This grain refinement helped to increase the hardness and wear resistance. The wear rates were measured to be $3.64 \cdot 10^{-6}$ and $1.42 \cdot 10^{-6}$ $mm^3 \cdot N^{-1} \cdot m^{-1}$ for Nb content of x = 0 and x = 2, respectively. Jones et al. [358] reported that CoCrFeNiMn showed a remarkably low wear rate of 10^{-6} $mm^3 \cdot N^{-1} \cdot m^{-1}$ with the hardness of 1.6 GPa. Zhu et al. [359] added V and Nb in equiatomic ratio into the CoCrFeNiMn (FCC phase) coating and studied the wear resistance. The measured wear rate ranged $1.85 \cdot 10^{-5}$–$6.39 \cdot 10^{-5}$ $mm^3 \cdot N^{-1} \cdot m^{-1}$ and the hardness varied in the range of 145–948.5 HV. The measured hardness values of CoCrFeNiMn, CoCrFeNiMnNb, CoCrFeNiMnV and CoCrFeNiMnNbV was 145 HV, 609 HV, 621 HV and 948 HV, respectively. Additionally, the wear rate of CoCrFeNiMn reduced from $6.39 \cdot 10^{-5}$ to $1.85 \cdot 10^{-5}$ $mm^3 \cdot N^{-1} \cdot m^{-1}$ (for CoCrFeNiMnNbV) when both Nb and V were added. These results could be attributed to the fact that Nb and V promoted the precipitation of the Laves phase (FeNb

intermetallic) and the sigma phase (CoFeV intermetallics) into the FCC matrix, which increased the hardness. Moreover, Nb and V promoted the formation of protective oxide layer on the worn surface and reduced the amount of adhesive and abrasive wear.

3.2.2. Particle Reinforcement

Hard particle reinforcement into HEAs matrix is another approach employed to improve the tribological properties. For example, adding WC into $Co_{10}Cr_{10}Fe_{40}Mn_{40}$ [382], adding TiN-Al_2O_3 into CoCrFeNiMn [277], adding NbC into AlCoCrFeNi [272], adding TiC into $CoCrCuFeNiSi_{0.2}$ [384] and $AlCoCrFeNi_{2.1}$ [416] improved the tribological performances. Such improved wear resistance was largely attributed to the increased hardness, the restrained effect of adherence abrasion, solution strengthening or microstructure refinement. Adding 10 wt% TiC particles into AlCoFeNiCu reduced the wear rate by the factor of 8 [439]. Adding TiB_2 into $(AlCrFeMnV)_{90}Bi_{10}$ resulted in ~95% decrease in wear rate due to the cumulative effect of matrix, reinforcement, refined grains and improved hardness [463]. Gou et al. [396] used CoCrFeNi (reinforced with NbC) as a metal binder for Ti (C,N)-based cermet. The hardness and fracture toughness were measured to be 1853 HV and 9.93 $MPa \cdot m^{1/2}$, respectively. The minimum wear rate was as low as $4.14 \cdot 10^{-6}$ $mm^3 \cdot N^{-1} \cdot m^{-1}$ which was attributed to the reduced grain size and improved hardness due to the solid solution strengthening effect of the HEA binder.

Ji et al. [376] improved the tribological behavior of CoCrFeNiCu by embedding MoS_2 (2–5 wt%) and WC (20–80 wt%) particles. Here, adding 2% MoS_2 improved the wear resistance and decreased the friction coefficient but adding 5% MoS_2 increased the wear rate. Adding WC continuously improved the wear resistance and 80% WC yielded the lowest wear rate. Likewise, the wear resistance of CrMnFeCoNi was improved considerably by adding 25 wt% Y_2O_3 thanks to grain boundary strengthening, Orowan looping and load transfer effect [366]. Zhou et al. [189] reported that $(FeCoCrNi)_{1-x}$ $(WC)_x$ (x = 3–11 wt%) alloy consisted of a FCC matrix and W/Cr rich carbides. The hardness increased with the WC content from 603 HV (for $(FeCoCrNi)_{0.97}$ $(WC)_{0.03}$) to 768 HV (for $(FeCoCrNi)_{0.89}$ $(WC)_{0.11}$). This was attributed to the hard WC particles and carbides precipitation into the FCC matrix. This material showed adhesive and abrasive wear. Most of the wear was caused by the debonding of WC particles.

Liu et al. [381] introduced graphene nanoplatelets into $Fe_{50}Mn_{30}Co_{10}Cr_{10}$. Adding 0.2% Graphene nanoparticles promoted self-lubricating properties because the coefficient of friction (COF) decreased by 62%, which in turn increased the wear resistance. Further addition of graphene did not have much impact on COF or self-lubricating properties. Similarly, Zhang et al. [370] added self-lubricating particles (i.e., nickel coated graphite and MoS_2 powder) into the CoCrFeNi matrix using SPS. This composite had four phases (i.e., FCC, graphite, MoS_2 and Nickel) and showed very low wear rates (~10^{-5} $mm^3 \cdot N^{-1} \cdot m^{-1}$) for the temperature range of RT-800 °C. After wear testing the worn surfaces were analyzed by Raman and EDS. They observed that graphite and MoS_2 particles were accumulated on the worn surface for temperatures RT-800 °C. They indicated that these particles helped reduce abrasive/adhesive wear. Moreover, at 600 and 800 °C, the significantly increased oxygen concentration on the worn surface facilitated the formation of a smooth glaze layer of oxide (i.e., Cr_2O_3, Fe_3O_4 etc.) and reduced the wear rate. Likewise, Zhang et al. [368] added solid lubricants (i.e., Ag, BaF_2/CaF_2 eutectic) into CoCrFeNi. This composite showed the better wear resistance (wear rates~10^{-5} $mm^3 \cdot N^{-1} \cdot m^{-1}$) than PM304 (wear rate~$10^{-4}$ $mm^3 \cdot N^{-1} \cdot m^{-1}$) [484] for the temperature range of RT-800 °C. The improved wear resistance was attributed to the solid lubricants (help to minimize friction and wear on the surface) and oxide layer (Cr_2O_3, Fe_3O_4, etc.) formation on the worn surface.

3.2.3. Use of Media and Heat Treatment

Media used during wear experiments have been proved to have considerable impact on the mechanism and rate of material removal. For example, Duan et al. [453] reported that AlCoCrFeNiCu showed more wear weight loss of ~1.2 mg when in H_2O_2 lubricant and ~0.8 mg when oil was used as media. This was because friction coefficient was lower when oil was used as a media. $FeCoCrAlNiTi_2$ showed the best wear resistance in distilled water and the worst in NaCl solutions [427]. Xiao et al. [421] noticed that the wear rates of $Al_xCoCrFeNiSi$ (x = 0.5–1.5 mol) reduced significantly from $5.5 \cdot 10^{-5}$ to $1.6 \cdot 10^{-6}$ $mm^3 \cdot N^{-1} \cdot m^{-1}$ with the increasing Al content under dry conditions. However, when water was used as a lubricant, the addition of Al content did not have a considerable impact on the wear rate. Geng et al. [369] studied the wear behavior of CoCrFeNiMn in vacuum and air in the temperature range of RT-800 °C. They found the wear rate varied in the range of $1.3 \cdot 10^{-4}$–$8 \cdot 10^{-4}$ $mm^3 \cdot N^{-1} \cdot m^{-1}$. The elements of this HEA oxidized as temperature increased. At elevated temperatures, oxides (i.e., CoO_3, CoO, $CoCrO_4$, Co_2O_3, Fe_2O_3, Cr_2O_3 and MoO_3) formed on the worn surface. From RT to 400 °C, the wear rate was higher in air than in vacuum due to peeling of the formed loose oxides. However, at 600 °C and 800 °C, robust oxides were formed, and these oxides served as a protective layer and improved the wear resistance resulting in the lower wear rate both in air than in vacuum.

The effect of heat treatment on the wear behavior of $Al_{0.5}CoCrFeNi$ was studied by Gwalani et al. [399]. They hot rolled (at 700 °C), annealed (at 1150 °C) and isothermally aged their alloy at 700 °C for 1, 4, 20, 40, 80 h. As the aging time increased, the B2 phase precipitated in the FCC matrix. These precipitates increased the hardness from ~250HV to ~302 HV, the flow stress from 668 MPa to 1352 MPa, the UTS from 1157 MPa to 1503 MPa. The wear rate of this alloy was found to be sensitive to aging. The wear rate for the sample without aging was $11 \cdot 10^{-5}$ $mm^3 \cdot N^{-1} \cdot m^{-1}$. After 80 h of aging, the wear rate reduced to $1.8 \cdot 10^{-5}$ $mm^3 \cdot N^{-1} \cdot m^{-1}$. Meanwhile, Kong et al. [419] studied the $Al_{1.8}CrCuFeNi_2$ alloy with different arc melting parameters. They varied welding current during arc melting as 410A, 455 A, 480 A, 505 A and 550 A to get different superheating. As a result, the hardness of the alloy increased from ~555 to ~625 HV when current increased from 410A to 480A. Consequently, the wear rate reduced from ~0.95 to ~0.65 $mg \cdot mm^2$. However, when the current was further increased up to 550 A, the hardness reduced to ~580 HV and the wear rate increased to ~0.72 $mg \cdot mm^2$. Here, the wear resistance of the HEA was found to be directly proportional to the hardness. Malatji et al. [263] improved the wear resistance of AlCrCuFeNi by heat treating at temperatures 800, 950 and 1100 °C. The microhardness increased from 310 to 381 HV when heat treated at 800 °C but decreased to 365 HV when heat treated at 1100 °C. Heat treatment at 1100 °C homogenized the microstructure and promoted grain coarsening. This alloy initially had the FCC phase alone. Upon heat treatment at 800 and 950 °C, the B2 phase precipitated and the hardness increased. When the alloy was heat treated at 1100 °C, some of the B2 precipitates decomposed and grain coarsened, which decreased the hardness. This explains why the wear resistant first increased and later reduced with the heat-treating temperatures. The observed wear weight was 0.002 g without heat treatment, and 0.001 g, 0.0007 g and 0.0016 g with heat treatment at 800 °C, 950 °C and 1100 °C respectively.

3.2.4. Nitriding/Carburizing/Boronizing/Sulfurization

Nitriding, carburizing, boronizing and sulfurizing have been used to improve the tribological behavior of HEAs. Pogrebnjak et al. [469] measured the wear rate of nitrided TiZrHfVNb (i.e., (TiZrHfVNb)N) and compared with the wear resistance of (AlCoCrFeNiCu)N and steel 45. The measured wear rates for (TiZrHfVNb)N and steel 45 were $0.039 \cdot 10^{-5}$ and $35.36 \cdot 10^{-5}$ $mm^3 \cdot N^{-1} \cdot m^{-1}$, respectively.

The AlCoCrFeNi alloy became more wear resistant after being nitrided [417]. The wear rates of as-cast alloy in air, water and rain media were $1.8 \cdot 10^{-4}$, $1.6 \cdot 10^{-4}$ and $0.7 \cdot 10^{-4}$

$mm^3 \cdot N^{-1} \cdot m^{-1}$, respectively. However, the wear rate of the nitrided AlCoCrFeNi in air, water and rain media were $0.39 \cdot 10^{-4}$, $0.32 \cdot 10^{-4}$ and $0.28 \cdot 10^{-4}$ $mm^3 \cdot N^{-1} \cdot m^{-1}$, respectively. The wear resistance of $(CrNbSiTiZr)C_x$ (x = 36.7–87.8 at%) was investigated by Jhong et al. [472]. Carbide coatings were deposited on CrNbSiTiZr by magnetron sputtering at various CH_4 flow ratios (3–20%). Coating with x = 36.8 at% and x = 87.8 at% showed the wear rate of $3.0 \cdot 10^{-6}$ and $0.2 \cdot 10^{-6}$ $mm^3 \cdot N^{-1} \cdot m^{-1}$, respectively. They concluded that the increase in carbon content improved the wear resistance; therefore, carbide coatings could be used as a protective layer for CrNbSiTiZr for wear application.

Cui et al. [374] sulfurized CoCrFeMoNi at 260 °C for 2 h and improved the wear resistance. After sulfurization, the weight loss by wear reduced from 15.1 mg to 4.25 mg. This was attributed to the FeS/MoS_2 lubricant phases and sulfides boundary lubricant films.

Wu et al. [406] used the pack-boronizing method to improve the wear resistance of $Al_{0.1}CoCrFeNi$ alloy. A 17.3–57.9 μm boronized layer, composed of $(Co, Fe, Ni)_2B$, CrB, Cr_2B, formed on the surface. The boronizing time varied from 2 h to 8 h. The hardness of the alloy increased gradually with the increasing boronizing time from 201 HV (0 h) to 1398 HV (8 h) and the wear rate reduced from $1.89 \cdot 10^{-4}$ to $0.22 \cdot 10^{-4}$ $mm^3 \cdot N^{-1} \cdot m^{-1}$.

Xiao et al. [363] investigated the effects of carbon content in $CoCrFeNiMnC_x$ (x = 0–1.2). The hardness was increased monotonically from 327.8 HV (x = 0) to 566.4 HV (x = 1.2) with carbon addition. They found out that the wear rates of CoCrFeNiMn and $CoCrFeNiMnC_{0.6}$ were $6.5 \cdot 10^{-3}$ $mm^3 \cdot N^{-1} \cdot m^{-1}$ and $0.47 \cdot 10^{-3}$ $mm^3 \cdot N^{-1} \cdot m^{-1}$, respectively. This alloy was comprised of the FCC (Co, Ni rich) phase and the Cr- and C- rich M7C3 carbide phases. The porosity increased with the increasing carbon content. Initially, the hardness increased until the volume fraction reached x = 0.6 due to introduction of M7C3 carbide and solid solutions of C atoms in the FCC phase. As the amount of carbon further increased, the hardness started to fall due to a significant increase in porosity. Meanwhile, Zhang et al. [385] found out that the wear rate and hardness of $(CoCrFeNiTi_{0.5})C_x$ (x = 3–12 wt%) coating were in the range of 12–24 $mg \cdot N^{-1} \cdot m^{-1}$ and 300–950 HV, respectively. This coating microstructure was made of BCC solid solution, $Cr_{23}C_6$ and TiC phases. Increase in carbon content raised the hardness due to carbides precipitates, but the wear resistance with x = 12 wt% was inferior to that with x = 6 wt% due to reduced ductility.

3.2.5. Comparison with Conventional Materials

Various HEAs have shown superior wear resistance than the commercial wear resistant materials in the following parentheses: $CuCoNiCrAl_{0.5}FeB$ (SUJ2 wear-resistant steel) [423], MoTaWNbV (Inconel-718) [475,476], TiZrHfNb (Nb and C103 ($Nb_{5.4}Hf_2Ti$)) [468], CoCrFeNiMo (HFXP-58) [372], $Al_{0.8}CrCoFeNi$ (AZ31) [411] and $Al_{0.2}Co_{1.5}CrFeNi_{1.5}Ti$ (AISI 52,100 steel and Inconel 713) [430]. $Al_3CoCrFeNi$ exhibited better wear resistance than 17–7 PH stainless steel [403], which was attributed to the precipitation of Cr_3Ni_2. CuNiSiTiZr coating improved the wear resistance of TC11 by a factor of 2.5 [393]. This improvement in hardness (and wear resistance) was resulted from the solid solutioning, precipitation and nanocomposite strengthening effects. Similarly, Al_x-CoCrFeNi (x = 0.1–3) showed 3 to 23 times higher wear resistance than SS316L steel [407]. This higher wear resistance was attributed to high hardness of $Al_xCoCrFeNi$ (~436–624 HV) than SS316L steel (~227 HV).

Many researchers formed coatings of HEAs on several commercial materials to improve their wear resistance. Zhang et al. [461] coated Ti-6Al-4V with AlTiSiVNi. They discovered that the wear resistance of AlTiSiVNi was 4 to 5 times higher than that of Ti-6Al-4V at RT and 800 °C. The hardness of AlTiSiVNi was also found to be in the range of 1151–1357 HV which was 4–6 times that of Ti-6Al-4V. The increase in hardness and wear resistance of AlTiSiVNi was attributed to the dispersion strengthening with $(Ti,V)_5Si_3$ and solution strengthening with NiAl. Huang et al. [460] coated Ti-6Al-4V with AlTiSiVCr. The microstructure of AlTiSiVCr had hard silicides $(Ti,V)_5Si_3$ dispersed into the BCC ma-

trix. The dispersed silicides improved the wear resistance of this HEA by lowering abrasive/adhesive wear. The hard BCC phase of the silicides also resisted crack propagation. While the specific wear rate for Ti-6Al-4V was ~$6.5 \cdot 10^{-5}$ to $9 \cdot 10^{-5}$ $mm^3 \cdot N^{-1} \cdot m^{-1}$, that for TiVCrAlSi ranged $2 \cdot 10^{-5}$ to $2.6 \cdot 10^{-5}$ $mm^3 \cdot N^{-1} \cdot m^{-1}$. This showed that TiVCrAlSi could become a promising anti-wear coating material for Ti-6Al-4V.

Islak et al. [391] improved the wear resistance of AISI 1040 steel with CrFeNiMoTi coating. They found that the hardness and wear rate of CrFeNiMoTi coating were ~450 HV0.3 and ~$2.732 \cdot 10^{-3}$–$3.952 \cdot 10^{-3}$ $mm^3 \cdot N^{-1} \cdot m^{-1}$, respectively. Meanwhile, the hardness and wear rate for AISI 1040 were ~200 HV0.3 and ~$8.125 \cdot 10^{-3}$–$9.455 \cdot 10^{-3}$ $mm^3 \cdot N^{-1} \cdot m^{-1}$, respectively. Gu et al. [455] analyzed $Al_xMo_{0.5}NbFeTiMn_2$ (x = 1–2) coating and found that the microhardness and wear resistance were positively related to the Al content. The increasing Al content reduced the grain size and increased both the hardness and wear resistance. The hardness of $Al_2Mo_{0.5}NbFeTiMn_2$ was measured to be 1098.5 HV0.2 which was 5 times higher than that of Q235 steel (~200 HV0.2). The high hardness was attributed to the microstructure composed of the BCC solid solution and (Nb,Ti)C carbides. The wear rates of $Al_2Mo_{0.5}NbFeTiMn_2$ and Q235 steel were measured to be ~0.3 $mg \cdot m^{-1}$ and ~0.9 $mg \cdot m^{-1}$, respectively. Liang et al. [457] deposited $AlCrFe_2Ni_2W_{0.2}Mo_{0.75}$ coating on Q235 steel used for ocean engineering equipment. This coating had the hardness of 630 HV and the specific wear rate in the range of $10.13 \cdot 10^{-6}$–$23.89 \cdot 10^{-6}$ $mm^3 \cdot N^{-1} \cdot m^{-1}$. The coating showed superior wear resistance to Q235 and SUS304 in deionized water, 3.5 wt% NaCl solution and artificial seawater media. They also reported that the electrochemical corrosion of $AlCrFe_2Ni_2W_{0.2}Mo_{0.75}$ (corrosion rate of 0.173 mm/yr) was less than both SUS304 (corrosion rate of 0.333 mm/yr) and Q235 (corrosion rate of 0.44 mm/yr).

3.2.6. Higher Temperatures Wear Resistance

HEAs have also exhibited promising tribological behaviors and thermal stability at elevated temperatures. Jin et al. [438] studied the characteristics of AlCoCuFeNi coating at temperatures up to 800 °C. This coating was mainly composed of Fe rich FCC and Cu rich BCC phases and showed good thermal stability without any phase transformation until 780 °C. Mainly Al_2O_3, Cr_2O_3, Fe_2O_3 and CuO were present in the oxide layer. Meanwhile, the weight losses of NiCrCoTiV at RT and 600 °C were measured to be 3.7 ± 0.1 mg and 3.5 ± 0.1 mg respectively [392]. The wear weight loss of 304L stainless steel was 7.7 ± 0.2 mg at RT. Fang et al. [405] used $Al_{0.3}CoCrFeNi$ as a metal binder for Ti (C,N)-based cermet. The hardness, fracture toughness and flexural strength of this cermet were 1137 HV, 6.46 $MPa \cdot m^{1/2}$ and 761 MPa at 1000 °C respectively. This superior high-temperature performance was attributed to the hindrance of the slip system and higher oxidation resistance of the HEA binder. The wear resistance of this $Al_{0.3}CoCrFeNi$ (wear groove width = 49 μm) was also better than that of the conventional Ni-Co (wear groove width = 172 μm) metal binder.

Yadav et al. [395] concluded that the wear resistance of $(CuCrFeTiZn)_{100-x}Pb_x$ improved due to oxide formation at the surface at elevated temperatures (800–1000 °C). Because these oxides made a layer on the surfaces of the HEA which helped to avoid metal to metal contact, hence reduced the material removal rate. Moreover, Chen et al. [400] said that annealed $Al_{0.6}CoCrFeNi$ showed the wear resistance higher than GCr15 by a factor of three at 600 °C. They also attributed this improved wear resistance to the formation of oxides on the surface. In this case, Fe_2O_3, Cr_2O_3, Al_2O_3 and $Al(OH)_3$, formed on the worn surfaces of $Al_xFeCrNiCo_x$ and reduced the wear rate. Alvi et al. [478] studied wear behavior of AlCoCrFeNi in the temperature range of RT-600 °C. They noticed that the oxidation of Cu (into CuO) causes wear rate decrease at 400 °C. Joseph et al. [365] analyzed wear behavior of $Al_xCoCrFeNi$ in the temperature range of RT-900 °C. The wear resistance of this HEA surpassed that of Inconel 718 at 900 °C. Here again, the wear resistance was enhanced at the higher temperatures thanks to the oxide layer formed at the contact interface.

Researchers also showed that the wear rate of HEAs increased initially and then decreased with temperature [380,401,434,467]. It was claimed that initially loose oxides formed on the surface and lower the wear rate up to moderately high temperatures. As temperature increased higher, such loose oxides were damaged by thermal softening and therefore, the wear rate increased. In contrast, other studies reported the opposite behaviors. The wear resistance initially decreased up to moderately high temperatures and then increased at higher temperatures. This behavior was attributed to the formation of a thicker and more robust oxide layer on the worn surface which reduced the area of direct metal to metal contact. For instance, Pole et al. [467] studied the wear resistance of refractory HEAs, TiZrHfTaV and TiZrTaVW in the temperature range of RT-500 °C. The hardness of these HEAs (6–8.1 GPa) was found to be larger than two times that of SS304. The measured wear rate of these alloy was in the range of $0.5 \cdot 10^{-5}$–$8 \cdot 10^{-4}$ $mm^3 \cdot N^{-1} \cdot m^{-1}$. Various oxides, such as ZrO_2, TiO_2, Ta_2O_5, V_2O_5, HfO_2 and WO_3, formed on the worn surface. The wear rate increased until 150 °C due to the formation of a delicate oxide layer at the worn surface. However, as the temperature increased further from 150 to 500 °C, a strong protective oxide layer formed on the worn surface and the wear rate reduced for both refractory HEAs. Similar findings were reported by Lobel et al. [434] for the wear resistance of $AlCoCrFeNiTi_{0.5}$ coating in the temperature range of RT-900 °C. The depth of wear increased from ~62 μm at RT to ~82 μm at 500 °C, and afterwards it decreased down to ~50 μm at 900 °C. As the temperature increased, a loose oxides layer formed on the worn surface at lower temperatures. As temperature increased, a stronger oxides protective layer formed and it reduced material loss. Similarly, $CoCrFeNiNb_x$ showed good resistance to thermal softening by showing less reduction in hardness (i.e., 35% from RT to 1000 °C) [380]. Here, the wear resistance decreased from RT to 400 °C and then increased. This improvement above 400 °C was attributed to the oxide layer formation at higher temperatures which lead to reduction in wear rates of the $CoCrFeNiNb_{0.65}$ and $CoCrFeNiNb_{0.8}$. By a similar mechanism, the wear rate of $Al_{0.25}CoCrFeNi$ increased from RT to 300 °C due to thermal softening but it decreased thereafter due to oxides formation at the contact surface [401].

Some HEAs showed fluctuation in wear resistance due to microstructural transformations at elevated temperatures. The wear rate of $Al_{0.6}TiCrFeCoNi$ increased from RT to 300 °C and reduced from 300 °C to 500 °C, mainly due to phase transformation (i.e., the formation of sigma-CrFe) at higher temperatures [435]. Such phase transformation at higher temperatures could also significantly reduce fracture toughness. The wear resistance of $(CoCrFeMnNi)_{85}Ti_{15}$ increased from RT to 400 °C and then decreased thereafter [367]. Miao et al. [415] studied the wear behavior of $AlCoCrFeNi_{2.1}$ with different antagonist materials (i.e., Al_2O_3, Si_3N_4 and GCr15). They also analyzed wear rate of the same composition for a temperature range of RT-900 °C against SiC. The wear rate of $AlCoCrFeNi_{2.1}$ against Al_2O_3, Si_3N_4 and GCr15 is ~$42 \cdot 10^{-5}$, ~$37 \cdot 10^{-5}$, ~$32.5 \cdot 10^{-5}$ $mm^3 \cdot N^{-1} \cdot m^{-1}$. The hardness of Al_2O_3, Si_3N_4 and GCr15 is 2300, 1500 and 680 HV, and the wear rate of $AlCoCrFeNi_{2.1}$ increased with the hardness of the antagonist material. Moreover, the wear rate of $AlCoCrFeNi_{2.1}$ (against SiC) increased from ~$75 \cdot 10^{-6}$ to ~$140 \cdot 10^{-6}$ $mm^3 \cdot N^{-1} \cdot m^{-1}$ when temperature increased from RT to 900 °C. This increased wear rate with temperature was attributed to the thermal softening. Joseph et al. [355] noticed that when the wear resistance of CoCrFeNiMn was examined at high temperatures, ultrafine grains and the sigma phase formed at the contact surface, which resulted in the improved wear resistance.

4. Summery and Future Direction

This review covers recent advances in the development and manufacturing of HEAs and their performances under extreme environments such as nuclear and wear applications. The HEAs were tabulated based on manufacturing methods, irradiation responses and wear performances.

The most widely used method for HEAs manufacturing was arc melting due to its simplicity, when the idea of HEAs was conceptualized. However, recently AM processes

(SLM, EBM and DED) have gained interest since they may potentially provide more freedom in shape and in properties by changing process parameters. However, there are some issues that need to be resolved. For instance, low productivity, formation of micro-level defects such as pores or unfused particle boundaries, residual stresses, composition shift due to selective evaporation of constituents with lower vapor pressure, lack of standards for quality evaluation, high initial investment cost and more. With these issues being gradually resolved, AM could make a powerful and versatile manufacturing method to fabricate application-specific HEAs with desired properties for some compositions. Most of the AM HEAs are studied in the as-cast state (after AM). In terms of HEAs characterization, most studies focused on the microstructure using SEM, tensile behavior and hardness. Structural characterization at a smaller length scale, using transmission electron microscope, would be helpful to better understand the structural evolution under various loadings. In order to identify the effect of manufacturing methods and explore more applications for HEAs, more research is needed on creep properties, dislocation behaviors, deformation microstructures, compressive strength, fatigue and more.

Structural materials for next generation nuclear reactors must survive high energy irradiation at high temperatures with reasonable service life. Similar to other structural metals, high energy irradiation on HEAs often induces microstructural changes which in turn deteriorated their mechanical properties including hardness, swelling or embrittlement. For a number of cases of HEAs, their compositional complexity hinders such microstructural degradation and results in superior irradiation resistance compared to other conventional alloys. This makes them promising candidate materials for nuclear applications. However, more studies must be conducted on the irradiation behaviors of HEAs to better understand their applicability to the next generation nuclear reactors. To date, very little is known about HEAs phase diagrams and equilibrium phases. In addition, the defect generation and movement mechanism as a result of irradiation are not clearly understood.

HEAs have also demonstrated superior tribological performances over a wide range of temperatures from RT to high temperatures in comparison to the commercial materials (i.e., Steel, Inconel, Ti-6Al-4V, Q235, SUS304 etc.). Moreover, the wear behavior of HEAs is affected by composition, particle reinforcement, media, nitriding/carburizaing/sulfurizing treatments, temperature and oxides formation. Most of the wear studies are on cantor alloy or its derivatives; therefore, more elements and combinations are needed to be explored to further understand potential candidates for wear applications. For the wear resistant applications where the weight is not a critical factor, refractory high entropy alloys would make a good option thanks to their high hardness [466–480]. Most of these alloys are equimolar. The equimolar ratios are probably a good point to start but they might not be the best to get the highest potential out of the particular element composition. Non-equimolar refractory HEAs are worth more exploration.

HEAs are being researched for more than a decade and are not yet commercially available. One reason could be because HEAs could not be manufactured with most widely used processes suitable for mass production (i.e., casting, molding etc.). Arc melting (most popular manufacturing method for HEAs) is limited to manufacture laboratory-scale samples for testing. Recently, a number of attempts have been made to fabricate HEAs using AM techniques. Some AM HEAs showed the improved mechanical properties. However, there are still many issues that need to be addressed for AM to be used for mass production of HEAs.

Overall, there are still a great number of possible HEAs compositions that are to be studied. Apart from cantor alloy, the characteristics of the majority of other HEAs have not been investigated well enough for safe practical applications. These studies cannot be used to generalize characteristics for HEAs but we can take them as screening efforts. Moreover, it is not practical to perform all the characterization studies on all these compositions. Therefore, it would be more reasonable to use simulations and material informatics to screen compositions before experimental studies instead of using trial and error.

Author Contributions: Conceptualization, S.S. and J.L.; methodology, S.S.; software, S.S.; validation, J.L. and S.S.; formal analysis, S.S.; investigation, S.S.; resources, S.S.; data curation, S.S.; writing—original draft preparation, S.S.; writing—review and editing, J.L.; visualization, S.S.; supervision, J.L.; project administration, J.L.; funding acquisition, J.L. All authors have read and agreed to the published version of the manuscript.

Funding: This research received no external funding.

Institutional Review Board Statement: Not applicable.

Informed Consent Statement: Not applicable.

Data Availability Statement: The authors declare that the data supporting the findings of this study are available within the article.

Conflicts of Interest: The authors declare no conflict of interest.

References

1. Radetzki, M. Seven thousand years in the service of humanity—The history of copper, the red metal. *Elsevier* **2009**, *34*, 176–184. https://doi.org/10.1016/j.resourpol.2009.03.003.
2. Murty, B.; Yeh, J.; Ranganathan, S.; Bhattacharjee, P. *High-Entropy Alloys*; Elsevier: Amsterdam, The Netherlands, 2019.
3. Yeh, J.W.; Chen, S.K.; Lin, S.J.; Gan, J.Y.; Chin, T.S.; Shun, T.T.; Tsau, C.H.; Chang, S.Y. Nanostructured high-entropy alloys with multiple principal elements: Novel alloy design concepts and outcomes. *Adv. Eng. Mater.* **2004**, *6*, 299–303. https://doi.org/10.1002/adem.200300567.
4. Achard, F.C. *Recherches sur les Propriétés des Alliages Métalliques*; Decker: Berlin, Germany, 1788, IV, 37.
5. Smith, C.S. Four outstanding researches in metallurgical history. *Am. Soc. Test. Mater.* **1963**.
6. Vincent, A.J.B. *A Study of Three Multicomponent Alloys*; University of Sussex: Brighton, UK, 1981.
7. Huang, K.H.; Yeh, J. *A Study on the Multicomponent Alloy Systems Containing Equal-Mole Elements*; National Tsing Hua University: Hsinchu, Taiwan, 1996.
8. Ranganathan, S. Alloyed pleasures: Multimetallic cocktails. *Curr. Sci.* **2003**, *85*, 1404–1406.
9. Cantor, B.; Chang, I.T.H.; Knight, P.; Vincent, A.J.B. Microstructural development in equiatomic multicomponent alloys. *Mater. Sci. Eng. A* **2004**, *375–377*, 213–218. https://doi.org/10.1016/j.msea.2003.10.257.
10. Greer, A.L. Confusion by design. *Nature* **1993**, *366*, 303–304. https://doi.org/10.1038/366303a0.
11. Gao, M.C.; Liaw, P.K.; Yeh, J.W.; Zhang, Y. *High-Entropy Alloys: Fundamentals and Applications*; Springer: Cham, Switzerland, 2016; ISBN 9783319270135.
12. Cantor, B. Multicomponent and high entropy alloys. *Entropy* **2014**, *16*, 4749–4768. https://doi.org/10.3390/e16094749.
13. Yeh, J.W. Recent progress in high-entropy alloys. *Ann. Chim. Sci.* **2006**, *31*, 633–648. https://doi.org/10.3166/acsm.31.633-648.
14. Yeh, J.W. Physical Metallurgy of High-Entropy Alloys. *JOM* **2015**, *67*, 2254–2261.
15. Zhang, W.; Liaw, P.K.; Zhang, Y. Science and technology in high-entropy alloys. *Sci. China Mater.* **2018**, *61*, 2–22. https://doi.org/10.1007/s40843-017-9195-8.
16. Sharma, A.S.; Yadav, S.; Biswas, K.; Basu, B. High-entropy alloys and metallic nanocomposites: Processing challenges, microstructure development and property enhancement. *Mater. Sci. Eng. R Rep.* **2018**, *131*, 1–42. https://doi.org/10.1016/j.mser.2018.04.003.
17. Basu, I.; De Hosson, J.T.M. High Entropy Alloys: Ready to Set Sail? *Metals* **2020**, *10*, 194. https://doi.org/10.3390/met10020194.
18. Reddy, C.K.; Gopi Krishna, M.; Srikant, P. Brief evolution story and some basic limitations of high entropy alloys (HEAs)—A review. *Mater. Today: Proc.* **2019**, *18*, 436–439.
19. Yeh, J.W.; Chen, Y.L.; Lin, S.J.; Chen, S.K. High-entropy alloys—A new era of exploitation. *Mater. Sci. Forum* **2007**, *560*, 1–9. https://doi.org/10.4028/www.scientific.net/MSF.560.1.
20. Pickering, E.J.; Jones, N.G. High-entropy alloys: A critical assessment of their founding principles and future prospects. *Int. Mater. Rev.* **2016**, *61*, 183–202. https://doi.org/10.1080/09506608.2016.1180020.
21. Tian, F. A review of solid-solution models of high-entropy alloys based on Ab initio calculations. *Front. Mater.* **2017**, *4*, 36. https://doi.org/10.3389/fmats.2017.00036.
22. George, E.P.; Raabe, D.; Ritchie, R.O. High-entropy alloys. *Nat. Rev. Mater.* **2019**, *4*, 5151–5534. https://doi.org/10.1038/s41578-019-0121-4.
23. Lu, Z.P.; Wang, H.; Chen, M.W.; Baker, I.; Yeh, J.W.; Liu, C.T.; Nieh, T.G. An assessment on the future development of high-entropy alloys: Summary from a recent workshop. *Intermetallics* **2015**, *66*, 67–76. https://doi.org/10.1016/j.intermet.2015.06.021.
24. Troparevsky, M.C.; Morris, J.R.; Daene, M.; Wang, Y.; Lupini, A.R.; Stocks, G.M. Beyond Atomic Sizes and Hume-Rothery Rules: Understanding and Predicting High-Entropy Alloys. *JOM* **2015**, *67*, 2350–2363. https://doi.org/10.1007/s11837-015-1594-2.
25. Ye, Y.F.; Wang, Q.; Lu, J.; Liu, C.T.; Yang, Y. High-entropy alloy: Challenges and prospects. *Mater. Today* **2016**, *19*, 349–362. https://doi.org/10.1016/j.mattod.2015.11.026.
26. Miracle, D.B.; Senkov, O.N. A critical review of high entropy alloys and related concepts. *Acta Mater.* **2017**, *122*, 448–511. https://doi.org/10.1016/j.actamat.2016.08.081.

27. Miracle, D.B. High-Entropy Alloys: A Current Evaluation of Founding Ideas and Core Effects and Exploring "Nonlinear Alloys." *JOM* **2017**, *69*, 2130–2136.
28. Ge, H.; Tian, F. A Review of Ab Initio Calculation on Lattice Distortion in High-Entropy Alloys. *JOM* **2019**, *71*, 4225–4237. https://doi.org/10.1007/s11837-019-03777-1.
29. Zhang, Y.; Yang, X.; Liaw, P.K. Alloy design and properties optimization of high-entropy alloys. *JOM* **2012**, *64*, 830–838. https://doi.org/10.1007/s11837-012-0366-5.
30. Yeh, J.W. Alloy design strategies and future trends in high-entropy alloys. *JOM* **2013**, *65*, 1759–1771. https://doi.org/10.1007/s11837-013-0761-6.
31. Tsai, M.H. Three strategies for the design of advanced high-entropy alloys. *Entropy* **2016**, *18*, 252. https://doi.org/1099-4300/18/7/252.
32. Zhang, Y.; Zhou, Y.J.; Lin, J.P.; Chen, G.L.; Liaw, P.K. Solid-solution phase formation rules for multi-component alloys. *Adv. Eng. Mater.* **2008**, *10*, 534–538. https://doi.org/10.1002/adem.200700240.
33. Guo, S.; Liu, C.T. Phase stability in high entropy alloys: Formation of solid-solution phase or amorphous phase. *Prog. Nat. Sci. Mater. Int.* **2011**, *21*, 433–446. https://doi.org/10.1016/S1002-0071(12)60080-X.
34. Gao, M.C.; Zhang, C.; Gao, P.; Zhang, F.; Ouyang, L.Z.; Widom, M.; Hawk, J.A. Thermodynamics of concentrated solid solution alloys. *Curr. Opin. Solid State Mater. Sci.* **2017**, *21*, 238–251. https://doi.org/10.1016/j.cossms.2017.08.001.
35. Kozak, R.; Sologubenko, A.; Steurer, W. Single-phase high-entropy alloys—An overview. *Z. Fur Krist.* **2015**, *230*, 55–68. https://doi.org/10.1515/zkri-2014-1739.
36. Diao, H.; Santodonato, L.J.; Tang, Z.; Egami, T.; Liaw, P.K. Local Structures of High-Entropy Alloys (HEAs) on Atomic Scales: An Overview. *JOM* **2015**, *67*, 2321–2325. https://doi.org/10.1007/s11837-015-1591-5.
37. Zhang, Y.; Zuo, T.T.; Tang, Z.; Gao, M.C.; Dahmen, K.A.; Liaw, P.K.; Lu, Z.P. Microstructures and properties of high-entropy alloys. *Prog. Mater. Sci.* **2014**, *61*, 1–93. https://doi.org/10.1016/j.pmatsci.2013.10.001.
38. Huang, W.; Martin, P.; Zhuang, H.L. Machine-learning phase prediction of high-entropy alloys. *Acta Mater.* **2019**, *169*, 225–236. https://doi.org/10.1016/j.actamat.2019.03.012.
39. Ganesh, U.L.; Raghavendra, H. Review on the transition from conventional to multi-component-based nano-high-entropy alloys—NHEAs. *J. Therm. Anal. Calorim.* **2020**, *139*, 207–216. https://doi.org/10.1007/s10973-019-08360-z.
40. Lyu, Z.; Lee, C.; Wang, S.Y.; Fan, X.; Yeh, J.W.; Liaw, P.K. Effects of Constituent Elements and Fabrication Methods on Mechanical Behavior of High-Entropy Alloys: A Review. *Metall. Mater. Trans. A Phys. Metall. Mater. Sci.* **2019**, *50*, 1–28. https://doi.org/10.1007/s11661-018-4970-z.
41. Li, Z.; Raabe, D. Strong and Ductile Non-equiatomic High-Entropy Alloys: Design, Processing, Microstructure, and Mechanical Properties. *JOM* **2017**, *69*, 2099–2106. https://doi.org/10.1007/s11837-017-2540-2.
42. Li, Z.; Zhao, S.; Ritchie, R.O.; Meyers, M.A. Mechanical properties of high-entropy alloys with emphasis on face-centered cubic alloys. *Prog. Mater. Sci.* **2019**, *102*, 296–345. https://doi.org/10.1016/j.pmatsci.2018.12.003.
43. Praveen, S.; Kim, H.S. High-Entropy Alloys: Potential Candidates for High-Temperature Applications—An Overview. *Adv. Eng. Mater.* **2018**, *20*, 1700645.
44. Cao, B.; Yang, T.; Liu, W.; Liu, C.T. Precipitation-hardened high-entropy alloys for high-temperature applications: A critical review. *MRS Bull.* **2019**, *44*, 854–859. https://doi.org/10.1557/mrs.2019.255.
45. Huang, E.W.; Hung, G.Y.; Lee, S.Y.; Jain, J.; Chang, K.P.; Chou, J.J.; Yang, W.C.; Liaw, P.K. Mechanical and magnetic properties of the high-entropy alloys for combinatorial approaches. *Crystals* **2020**, *10*, 200. https://doi.org/10.3390/cryst10030200.
46. Tsai, M.H. Physical properties of high entropy alloys. *Entropy* **2013**, *15*, 5338–5345. https://doi.org/10.3390/e15125338.
47. Wu, Z.; Troparevsky, M.C.; Gao, Y.F.; Morris, J.R.; Stocks, G.M.; Bei, H. Phase stability, physical properties and strengthening mechanisms of concentrated solid solution alloys. *Curr. Opin. Solid State Mater. Sci.* **2017**, *21*, 267–284. https://doi.org/10.1016/j.cossms.2017.07.001.
48. Toda-Caraballo, I.; Wróbel, J.S.; Nguyen-Manh, D.; Pérez, P.; Rivera-Díaz-del-Castillo, P.E.J. Simulation and Modeling in High Entropy Alloys. *JOM* **2017**, *69*, 2137–2149. https://doi.org/10.1007/s11837-017-2524-2.
49. Zhao, S.; Weber, W.J.; Zhang, Y. Unique Challenges for Modeling Defect Dynamics in Concentrated Solid-Solution Alloys. *JOM* **2017**, *69*, 2084–2091. https://doi.org/10.1007/s11837-017-2461-0.
50. Torralba, J.M.; Alvaredo, P.; García-Junceda, A. High-entropy alloys fabricated via powder metallurgy. A critical review. *Powder Metall.* **2019**, *62*, 84–114. https://doi.org/10.1080/00325899.2019.1584454.
51. Chen, S.; Tong, Y.; Liaw, P.K. Additive manufacturing of high-entropy alloys: A review. *Entropy* **2018**, *20*, 937. https://doi.org/10.3390/e20120937.
52. Guo, J.; Tang, C.; Rothwell, G.; Li, L.; Wang, Y.C.; Yang, Q.; Ren, X. Welding of high entropy alloys—A review. *Entropy* **2019**, *21*, 431. https://doi.org/10.3390/e21040431.
53. Lopes, J.G.; Oliveira, J.P. A short review on welding and joining of high entropy alloys. *Metals* **2020**, *10*, 212. https://doi.org/10.3390/met10020212.
54. Filho, F.C.G.; Monteiro, S.N. Welding joints in high entropy alloys: A short-review on recent trends. *Materials* **2020**, *13*, 1411. https://doi.org/10.3390/ma13061411.
55. Scutelnicu, E.; Simion, G.; Rusu, C.C.; Corneliu Gheonea, M.; Voiculescu, I.; Geanta, V. High Entropy Alloys Behaviour During Welding. *Rev. Chim* **2020**, *71*, 219–233. https://doi.org/10.37358/Rev.

56. Dong, W.; Zhou, Z.; Zhang, M.; Ma, Y.; Yu, P.; Liaw, P.K.; Li, G. Applications of high-pressure technology for high-entropy alloys: A review. *Metals* **2019**, *9*, 876. https://doi.org/10.3390/met9080867.
57. Dąbrowa, J.; Danielewski, M. State-of-the-art diffusion studies in the high entropy alloys. *Metals* **2020**, *10*, 347. https://doi.org/10.3390/met10030347.
58. Chen, S.; Wang, J.; Xia, L.; Wu, Y. Deformation behavior of bulk metallic glasses and high entropy alloys under complex stress fields: A review. *Entropy* **2019**, *21*, 54. https://doi.org/10.3390/e21010054.
59. Diao, H.Y.; Feng, R.; Dahmen, K.A.; Liaw, P.K. Fundamental deformation behavior in high-entropy alloys: An overview. *Curr. Opin. Solid State Mater. Sci.* **2017**, *21*, 252–266. https://doi.org/10.1016/j.cossms.2017.08.003.
60. Shi, Y.; Yang, B.; Liaw, P.K. Corrosion-resistant high-entropy alloys: A review. *Metals* **2017**, *7*, 43. https://doi.org/10.3390/met7020043.
61. Qiu, Y.; Thomas, S.; Gibson, M.A.; Fraser, H.L.; Birbilis, N. Corrosion of high entropy alloys. *npj Mater. Degrad.* **2017**, *1*, 15. https://doi.org/10.1038/s41529-017-0009-y.
62. Chen, P.Y.; Lee, C.; Wang, S.Y.; Seifi, M.; Lewandowski, J.J.; Dahmen, K.A.; Jia, H.L.; Xie, X.; Chen, B.L.; Yeh, J.W.; et al. Fatigue behavior of high-entropy alloys: A review. *Sci. China Technol. Sci.* **2018**, *61*, 168–178. https://doi.org/10.1007/s11431-017-9137-4.
63. Li, W.; Wang, G.; Wu, S.; Liaw, P.K. Creep, fatigue, and fracture behavior of high-entropy alloys. *J. Mater. Res.* **2018**, *33*, 3011–3034. https://doi.org/10.1557/jmr.2018.191.
64. Zhang, Y.; Zhao, S.; Weber, W.J.; Nordlund, K.; Granberg, F.; Djurabekova, F. Atomic-level heterogeneity and defect dynamics in concentrated solid-solution alloys. *Curr. Opin. Solid State Mater. Sci.* **2017**, *21*, 221–237. https://doi.org/10.1016/j.cossms.2017.02.002.
65. Yang, T.; Li, C.; Zinkle, S.J.; Zhao, S.; Bei, H.; Zhang, Y. Irradiation responses and defect behavior of single-phase concentrated solid solution alloys. *J. Mater. Res.* **2018**, *33*, 3077–3091.
66. Jin, K.; Bei, H. Single-phase concentrated solid-solution alloys: Bridging intrinsic transport properties and irradiation resistance. *Front. Mater.* **2018**, *5*, 26. https://doi.org/10.3389/fmats.2018.00026.
67. Senkov, O.N.; Miracle, D.B.; Chaput, K.J.; Couzinie, J.P. Development and exploration of refractory high entropy alloys—A review. *J. Mater. Res.* **2018**, *33*, 3092–3128. https://doi.org/10.1557/jmr.2018.153.
68. Ram Prabhu, T.; Chodancar, Y.; Arivarasu, M.; Arivazhagan, N.; Mishra, R.K. High Entropy Based Composites—An Overview. *Mater. Sci. Forum* **2019**, *969*, 98–113. https://doi.org/10.4028/www.scientific.net/MSF.969.98.
69. Oses, C.; Toher, C.; Curtarolo, S. High-entropy ceramics. *Nat. Rev. Mater.* **2020**, *5*, 295–309. https://doi.org/10.1038/s41578-019-0170-8.
70. Motallebzadeh, A.; Peighambardoust, N.S.; Sheikh, S.; Murakami, H.; Guo, S.; Canadinc, D. Microstructural, mechanical and electrochemical characterization of TiZrTaHfNb and $Ti_{1.5}ZrTa_{0.5}Hf_{0.5}Nb_{0.5}$ refractory high-entropy alloys for biomedical applications. *Intermetallics* **2019**, *113*, 106572. https://doi.org/10.1016/j.intermet.2019.106572.
71. Akmal, M.; Hussain, A.; Afzal, M.; Lee, Y.I.; Ryu, H.J. Systematic Study of $(MoTa)_xNbTiZr$ Medium- and High-Entropy Alloys for Biomedical Implants- In Vivo Biocompatibility Examination. *J. Mater. Sci. Technol.* **2021**, *78*, 183–191. https://doi.org/10.1016/j.jmst.2020.10.049.
72. Fu, M.; Ma, X.; Zhao, K.; Li, X.; Su, D. High-entropy materials for energy-related applications. *Iscience* **2021**, *24*, 102177. https://doi.org/10.1016/j.isci.2021.102177.
73. Canter, N. *High-Entropy Alloys*; Elsevier: London, UK, 2015; Volume 71, ISBN 9780128160671.
74. Gopinath, V.M.; Arulvel, S. A review on the steels, alloys/high entropy alloys, composites and coatings used in high temperature wear applications. *Mater. Today Proc.* **2020**, *43*, 817–823. https://doi.org/10.1016/j.matpr.2020.06.495.
75. Voiculescu, I.; Geanta, V.; Stanciu, E.M.; Jianu, D.A.; Postolache, C.; Fugaru, V. Effect of irradiation and temperature on microstructural characteristic of FeCrAl alloys. *Acta Phys. Pol. A* **2018**, *134*, 116–118. https://doi.org/10.12693/APhysPolA.134.116.
76. Zhang, Y.; Qiao, J.W.; Liaw, P.K. A Brief Review of High Entropy Alloys and Serration Behavior and Flow Units. *J. Iron Steel Res. Int.* **2016**, *23*, 2–6. https://doi.org/10.1016/S1006-706X(16)30002-4.
77. López Ríos, M.; Socorro Perdomo, P.P.; Voiculescu, I.; Geanta, V.; Crăciun, V.; Boerasu, I.; Mirza Rosca, J.C. Effects of nickel content on the microstructure, microhardness and corrosion behavior of high-entropy $AlCoCrFeNi_x$ alloys. *Sci. Rep.* **2020**, *10*, 21119. https://doi.org/10.1038/s41598-020-78108-5.
78. Shi, H.; Fetzer, R.; Jianu, A.; Weisenburger, A.; Heinzel, A.; Lang, F.; Müller, G. Influence of alloying elements (Cu, Ti, Nb) on the microstructure and corrosion behaviour of AlCrFeNi-based high entropy alloys exposed to oxygen-containing molten Pb. *Corros. Sci.* **2021,** *190*, 109659. https://doi.org/10.1016/j.corsci.2021.109659.
79. Thorhallsson, A.I.; Csáki, I.; Geambazu, L.E.; Magnus, F.; Karlsdottir, S.N. Effect of alloying ratios and Cu-addition on corrosion behaviour of CoCrFeNiMo high-entropy alloys in superheated steam containing CO2, H2S and HCl. Corros. Sci. **2021**, *178*, 109083. https://doi.org/10.1016/j.corsci.2020.109083.
80. Lu, Y.; Huang, H.; Gao, X.; Ren, C.; Gao, J.; Zhang, H.; Zheng, S.; Jin, Q.; Zhao, Y.; Lu, C.; et al. A promising new class of irradiation tolerant materials: Ti2ZrHfV0.5Mo0.2 high-entropy alloy. *J. Mater. Sci. Technol.* **2019**, *35*, 369–373. https://doi.org/10.1016/j.jmst.2018.09.034.
81. Chen, D.; Tong, Y.; Wang, J.; Han, B.; Zhao, Y.L.; He, F.; Kai, J.J. Microstructural response of He^+ irradiated $FeCoNiCrTi_{0.2}$ high-entropy alloy. *J. Nucl. Mater.* **2018**, *510*, 187–192. https://doi.org/10.1016/j.jnucmat.2018.08.006.
82. Yang, T.; Xia, S.; Liu, S.; Wang, C.; Liu, S.; Fang, Y.; Zhang, Y.; Xue, J.; Yan, S.; Wang, Y. Precipitation behavior of $Al_xCoCrFeNi$ high entropy alloys under ion irradiation. *Sci. Rep.* **2016**, *6*, 32146. https://doi.org/10.1038/srep32146.

83. Xia, S.; Gao, M.C.; Yang, T.; Liaw, P.K.; Zhang, Y. Phase stability and microstructures of high entropy alloys ion irradiated to high doses. *J. Nucl. Mater.* **2016**, *480*, 100–108. https://doi.org/10.1016/j.jnucmat.2016.08.017.
84. Alshataif, Y.A.; Sivasankaran, S.; Al-Mufadi, F.A.; Alaboodi, A.S.; Ammar, H.R. Manufacturing Methods, Microstructural and Mechanical Properties Evolutions of High-Entropy Alloys: A Review. *Met. Mater. Int.* **2019**, *26*, 1099–1133. https://doi.org/10.1007/s12540-019-00565-z.
85. He, Q.F.; Tang, P.H.; Chen, H.A.; Lan, S.; Wang, J.G.; Luan, J.H.; Du, M.; Liu, Y.; Liu, C.T.; Pao, C.W.; et al. Understanding chemical short-range ordering/demixing coupled with lattice distortion in solid solution high entropy alloys. Acta Mater. **2021**, *216*, 117140. https://doi.org/10.1016/j.actamat.2021.117140.
86. Stepanov, N.D.; Yurchenko, N.Y.; Zherebtsov, S. V.; Tikhonovsky, M.A.; Salishchev, G.A. Aging behavior of the HfNbTaTiZr high entropy alloy. *Mater. Lett.* **2018**, *211*, 87–90. https://doi.org/10.1016/j.matlet.2017.09.094.
87. Tsai, C.W.; Chen, Y.L.; Tsai, M.H.; Yeh, J.W.; Shun, T.T.; Chen, S.K. Deformation and annealing behaviors of high-entropy alloy $Al_{0.5}$CoCrCuFeNi. *J. Alloys Compd.* **2009**, *486*, 427–435. https://doi.org/10.1016/j.jallcom.2009.06.182.
88. Zhang, K.B.; Fu, Z.Y.; Zhang, J.Y.; Shi, J.; Wang, W.M.; Wang, H.; Wang, Y.C.; Zhang, Q.J. Annealing on the structure and properties evolution of the CoCrFeNiCuAl high-entropy alloy. *J. Alloys Compd.* **2010**, *502*, 295–299. https://doi.org/10.1016/j.jallcom.2009.11.104.
89. Bhattacharjee, P.P.; Sathiaraj, G.D.; Zaid, M.; Gatti, J.R.; Lee, C.; Tsai, C.W.; Yeh, J.W. Microstructure and texture evolution during annealing of equiatomic CoCrFeMnNi high-entropy alloy. *J. Alloys Compd.* **2014**, *587*, 544–552. https://doi.org/10.1016/j.jallcom.2013.10.237.
90. Stepanov, N.D.; Yurchenko, N.Y.; Tikhonovsky, M.A.; Salishchev, G.A. Effect of carbon content and annealing on structure and hardness of the CoCrFeNiMn-based high entropy alloys. *J. Alloys Compd.* **2016**, *687*, 59–71. https://doi.org/10.1016/j.jallcom.2016.06.103.
91. Zhang, K.; Fu, Z. Effects of annealing treatment on phase composition and microstructure of CoCrFeNiTiAl_x high-entropy alloys. *Intermetallics* **2012**, *22*, 24–32. https://doi.org/10.1016/j.intermet.2011.10.010.
92. Haase, C.; Barrales-Mora, L.A. Influence of deformation and annealing twinning on the microstructure and texture evolution of face-centered cubic high-entropy alloys. *Acta Mater.* **2018**, *150*, 88–103. https://doi.org/10.1016/j.actamat.2018.02.048.
93. Niu, Z.; Wang, Y.; Geng, C.; Xu, J.; Wang, Y. Microstructural evolution, mechanical and corrosion behaviors of as-annealed CoCrFeNiMo$_x$ (x = 0, 0.2, 0.5, 0.8, 1) high entropy alloys. *J. Alloys Compd.* **2020**, *820*, 153273. https://doi.org/10.1016/j.jallcom.2019.153273.
94. Abbasi, E.; Dehghani, K. Microstructure and mechanical properties of $Co_{19}Cr_{20}Fe_{20}Mn_{21}Ni_{19}$ and $Co_{19}Cr_{20}Fe_{20}Mn_{21}Ni_{19}Nb_{0.06}C_{0.8}$ high-entropy/compositionally-complex alloys after annealing. *Mater. Sci. Eng. A* **2020**, *772*, 138812. https://doi.org/10.1016/j.msea.2019.138812.
95. Sathiaraj, G.D.; Pukenas, A.; Skrotzki, W. Texture formation in face-centered cubic high-entropy alloys. *J. Alloys Compd.* **2020**, *826*, 154183. https://doi.org/10.1016/j.jallcom.2020.154183.
96. Munitz, A.; Meshi, L.; Kaufman, M.J. Heat treatments' effects on the microstructure and mechanical properties of an equiatomic Al-Cr-Fe-Mn-Ni high entropy alloy. *Mater. Sci. Eng. A* **2017**, *689*, 384–394. https://doi.org/10.1016/j.msea.2017.02.072.
97. Tang, Q.H.; Huang, Y.; Huang, Y.Y.; Liao, X.Z.; Langdon, T.G.; Dai, P.Q. Hardening of an $Al_{0.3}$CoCrFeNi high entropy alloy via high-pressure torsion and thermal annealing. *Mater. Lett.* **2015**, *151*, 126–129. https://doi.org/10.1016/j.matlet.2015.03.066.
98. Lin, D.; Xu, L.; Jing, H.; Han, Y.; Zhao, L.; Minami, F. Effects of annealing on the structure and mechanical properties of FeCoCrNi high-entropy alloy fabricated via selective laser melting. *Addit. Manuf.* **2020**, *32*, 101058. https://doi.org/10.1016/j.addma.2020.101058.
99. Shahmir, H.; He, J.; Lu, Z.; Kawasaki, M.; Langdon, T.G. Effect of annealing on mechanical properties of a nanocrystalline CoCrFeNiMn high-entropy alloy processed by high-pressure torsion. *Mater. Sci. Eng. A* **2016**, *676*, 294–303. https://doi.org/10.1016/j.msea.2016.08.118.
100. Xu, J.; Zhang, J.Y.; Wang, Y.Q.; Zhang, P.; Kuang, J.; Liu, G.; Zhang, G.J.; Sun, J. Annealing-dependent microstructure, magnetic and mechanical properties of high-entropy FeCoNi$Al_{0.5}$ alloy. *Mater. Sci. Eng. A* **2020**, *776*, 139003. https://doi.org/10.1016/j.msea.2020.139003.
101. Ma, Y.; Peng, G.J.; Wen, D.H.; Zhang, T.H. Nanoindentation creep behavior in a CoCrFeCuNi high-entropy alloy film with two different structure states. *Mater. Sci. Eng. A* **2015**, *621*, 111–117. https://doi.org/10.1016/j.msea.2014.10.065.
102. Ma, S.G.; Qiao, J.W.; Wang, Z.H.; Yang, H.J.; Zhang, Y. Microstructural features and tensile behaviors of the $Al_{0.5}$CrCuFeNi2 high-entropy alloys by cold rolling and subsequent annealing. *Mater. Des.* **2015**, *88*, 1057–1062. https://doi.org/10.1016/j.matdes.2015.09.092.
103. Zhuang, Y.X.; Xue, H.D.; Chen, Z.Y.; Hu, Z.Y.; He, J.C. Effect of annealing treatment on microstructures and mechanical properties of FeCoNiCuAl high entropy alloys. *Mater. Sci. Eng. A* **2013**, *572*, 30–35. https://doi.org/10.1016/j.msea.2013.01.081.
104. Niu, S.; Kou, H.; Guo, T.; Zhang, Y.; Wang, J.; Li, J. Strengthening of nanoprecipitations in an annealed Al0.5CoCrFeNi high entropy alloy. *Mater. Sci. Eng. A* **2016**, *671*, 82–86. https://doi.org/10.1016/j.msea.2016.06.040.
105. Gwalani, B.; Gorsse, S.; Choudhuri, D.; Styles, M.; Zheng, Y.; Mishra, R.S.; Banerjee, R. Modifying transformation pathways in high entropy alloys or complex concentrated alloys via thermo-mechanical processing. *Acta Mater.* **2018**, *153*, 169–185. https://doi.org/10.1016/j.actamat.2018.05.009.

106. Wani, I.S.; Bhattacharjee, T.; Sheikh, S.; Bhattacharjee, P.P.; Guo, S.; Tsuji, N. Tailoring nanostructures and mechanical properties of $AlCoCrFeNi_{2.1}$ eutectic high entropy alloy using thermo-mechanical processing. *Mater. Sci. Eng. A* **2016**, *675*, 99–109. https://doi.org/10.1016/j.msea.2016.08.048.
107. Wani, I.S.; Sathiaraj, G.D.; Ahmed, M.Z.; Reddy, S.R.; Bhattacharjee, P.P. Evolution of microstructure and texture during thermo-mechanical processing of a two phase $Al_{0.5}CoCrFeMnNi$ high entropy alloy. *Mater. Charact.* **2016**, *118*, 417–424. https://doi.org/10.1016/j.matchar.2016.06.021.
108. Sathiaraj, G.D.; Bhattacharjee, P.P. Effect of starting grain size on the evolution of microstructure and texture during thermo-mechanical processing of CoCrFeMnNi high entropy alloy. *J. Alloys Compd.* **2015**, *647*, 82–96. https://doi.org/10.1016/j.jallcom.2015.06.009.
109. Munitz, A.; Salhov, S.; Guttmann, G.; Derimow, N.; Nahmany, M. Heat treatment influence on the microstructure and mechanical properties of $AlCrFeNiTi_{0.5}$ high entropy alloys. *Mater. Sci. Eng. A* **2019**, *742*, 1–14. https://doi.org/10.1016/j.msea.2018.10.114.
110. Zhang, Y.; Jiang, X.; Sun, H.; Shao, Z. Effect of annealing heat treatment on microstructure and mechanical properties of nonequiatomic CoCrFeNiMo medium-entropy alloys prepared by hot isostatic pressing. *Nanotechnol. Rev.* **2020**, *9*, 580–595. https://doi.org/10.1515/ntrev-2020-0047.
111. Li, Z.; Fu, L.; Zheng, H.; Yu, R.; Lv, L.; Sun, Y.; Dong, X.; Shan, A. Effect of Annealing Temperature on Microstructure and Mechanical Properties of a Severe Cold-Rolled FeCoCrNiMn High-Entropy Alloy. *Metall. Mater. Trans. A Phys. Metall. Mater. Sci.* **2019**, *50*, 3223–3237. https://doi.org/10.1007/s11661-019-05231-y.
112. Zhang, M.; Zhou, X.; Wang, D.; Zhu, W.; Li, J.; Zhao, Y.F. AlCoCuFeNi high-entropy alloy with tailored microstructure and outstanding compressive properties fabricated via selective laser melting with heat treatment. *Mater. Sci. Eng. A* **2019**, *743*, 773–784. https://doi.org/10.1016/j.msea.2018.11.118.
113. Lin, C.M.; Tsai, H.L.; Bor, H.Y. Effect of aging treatment on microstructure and properties of high-entropy $Cu_{0.5}CoCrFeNi$ alloy. *Intermetallics* **2010**, *18*, 1244–1250. https://doi.org/10.1016/j.intermet.2010.03.030.
114. Wen, L.H.; Kou, H.C.; Li, J.S.; Chang, H.; Xue, X.Y.; Zhou, L. Effect of aging temperature on microstructure and properties of AlCoCrCuFeNi high-entropy alloy. *Intermetallics* **2009**, *17*, 266–269. https://doi.org/10.1016/j.intermet.2008.08.012.
115. Ren, B.; Liu, Z.X.; Cai, B.; Wang, M.X.; Shi, L. Aging behavior of a $CuCr_2Fe_2NiMn$ high-entropy alloy. *Mater. Des.* **2012**, *33*, 121–126. https://doi.org/10.1016/j.matdes.2011.07.005.
116. Na, T.W.; Park, K.B.; Lee, S.Y.; Yang, S.M.; Kang, J.W.; Lee, T.W.; Park, J.M.; Park, K.; Park, H.K. Preparation of spherical TaNbHfZrTi high-entropy alloy powders by a hydrogenation–dehydrogenation reaction and thermal plasma treatment. *J. Alloys Compd.* **2020**, *817*, 152757. https://doi.org/10.1016/j.jallcom.2019.152757.
117. Zhang, H.; He, Y.; Pan, Y. Enhanced hardness and fracture toughness of the laser-solidified $FeCoNiCrCuTiMoAlSiB_{0.5}$ high-entropy alloy by martensite strengthening. *Scr. Mater.* **2013**, *69*, 342–345. https://doi.org/10.1016/j.scriptamat.2013.05.020.
118. Yang, J.; Jo, Y.H.; Kim, D.W.; Choi, W.M.; Kim, H.S.; Lee, B.J.; Sohn, S.S.; Lee, S. Effects of transformation-induced plasticity (TRIP) on tensile property improvement of $Fe_{45}Co_{30}Cr_{10}V_{10}Ni_{5-x}Mn_x$ high-entropy alloys. *Mater. Sci. Eng. A* **2020**, *772*, 138809. https://doi.org/10.1016/j.msea.2019.138809.
119. Lilensten, L.; Couzinié, J.P.; Perrière, L.; Bourgon, J.; Emery, N.; Guillot, I. New structure in refractory high-entropy alloys. *Mater. Lett.* **2014**, *132*, 123–125. https://doi.org/10.1016/j.matlet.2014.06.064.
120. Aryal, A.; Dubenko, I.; Talapatra, S.; Granovsky, A.; Lähderanta, E.; Stadler, S.; Ali, N. Magnetic field dependence of the martensitic transition and magnetocaloric effects in Ni49BiMn35In15. *AIP Adv.* **2020**, *10*, 015138. https://doi.org/10.1063/1.5130405.
121. Li, R.X.; Liaw, P.K.; Zhang, Y. Synthesis of $Al_xCoCrFeNi$ high-entropy alloys by high-gravity combustion from oxides. *Mater. Sci. Eng. A* **2017**, *707*, 668–673. https://doi.org/10.1016/j.msea.2017.09.101.
122. Chen, C.; Zhang, H.; Hu, S.; Wei, R.; Wang, T.; Cheng, Y.; Zhang, T.; Shi, N.; Li, F.; Guan, S.; et al. Influences of laser surface melting on microstructure, mechanical properties and corrosion resistance of dual-phase Cr–Fe–Co–Ni–Al high entropy alloys. *J. Alloys Compd.* **2020**, *826*, 154100. https://doi.org/10.1016/j.jallcom.2020.154100.
123. He, J.Y.; Wang, H.; Wu, Y.; Liu, X.J.; Mao, H.H.; Nieh, T.G.; Lu, Z.P. Precipitation behavior and its effects on tensile properties of FeCoNiCr high-entropy alloys. *Intermetallics* **2016**, *79*, 41–52. https://doi.org/10.1016/j.intermet.2016.09.005.
124. Zhang, K.; Wen, H.; Zhao, B.; Dong, X.; Zhang, L. Precipitation behavior and its impact on mechanical properties in an aged carbon-containing $Al_{0.3}Cu_{0.5}CrFeNi_2$ high-entropy alloy. *Mater. Charact.* **2019**, *155*, 109792. https://doi.org/10.1016/j.matchar.2019.109792.
125. Liu, W.H.; Yang, T.; Liu, C.T. Precipitation hardening in CoCrFeNi-based high entropy alloys. *Mater. Chem. Phys.* **2018**, *210*, 2–11. https://doi.org/10.1016/j.matchemphys.2017.07.037.
126. He, J.Y.; Wang, H.; Huang, H.L.; Xu, X.D.; Chen, M.W.; Wu, Y.; Liu, X.J.; Nieh, T.G.; An, K.; Lu, Z.P. A precipitation-hardened high-entropy alloy with outstanding tensile properties. *Acta Mater.* **2016**, *102*, 187–196. https://doi.org/10.1016/j.actamat.2015.08.076.
127. Park, J.M.; Kang, J.W.; Lee, W.H.; Lee, S.Y.; Min, S.H.; Ha, T.K.; Park, H.K. Preparation of spherical WTaMoNbV refractory high entropy alloy powder by inductively-coupled thermal plasma. *Mater. Lett.* **2019**, *255*, 126513. https://doi.org/10.1016/j.matlet.2019.126513.
128. Zhang, F.; Lou, H.; Cheng, B.; Zeng, Z.; Zeng, Q. High-Pressure Induced Phase Transitions in High-Entropy Alloys: A Review. *Entropy* **2019**, *21*, 239. https://doi.org/10.3390/e21030239.
129. Shahmir, H.; He, J.; Lu, Z.; Kawasaki, M.; Langdon, T.G. Evidence for superplasticity in a CoCrFeNiMn high-entropy alloy processed by high-pressure torsion. *Mater. Sci. Eng. A* **2017**, *685*, 342–348. https://doi.org/10.1016/j.msea.2017.01.016.

130. Haušild, P.; Čížek, J.; Čech, J.; Zýka, J.; Kim, H.S. INDENTATION SIZE EFFECT IN HIGH PRESSURE TORSION PROCESSED HIGH ENTROPY ALLOY. *Acta Polytech. CTU Proc.* **2020**, *27*, 141–144. https://doi.org/10.14311/APP.2020.27.0141.
131. Zhang, K.; Peng, S.; Li, N.; Liu, X.; Zhang, M.; Wu, Y.D.; Yang, Y.; Greenberg, E.; Prakapenka, V.B.; Hui, X.; et al. Tuning to more compressible phase in TiZrHfNb high entropy alloy by pressure. *Appl. Phys. Lett.* **2020**, *116*, 031901. https://doi.org/10.1063/1.5136022.
132. Sonkusare, R.; Biswas, K.; Al-Hamdany, N.; Brokmeier, H.G.; Kalsar, R.; Schell, N.; Gurao, N.P. A critical evaluation of microstructure-texture-mechanical behavior heterogeneity in high pressure torsion processed CoCuFeMnNi high entropy alloy. *Mater. Sci. Eng. A* **2020**, *782*, 139187. https://doi.org/10.1016/j.msea.2020.139187.
133. Podolskiy, A. V.; Shapovalov, Y.O.; Tabachnikova, E.D.; Tortika, A.S.; Tikhonovsky, M.A.; Joni, B.; Ódor, E.; Ungar, T.; Maier, S.; Rentenberger, C.; et al. Anomalous Evolution of Strength and Microstructure of High-Entropy Alloy CoCrFeNiMn after High-Pressure Torsion at 300 and 77 K. *Adv. Eng. Mater.* **2020**, *22*, 1900752. https://doi.org/10.1002/adem.201900752.
134. Skrotzki, W.; Pukenas, A.; Odor, E.; Joni, B.; Ungar, T.; Völker, B.; Hohenwarter, A.; Pippan, R.; George, E.P. Microstructure, texture, and strength development during high-pressure torsion of crmnfeconi high-entropy alloy. *Crystals* **2020**, *10*, 336. https://doi.org/10.3390/cryst10040336.
135. Asghari-Rad, P.; Sathiyamoorthi, P.; Thi-Cam Nguyen, N.; Bae, J.W.; Shahmir, H.; Kim, H.S. Fine-tuning of mechanical properties in $V_{10}Cr_{15}Mn_5Fe_{35}Co_{10}Ni_{25}$ high-entropy alloy through high-pressure torsion and annealing. *Mater. Sci. Eng. A* **2020**, *771*, 138604. https://doi.org/10.1016/j.msea.2019.138604.
136. Ahmad, A.S.; Su, Y.; Liu, S.Y.; Ståhl, K.; Wu, Y.D.; Hui, X.D.; Ruett, U.; Gutowski, O.; Glazyrin, K.; Liermann, H.P.; et al. Structural stability of high entropy alloys under pressure and temperature. *J. Appl. Phys.* **2017**, *121*, 235901. https://doi.org/10.1063/1.4984796.
137. LuŽnik, J.; KoŽelj, P.; Vrtnik, S.; Jelen, A.; Jagličić, Z.; Meden, A.; Feuerbacher, M.; Dolinšek, J. Complex magnetism of Ho-Dy-Y-Gd-Tb hexagonal high-entropy alloy. *Phys. Rev. B Condens. Matter Mater. Phys.* **2015**, *92*, 224201. https://doi.org/10.1103/PhysRevB.92.224201.
138. Feuerbacher, M.; Heidelmann, M.; Thomas, C. Hexagonal High-entropy Alloys. *Mater. Res. Lett.* **2014**, *3*, 1–6. https://doi.org/10.1080/21663831.2014.951493.
139. Heczel, A.; Kawasaki, M.; Lábár, J.L.; Jang, J. il; Langdon, T.G.; Gubicza, J. Defect structure and hardness in nanocrystalline CoCrFeMnNi High-Entropy Alloy processed by High-Pressure Torsion. *J. Alloys Compd.* **2017**, *711*, 143–154. https://doi.org/10.1016/j.jallcom.2017.03.352.
140. Kilmametov, A.; Kulagin, R.; Mazilkin, A.; Seils, S.; Boll, T.; Heilmaier, M.; Hahn, H. High-pressure torsion driven mechanical alloying of CoCrFeMnNi high entropy alloy. *Scr. Mater.* **2019**, *158*, 29–33. https://doi.org/10.1016/j.scriptamat.2018.08.031.
141. Asghari-Rad, P.; Sathiyamoorthi, P.; Bae, J.W.; Moon, J.; Park, J.M.; Zargaran, A.; Kim, H.S. Effect of grain size on the tensile behavior of V10Cr15Mn5Fe35Co10Ni25 high entropy alloy. *Mater. Sci. Eng. A* **2019**, *744*, 610–617. https://doi.org/10.1016/j.msea.2018.12.077.
142. Edalati, P.; Floriano, R.; Tang, Y.; Mohammadi, A.; Pereira, K.D.; Luchessi, A.D.; Edalati, K. Ultrahigh hardness and biocompatibility of high-entropy alloy TiAlFeCoNi processed by high-pressure torsion. *Mater. Sci. Eng. C* **2020**, *112*, 110908. https://doi.org/10.1016/j.msec.2020.110908.
143. Yu, P.F.; Zhang, L.J.; Cheng, H.; Zhang, H.; Ma, M.Z.; Li, Y.C.; Li, G.; Liaw, P.K.; Liu, R.P. The high-entropy alloys with high hardness and soft magnetic property prepared by mechanical alloying and high-pressure sintering. *Intermetallics* **2016**, *70*, 82–87. https://doi.org/10.1016/j.intermet.2015.11.005.
144. Tracy, C.L.; Park, S.; Rittman, D.R.; Zinkle, S.J.; Bei, H.; Lang, M.; Ewing, R.C.; Mao, W.L. High pressure synthesis of a hexagonal close-packed phase of the high-entropy alloy CrMnFeCoNi. *Nat. Commun.* **2017**, *8*, 15634 . https://doi.org/10.1038/ncomms15634.
145. Liu, W.H.; Tong, Y.; Chen, S.W.; Xu, W.W.; Wu, H.H.; Zhao, Y.L.; Yang, T.; Wang, X.L.; Liu, X.; Kai, J.J.; et al. Unveiling the Electronic Origin for Pressure-Induced Phase Transitions in High-Entropy Alloys. *Matter* **2020**, *2*, 751–763. https://doi.org/10.1016/j.matt.2019.12.023.
146. Yu, P.F.; Zhang, L.J.; Ning, J.L.; Ma, M.Z.; Zhang, X.Y.; Li, Y.C.; Liaw, P.K.; Li, G.; Liu, R.P. Pressure-induced phase transitions in HoDyYGdTb high-entropy alloy. *Mater. Lett.* **2017**, *196*, 137–140. https://doi.org/10.1016/j.matlet.2017.02.136.
147. Zhang, F.; Lou, H.; Chen, S.; Chen, X.; Zeng, Z.; Yan, J.; Zhao, W.; Wu, Y.; Lu, Z.; Zeng, Q. Effects of non-hydrostaticity and grain size on the pressure-induced phase transition of the CoCrFeMnNi high-entropy alloy. *J. Appl. Phys.* **2018**, *124*, 115901. https://doi.org/10.1063/1.5046180.
148. Zhang, F.X.; Zhao, S.; Jin, K.; Bei, H.; Popov, D.; Park, C.; Neuefeind, J.C.; Weber, W.J.; Zhang, Y. Pressure-induced fcc to hcp phase transition in Ni-based high entropy solid solution alloys. *Appl. Phys. Lett.* **2017**, *110*, 011902. https://doi.org/10.1063/1.4973627.
149. Cheng, B.; Zhang, F.; Lou, H.; Chen, X.; Liaw, P.K.; Yan, J.; Zeng, Z.; Ding, Y.; Zeng, Q. Pressure-induced phase transition in the AlCoCrFeNi high-entropy alloy. *Scr. Mater.* **2019**, *161*, 88–92. https://doi.org/10.1016/j.scriptamat.2018.10.020.
150. Zhang, C.; Bhandari, U.; Zeng, C.; Ding, H.; Guo, S.; Yan, J.; Yang, S. Carbide formation in refractory Mo15Nb20Re15Ta30W20 alloy under a combined high-pressure and high-temperature condition. *Entropy* **2020**, *22*, 718. https://doi.org/10.3390/e22070718.
151. Tillmann, W.; Ulitzka, T.; Wojarski, L.; Manka, M.; Ulitzka, H.; Wagstyl, D. Development of high entropy alloys for brazing applications. *Weld. World* **2020**, *64*, 201–208. https://doi.org/10.1007/s40194-019-00824-y.

152. Liu, R.; Wang, Z.; Sparks, T.; Liou, F.; Newkirk, J. Aerospace applications of laser additive manufacturing. In *Laser Additive Manufacturing: Materials, Design, Technologies, and Applications*; Brandt, M., Ed.; Matthew Deans; Woodhead Publishing: Sawston, England, 2017; pp. 351–371, ISBN 9780081004340.
153. Zhu, Z.G.; Nguyen, Q.B.; Ng, F.L.; An, X.H.; Liao, X.Z.; Liaw, P.K.; Nai, S.M.L.; Wei, J. Hierarchical microstructure and strengthening mechanisms of a CoCrFeNiMn high entropy alloy additively manufactured by selective laser melting. *Scr. Mater.* **2018**, *154*, 20–24. https://doi.org/10.1016/j.scriptamat.2018.05.015.
154. Park, J.M.; Choe, J.; Kim, J.G.; Bae, J.W.; Moon, J.; Yang, S.; Kim, K.T.; Yu, J.H.; Kim, H.S. Superior tensile properties of 1%C-CoCrFeMnNi high-entropy alloy additively manufactured by selective laser melting. *Mater. Res. Lett.* **2020**, *8*, 1–7. https://doi.org/10.1080/21663831.2019.1638844.
155. Zhou, R.; Liu, Y.; Zhou, C.; Li, S.; Wu, W.; Song, M.; Liu, B.; Liang, X.; Liaw, P.K. Microstructures and mechanical properties of C-containing FeCoCrNi high-entropy alloy fabricated by selective laser melting. *Intermetallics* **2018**, *94*, 165–171. https://doi.org/10.1016/j.intermet.2018.01.002.
156. Brif, Y.; Thomas, M.; Todd, I. The use of high-entropy alloys in additive manufacturing. *Scr. Mater.* **2015**, *99*, 93–96. https://doi.org/10.1016/j.scriptamat.2014.11.037.
157. Peyrouzet, F.; Hachet, D.; Soulas, R.; Navone, C.; Godet, S.; Gorsse, S. Selective Laser Melting of $Al_{0.3}$CoCrFeNi High-Entropy Alloy: Printability, Microstructure, and Mechanical Properties. *JOM* **2019**, *71*, 3443–3451. https://doi.org/10.1007/s11837-019-03715-1.
158. Sun, K.; Peng, W.; Yang, L.; Fang, L. Effect of SLM processing parameters on microstructures and mechanical properties of Al0.5CoCrFeNi high entropy alloys. *Metals* **2020**, *10*, 292. https://doi.org/10.3390/met10020292.
159. Wang, J.; Niu, S.; Guo, T.; Kou, H.; Li, J. The FCC to BCC phase transformation kinetics in an $Al_{0.5}$CoCrFeNi high entropy alloy. *J. Alloys Compd.* **2017**, *710*, 144–150. https://doi.org/10.1016/j.jallcom.2017.03.249.
160. Zhou, P.F.; Xiao, D.H.; Wu, Z.; Ou, X.Q. $Al_{0.5}$FeCoCrNi high entropy alloy prepared by selective laser melting with gas-atomized pre-alloy powders. *Mater. Sci. Eng. A* **2019**, *739*, 86–89. https://doi.org/10.1016/j.msea.2018.10.035.
161. Li, X. Additive Manufacturing of Advanced Multi-Component Alloys: Bulk Metallic Glasses and High Entropy Alloys. *Adv. Eng. Mater.* **2018**, *20*, 1490. https://doi.org/10.1002/adem.201700874.
162. Li, X.P.; Wang, X.J.; Saunders, M.; Suvorova, A.; Zhang, L.C.; Liu, Y.J.; Fang, M.H.; Huang, Z.H.; Sercombe, T.B. A selective laser melting and solution heat treatment refined Al-12Si alloy with a controllable ultrafine eutectic microstructure and 25% tensile ductility. *Acta Mater.* **2015**, *95*, 74–82. https://doi.org/10.1016/j.actamat.2015.05.017.
163. Li, X.P.; Ji, G.; Chen, Z.; Addad, A.; Wu, Y.; Wang, H.W.; Vleugels, J.; Van Humbeeck, J.; Kruth, J.P. Selective laser melting of nano-TiB_2 decorated $AlSi_{10}Mg$ alloy with high fracture strength and ductility. *Acta Mater.* **2017**, *129*, 183–193. https://doi.org/10.1016/j.actamat.2017.02.062.
164. Attar, H.; Bönisch, M.; Calin, M.; Zhang, L.C.; Scudino, S.; Eckert, J. Selective laser melting of in situ titanium-titanium boride composites: Processing, microstructure and mechanical properties. *Acta Mater.* **2014**, *76*, 13–22. https://doi.org/10.1016/j.actamat.2014.05.022.
165. Vrancken, B.; Thijs, L.; Kruth, J.P.; Van Humbeeck, J. Microstructure and mechanical properties of a novel β titanium metallic composite by selective laser melting. *Acta Mater.* **2014**, *68*, 150–158. https://doi.org/10.1016/j.actamat.2014.01.018.
166. Li, X.P.; Van Humbeeck, J.; Kruth, J.P. Selective laser melting of weak-textured commercially pure titanium with high strength and ductility: A study from laser power perspective. *Mater. Des.* **2017**, *116*, 352–358. https://doi.org/10.1016/j.matdes.2016.12.019.
167. Wang, Q.; Ren, L.; Li, X.; Zhang, S.; Sercombe, T.B.; Yang, K. Antimicrobial Cu-bearing stainless steel scaffolds. *Mater. Sci. Eng. C* **2016**, *68*, 519–522. https://doi.org/10.1016/j.msec.2016.06.038.
168. Sercombe, T.B.; Li, X. Selective laser melting of aluminium and aluminium metal matrix composites: Review. *Mater. Technol.* **2016**, *31*, 77–85. https://doi.org/10.1179/1753555715Y.0000000078.
169. Niu, P.; Li, R.; Zhu, S.; Wang, M.; Chen, C.; Yuan, T. Hot cracking, crystal orientation and compressive strength of an equimolar CoCrFeMnNi high-entropy alloy printed by selective laser melting. *Opt. Laser Technol.* **2020**, *127*, 106147. https://doi.org/10.1016/j.optlastec.2020.106147.
170. Karlsson, D.; Marshal, A.; Johansson, F.; Schuisky, M.; Sahlberg, M.; Schneider, J.M.; Jansson, U. Elemental segregation in an AlCoCrFeNi high-entropy alloy—A comparison between selective laser melting and induction melting. *J. Alloys Compd.* **2019**, *784*, 195–203. https://doi.org/10.1016/j.jallcom.2018.12.267.
171. Cui, W.; Zhang, X.; Liou, F. Additive Manufacturing of High-Entropy Alloys—A Review. In Proceedings of the Solid Freeform Fabrication 2017 the 28th Solid Freeform Fabrication 2017; Rolla, MO, USA, August 7-9, **2017**, pp. 712–724.
172. Ostovari Moghaddam, A.; Shaburova, N.A.; Samodurova, M.N.; Abdollahzadeh, A.; Trofimov, E.A. Additive manufacturing of high entropy alloys: A practical review. *J. Mater. Sci. Technol.* **2021,** 77, 131–162. https://doi.org/10.1016/j.jmst.2020.11.029.
173. Yeh, M.C.G.J.; Liaw, P.K.; Zhang, Y. *High-Entropy Alloys*; Elsevier: Amsterdam, The Netherlands, 2016; ISBN 9783319270111.
174. Riva, S.; Brown, S.G.R.; Lavery, N.P.; Tudball, A.; Yusenko, and K. V. *Spark Plasma Sintering of Materials*; Cavaliere, P., Ed.; Springer Nature Switzerland: Lecce, Italy, 2019; ISBN 978-3-030-05326-0.
175. Vaidya, M.; Muralikrishna, G.M.; Murty, B.S. High-entropy alloys by mechanical alloying: A review. *J. Mater. Res.* **2019**, *34*, 664–686.
176. Chen, P.; Li, S.; Zhou, Y.; Yan, M.; Attallah, M.M. Fabricating CoCrFeMnNi high entropy alloy via selective laser melting in-situ alloying. *J. Mater. Sci. Technol.* **2020**, *43*, 40–43. https://doi.org/10.1016/j.jmst.2020.01.002.

177. Li, B.; Zhang, L.; Xu, Y.; Liu, Z.; Qian, B.; Xuan, F. Selective laser melting of CoCrFeNiMn high entropy alloy powder modified with nano-TiN particles for additive manufacturing and strength enhancement: Process, particle behavior and effects. *Powder Technol.* **2020**, *360*, 509–521. https://doi.org/10.1016/j.powtec.2019.10.068.
178. Li, N.; Wu, S.; Ouyang, D.; Zhang, J.; Liu, L. Fe-based metallic glass reinforced FeCoCrNiMn high entropy alloy through selective laser melting. *J. Alloys Compd.* **2020**, *822*, 153695. https://doi.org/10.1016/j.jallcom.2020.153695.
179. Li, B.; Zhang, L.; Yang, B. Grain refinement and localized amorphization of additively manufactured high-entropy alloy matrix composites reinforced by nano ceramic particles via selective-laser-melting/remelting. *Compos. Commun.* **2020**, *19*, 56–60. https://doi.org/10.1016/j.coco.2020.03.001.
180. Kim, J.G.; Park, J.M.; Seol, J.B.; Choe, J.; Yu, J.H.; Yang, S.; Kim, H.S. Nano-scale solute heterogeneities in the ultrastrong selectively laser melted carbon-doped CoCrFeMnNi alloy. *Mater. Sci. Eng. A* **2020**, *773*, 138726. https://doi.org/10.1016/j.msea.2019.138726.
181. Li, B.; Qian, B.; Xu, Y.; Liu, Z.; Xuan, F. Fine-structured CoCrFeNiMn high-entropy alloy matrix composite with 12 wt% TiN particle reinforcements via selective laser melting assisted additive manufacturing. *Mater. Lett.* **2019**, *252*, 88–91. https://doi.org/10.1016/j.matlet.2019.05.108.
182. Piglione, A.; Dovgyy, B.; Liu, C.; Gourlay, C.M.; Hooper, P.A.; Pham, M.S. Printability and microstructure of the CoCrFeMnNi high-entropy alloy fabricated by laser powder bed fusion. *Mater. Lett.* **2018**, *224*, 22–25. https://doi.org/10.1016/j.matlet.2018.04.052.
183. Xu, Z.; Zhang, H.; Li, W.; Mao, A.; Wang, L.; Song, G.; He, Y. Microstructure and nanoindentation creep behavior of CoCrFeMnNi high-entropy alloy fabricated by selective laser melting. *Addit. Manuf.* **2019**, *28*, 766–771. https://doi.org/10.1016/j.addma.2019.06.012.
184. Ren, J.; Mahajan, C.; Liu, L.; Follette, D.; Chen, W.; Mukherjee, S. Corrosion behavior of selectively laser melted CoCrFeMnNi high entropy alloy. *Metals* **2019**, *9*, 1029. https://doi.org/10.3390/met9101029.
185. Dovgyy, B.; Pham, M.S. Epitaxial growth in 316L steel and CoCrFeMnNi high entropy alloy made by powder-bed laser melting. *AIP Conf. Proc.* **2018**, *1960*, 140008. https://doi.org/10.1063/1.5035000.
186. Wu, W.; Zhou, R.; Wei, B.; Ni, S.; Liu, Y.; Song, M. Nanosized precipitates and dislocation networks reinforced C-containing CoCrFeNi high-entropy alloy fabricated by selective laser melting. *Mater. Charact.* **2018**, *144*, 605–610. https://doi.org/10.1016/j.matchar.2018.08.019.
187. Sun, Z.; Tan, X.P.; Descoins, M.; Mangelinck, D.; Tor, S.B.; Lim, C.S. Revealing hot tearing mechanism for an additively manufactured high-entropy alloy via selective laser melting. *Scr. Mater.* **2019**, *168*, 129–133. https://doi.org/10.1016/j.scriptamat.2019.04.036.
188. Song, M.; Zhou, R.; Gu, J.; Wang, Z.; Ni, S.; Liu, Y. Nitrogen induced heterogeneous structures overcome strength-ductility trade-off in an additively manufactured high-entropy alloy. *Appl. Mater. Today* **2020**, *18*, 100498. https://doi.org/10.1016/j.apmt.2019.100498.
189. Zhou, R.; Chen, G.; Liu, B.; Wang, J.; Han, L.; Liu, Y. Microstructures and wear behaviour of $(FeCoCrNi)_{1-x}(WC)_x$ high entropy alloy composites. *Int. J. Refract. Met. Hard Mater.* **2018**, *75*, 56–62. https://doi.org/10.1016/j.ijrmhm.2018.03.019.
190. Niu, P.D.; Li, R.D.; Yuan, T.C.; Zhu, S.Y.; Chen, C.; Wang, M.B.; Huang, L. Microstructures and properties of an equimolar AlCoCrFeNi high entropy alloy printed by selective laser melting. *Intermetallics* **2019**, *104*, 24–32. https://doi.org/10.1016/j.intermet.2018.10.018.
191. Luo, S.; Gao, P.; Yu, H.; Yang, J.; Wang, Z.; Zeng, X. Selective laser melting of an equiatomic AlCrCuFeNi high-entropy alloy: Processability, non-equilibrium microstructure and mechanical behavior. *J. Alloys Compd.* **2019**, *771*, 387–397. https://doi.org/10.1016/j.jallcom.2018.08.290.
192. Luo, S.; Zhao, C.; Su, Y.; Liu, Q.; Wang, Z. Selective laser melting of dual phase $AlCrCuFeNi_x$ high entropy alloys: Formability, heterogeneous microstructures and deformation mechanisms. *Addit. Manuf.* **2020**, *31*, 100925. https://doi.org/10.1016/j.addma.2019.100925.
193. Yao, H.; Tan, Z.; He, D.; Zhou, Z.; Zhou, Z.; Xue, Y.; Cui, L.; Chen, L.; Wang, G.; Yang, Y. High strength and ductility AlCrFeNiV high entropy alloy with hierarchically heterogeneous microstructure prepared by selective laser melting. *J. Alloys Compd.* **2020**, *813*, 152196. https://doi.org/10.1016/j.jallcom.2019.152196.
194. Wang, Y.; Li, R.; Niu, P.; Zhang, Z.; Yuan, T.; Yuan, J.; Li, K. Microstructures and properties of equimolar AlCoCrCuFeNi high-entropy alloy additively manufactured by selective laser melting. *Intermetallics* **2020**, *120*, 106746. https://doi.org/10.1016/j.intermet.2020.106746.
195. Wang, M.; Li, R.; Yuan, T.; Chen, C.; Zhou, L.; Chen, H.; Zhang, M.; Xie, S. Microstructures and mechanical property of AlMgScZrMn—A comparison between selective laser melting, spark plasma sintering and cast. *Mater. Sci. Eng. A* **2019**, *756*, 354–364. https://doi.org/10.1016/j.msea.2019.04.060.
196. Sarswat, P.K.; Sarkar, S.; Murali, A.; Huang, W.; Tan, W.; Free, M.L. Additive manufactured new hybrid high entropy alloys derived from the AlCoFeNiSmTiVZr system. *Appl. Surf. Sci.* **2019**, *476*, 242–258. https://doi.org/10.1016/j.apsusc.2018.12.300.
197. Agrawal, P.; Thapliyal, S.; Nene, S.S.; Mishra, R.S.; McWilliams, B.A.; Cho, K.C. Excellent strength-ductility synergy in metastable high entropy alloy by laser powder bed additive manufacturing. *Addit. Manuf.* **2020**, *32*, 101098. https://doi.org/10.1016/j.addma.2020.101098.
198. Zhang, H.; Zhao, Y.; Huang, S.; Zhu, S.; Wang, F.; Li, D. Manufacturing and analysis of high-performance refractory high-entropy alloy via selective laser melting (SLM). *Materials* **2019**, *12*, 720. https://doi.org/10.3390/ma12050720.

199. Zhang, H.; Xu, W.; Xu, Y.; Lu, Z.; Li, D. The thermal-mechanical behavior of WTaMoNb high-entropy alloy via selective laser melting (SLM): Experiment and simulation. *Int. J. Adv. Manuf. Technol.* **2018**, *96*, 461–474. https://doi.org/10.1007/s00170-017-1331-9.
200. Yang, X.; Zhou, Y.; Xi, S.; Chen, Z.; Wei, P.; He, C.; Li, T.; Gao, Y.; Wu, H. Additively manufactured fine grained Ni6Cr4WFe9Ti high entropy alloys with high strength and ductility. *Mater. Sci. Eng. A* **2019**, *767*, 138394. https://doi.org/10.1016/j.msea.2019.138394.
201. Yang, X.; Zhou, Y.; Xi, S.; Chen, Z.; Wei, P.; He, C.; Li, T.; Gao, Y.; Wu, H. Grain-anisotropied high-strength $Ni_6Cr_4WFe_9Ti$ high entropy alloys with outstanding tensile ductility. *Mater. Sci. Eng. A* **2019**, *767*, 138382. https://doi.org/10.1016/j.msea.2019.138382.
202. Chen, P.; Yang, C.; Li, S.; Attallah, M.M.; Yan, M. In-situ alloyed, oxide-dispersion-strengthened CoCrFeMnNi high entropy alloy fabricated via laser powder bed fusion. *Mater. Des.* **2020**, *194*, 108966. https://doi.org/10.1016/j.matdes.2020.108966.
203. Litwa, P.; Hernandez-Nava, E.; Guan, D.; Goodall, R.; Wika, K.K. The additive manufacture processing and machinability of CrMnFeCoNi high entropy alloy. *Mater. Des.* **2021**, *198*, 109380. https://doi.org/10.1016/j.matdes.2020.109380.
204. Zhang, C.; Feng, K.; Kokawa, H.; Han, B.; Li, Z. Cracking mechanism and mechanical properties of selective laser melted CoCrFeMnNi high entropy alloy using different scanning strategies. *Mater. Sci. Eng. A* **2020**, *789*, 139672. https://doi.org/10.1016/j.msea.2020.139672.
205. Kim, Y.K.; Suh, J.Y.; Lee, K.A. Effect of gaseous hydrogen embrittlement on the mechanical properties of additively manufactured CrMnFeCoNi high-entropy alloy strengthened by in-situ formed oxide. *Mater. Sci. Eng. A* **2020**, *796*, 140039. https://doi.org/10.1016/j.msea.2020.140039.
206. Choi, N.; Kulitckii, V.; Kottke, J.; Tas, B.; Choe, J.; Yu, J.H.; Yang, S.; Park, J.H.; Lee, J.S.; Wilde, G.; et al. Analyzing the 'non-equilibrium state' of grain boundaries in additively manufactured high-entropy CoCrFeMnNi alloy using tracer diffusion measurements. *J. Alloys Compd.* **2020**, *844*, 155757. https://doi.org/10.1016/j.jallcom.2020.155757.
207. Su, Y.; Luo, S.; Wang, Z. Microstructure evolution and cracking behaviors of additively manufactured $Al_xCrCuFeNi_2$ high entropy alloys via selective laser melting. *J. Alloys Compd.* **2020**, *842*, 155823. https://doi.org/10.1016/j.jallcom.2020.155823.
208. Peng, Y.; Kong, Y.; Zhang, W.; Zhang, M.; Wang, H. Effect of diffusion barrier and interfacial strengthening on the interface behavior between high entropy alloy and diamond. *J. Alloys Compd.* **2021**, *852*, 157023. https://doi.org/10.1016/j.jallcom.2020.157023.
209. Wang, H.; Zhu, Z.G.; Chen, H.; Wang, A.G.; Liu, J.Q.; Liu, H.W.; Zheng, R.K.; Nai, S.M.L.; Primig, S.; Babu, S.S.; et al. Effect of cyclic rapid thermal loadings on the microstructural evolution of a CrMnFeCoNi high-entropy alloy manufactured by selective laser melting. *Acta Mater.* **2020**, *196*, 609–625. https://doi.org/10.1016/j.actamat.2020.07.006.
210. Sun, Z.; Tan, X.; Wang, C.; Descoins, M.; Mangelinck, D.; Tor, S.B.; Jägle, E.A.; Zaefferer, S.; Raabe, D. Reducing hot tearing by grain boundary segregation engineering in additive manufacturing: Example of an $Al_xCoCrFeNi$ high-entropy alloy. *Acta Mater.* **2021**, *204*, 116505. https://doi.org/10.1016/j.actamat.2020.116505.
211. Ishimoto, T.; Ozasa, R.; Nakano, K.; Weinmann, M.; Schnitter, C.; Stenzel, M.; Matsugaki, A.; Nagase, T.; Matsuzaka, T.; Todai, M.; et al. Development of TiNbTaZrMo bio-high entropy alloy (BioHEA) super-solid solution by selective laser melting, and its improved mechanical property and biocompatibility. *Scr. Mater.* **2021**, *194*, 113658. https://doi.org/10.1016/j.scriptamat.2020.113658.
212. Park, J.M.; Choe, J.; Park, H.K.; Son, S.; Jung, J.; Kim, T.S.; Yu, J.H.; Kim, J.G.; Kim, H.S. Synergetic strengthening of additively manufactured $(CoCrFeMnNi)_{99}C_1$ high-entropy alloy by heterogeneous anisotropic microstructure. *Addit. Manuf.* **2020**, *35*, 101333. https://doi.org/10.1016/j.addma.2020.101333.
213. Lin, D.; Xu, L.; Li, X.; Jing, H.; Qin, G.; Pang, H.; Minami, F. A Si-containing FeCoCrNi high-entropy alloy with high strength and ductility synthesized in situ via selective laser melting. *Addit. Manuf.* **2020**, *35*, 101340. https://doi.org/10.1016/j.addma.2020.101340.
214. Kim, Y.K.; Yang, S.; Lee, K.A. Compressive creep behavior of selective laser melted CoCrFeMnNi high-entropy alloy strengthened by in-situ formation of nano-oxides. *Addit. Manuf.* **2020**, *36*, 101543. https://doi.org/10.1016/j.addma.2020.101543.
215. Jin, M.; Piglione, A.; Dovgyy, B.; Hosseini, E.; Hooper, P.A.; Holdsworth, S.R.; Pham, M.S. Cyclic plasticity and fatigue damage of CrMnFeCoNi high entropy alloy fabricated by laser powder-bed fusion. *Addit. Manuf.* **2020**, *36*, 101584. https://doi.org/10.1016/j.addma.2020.101584.
216. Lin, W.C.; Chang, Y.J.; Hsu, T.H.; Gorsse, S.; Sun, F.; Furuhara, T.; Yeh, A.C. Microstructure and tensile property of a precipitation strengthened high entropy alloy processed by selective laser melting and post heat treatment. *Addit. Manuf.* **2020**, *36*, 101601. https://doi.org/10.1016/j.addma.2020.101601.
217. Peng, H.; Lin, Z.; Li, R.; Niu, P.; Zhang, Z. Corrosion Behavior of an Equiatomic CoCrFeMnNi High-Entropy Alloy- a Comparison Between Selective Laser Melting and Cast. *Front. Mater.* **2020**, *7*, 244. https://doi.org/10.3389/fmats.2020.00244.
218. Vogiatzief, D.; Evirgen, A.; Gein, S.; Molina, V.R.; Weisheit, A.; Pedersen, M. Laser Powder Bed Fusion and Heat Treatment of an $AlCrFe_2Ni_2$ High Entropy Alloy. *Front. Mater.* **2020**, *7*, 248. https://doi.org/10.3389/fmats.2020.00248.
219. Liao, Y.; Zhu, P.; Li, S. Synthesis of AlFeCrNiV high entropy alloy by gas atomization and selective laser melting. *Synthesis (Stuttg)* **2020**, *7*, 11591-11594.
220. Guo, L.; Gu, J.; Gan, B.; Ni, S.; Bi, Z.; Wang, Z.; Song, M. Effects of elemental segregation and scanning strategy on the mechanical properties and hot cracking of a selective laser melted FeCoCrNiMn-(N,Si) high entropy alloy. *J. Alloys Compd.* **2021**, *865*, 158892. https://doi.org/10.1016/j.jallcom.2021.158892.

221. Kim, Y.K.; Yu, J.H.; Kim, H.S.; Lee, K.A. In-situ carbide-reinforced CoCrFeMnNi high-entropy alloy matrix nanocomposites manufactured by selective laser melting: Carbon content effects on microstructure, mechanical properties, and deformation mechanism. *Compos. Part B Eng.* **2021**, *210*, 108638. https://doi.org/10.1016/j.compositesb.2021.108638.
222. Zhao, W.; Han, J.-K.; Kuzminova, Y.O.; Evlashin, S.A.; Zhilyaev, A.P.; Pesin, A.M.; Jang, J.; Liss, K.-D.; Kawasaki, M. Significance of grain refinement on micro-mechanical properties and structures of additively-manufactured CoCrFeNi high-entropy alloy. *Mater. Sci. Eng. A* **2021**, *807*, 140898. https://doi.org/10.1016/j.msea.2021.140898.
223. Gu, Z.; Su, X.; Peng, W.; Guo, W.; Xi, S.; Zhang, X.; Tu, H.; Gao, Y.; Wu, H. An important improvement of strength and ductility on a new type of $CoCr_{2.5}FeNi_2TiW_{0.5}$ high entropy alloys under two different protective gases by selective laser melting. *J. Alloys Compd.* **2021**, *868*, 159088. https://doi.org/10.1016/j.jallcom.2021.159088.
224. Peng, S.; Mooraj, S.; Feng, R.; Liu, L.; Ren, J.; Liu, Y.; Kong, F.; Xiao, Z.; Zhu, C.; Liaw, P.K.; et al. Additive manufacturing of three-dimensional (3D)-architected CoCrFeNiMn high- entropy alloy with great energy absorption. *Scr. Mater.* **2021**, *190*, 46–51. https://doi.org/10.1016/j.scriptamat.2020.08.028.
225. Wang, P.; Huang, P.; Ng, F.L.; Sin, W.J.; Lu, S.; Nai, M.L.S.; Dong, Z.L.; Wei, J. Additively manufactured CoCrFeNiMn high-entropy alloy via pre-alloyed powder. *Mater. Des.* **2019**, *168*, 107576. https://doi.org/10.1016/j.matdes.2018.107576.
226. Kuwabara, K.; Shiratori, H.; Fujieda, T.; Yamanaka, K.; Koizumi, Y.; Chiba, A. Mechanical and corrosion properties of AlCoCrFeNi high-entropy alloy fabricated with selective electron beam melting. *Addit. Manuf.* **2018**, *23*, 264–271. https://doi.org/10.1016/j.addma.2018.06.006.
227. Yang, S.; Liu, Z.; Pi, J. Microstructure and wear behavior of the AlCrFeCoNi high-entropy alloy fabricated by additive manufacturing. *Mater. Lett.* **2020**, *261*, 127004. https://doi.org/10.1016/j.matlet.2019.127004.
228. Fujieda, T.; Chen, M.; Shiratori, H.; Kuwabara, K.; Yamanaka, K.; Koizumi, Y.; Chiba, A.; Watanabe, S. Mechanical and corrosion properties of CoCrFeNiTi-based high-entropy alloy additive manufactured using selective laser melting. *Addit. Manuf.* **2019**, *25*, 412–420. https://doi.org/10.1016/j.addma.2018.10.023.
229. Popov, V. V.; Katz-Demyanetz, A.; Koptyug, A.; Bamberger, M. Selective electron beam melting of $Al_{0.5}CrMoNbTa_{0.5}$ high entropy alloys using elemental powder blend. *Heliyon* **2019**, *5*, e01188. https://doi.org/10.1016/j.heliyon.2019.e01188.
230. Guan, S.; Wan, D.; Solberg, K.; Berto, F.; Welo, T.; Yue, T.M.; Chan, K.C. Additive manufacturing of fine-grained and dislocation-populated CrMnFeCoNi high entropy alloy by laser engineered net shaping. *Mater. Sci. Eng. A* **2019**, *761*, 138056. https://doi.org/10.1016/j.msea.2019.138056.
231. Melia, M.A.; Carroll, J.D.; Whetten, S.R.; Esmaeely, S.N.; Locke, J.; White, E.; Anderson, I.; Chandross, M.; Michael, J.R.; Argibay, N.; et al. Mechanical and Corrosion Properties of Additively Manufactured CoCrFeMnNi High Entropy Alloy. *Addit. Manuf.* **2019**, *29*, 100833. https://doi.org/10.1016/j.addma.2019.100833.
232. Li, H.G.; Lee, T.L.; Zheng, W.; Lu, Y.Z.; Yin, H.B.C.; Yang, J.X.; Huang, Y.J.; Sun, J.F. Characterization of residual stress in laser melting deposited CoCrFeMnNi high entropy alloy by neutron diffraction. *Mater. Lett.* **2020**, *263*, 127247. https://doi.org/10.1016/j.matlet.2019.127247.
233. Gao, X.; Lu, Y. Laser 3D printing of CoCrFeMnNi high-entropy alloy. *Mater. Lett.* **2019**, *236*, 77–80. https://doi.org/10.1016/j.matlet.2018.10.084.
234. Xiang, S.; Li, J.; Luan, H.; Amar, A.; Lu, S.; Li, K.; Zhang, L.; Liu, X.; Le, G.; Wang, X.; et al. Effects of process parameters on microstructures and tensile properties of laser melting deposited CrMnFeCoNi high entropy alloys. *Mater. Sci. Eng. A* **2019**, *743*, 412–417. https://doi.org/10.1016/j.msea.2018.11.110.
235. Xiang, S.; Luan, H.; Wu, J.; Yao, K.F.; Li, J.; Liu, X.; Tian, Y.; Mao, W.; Bai, H.; Le, G.; et al. Microstructures and mechanical properties of CrMnFeCoNi high entropy alloys fabricated using laser metal deposition technique. *J. Alloys Compd.* **2019**, *773*, 387–392. https://doi.org/10.1016/j.jallcom.2018.09.235.
236. Chew, Y.; Bi, G.J.; Zhu, Z.G.; Ng, F.L.; Weng, F.; Liu, S.B.; Nai, S.M.L.; Lee, B.Y. Microstructure and enhanced strength of laser aided additive manufactured CoCrFeNiMn high entropy alloy. *Mater. Sci. Eng. A* **2019**, *744*, 137–144. https://doi.org/10.1016/j.msea.2018.12.005.
237. Qiu, Z.; Yao, C.; Feng, K.; Li, Z.; Chu, P.K. Cryogenic deformation mechanism of CrMnFeCoNi high-entropy alloy fabricated by laser additive manufacturing process. *Int. J. Light. Mater. Manuf.* **2018**, *1*, 33–39. https://doi.org/10.1016/j.ijlmm.2018.02.001.
238. Li, J.; Xiang, S.; Luan, H.; Amar, A.; Liu, X.; Lu, S.; Zeng, Y.; Le, G.; Wang, X.; Qu, F.; et al. Additive manufacturing of high-strength CrMnFeCoNi high-entropy alloys-based composites with WC addition. *J. Mater. Sci. Technol.* **2019**, *35*, 2430–2434. https://doi.org/10.1016/j.jmst.2019.05.062.
239. Amar, A.; Li, J.; Xiang, S.; Liu, X.; Zhou, Y.; Le, G.; Wang, X.; Qu, F.; Ma, S.; Dong, W.; et al. Additive manufacturing of high-strength CrMnFeCoNi-based High Entropy Alloys with TiC addition. *Intermetallics* **2019**, *109*, 162–166. https://doi.org/10.1016/j.intermet.2019.04.005.
240. Guan, S.; Wan, D.; Solberg, K.; Berto, F.; Welo, T.; Yue, T.M.; Chan, K.C. Additively manufactured CrMnFeCoNi/AlCoCrFeNiTi0.5 laminated high-entropy alloy with enhanced strength-plasticity synergy. *Scr. Mater.* **2020**, *183*, 133–138. https://doi.org/10.1016/j.scriptamat.2020.03.032.
241. Wang, Q.; Amar, A.; Jiang, C.; Luan, H.; Zhao, S.; Zhang, H.; Le, G.; Liu, X.; Wang, X.; Yang, X.; et al. CoCrFeNiMo0.2 high entropy alloy by laser melting deposition: Prospective material for low temperature and corrosion resistant applications. *Intermetallics* **2020**, *119*, 106727. https://doi.org/10.1016/j.intermet.2020.106727.
242. Zhou, K.; Li, J.; Wang, L.; Yang, H.; Wang, Z.; Wang, J. Direct laser deposited bulk $CoCrFeNiNb_x$ high entropy alloys. *Intermetallics* **2019**, *114*, 106592. https://doi.org/10.1016/j.intermet.2019.106592.

243. Gwalani, B.; Gangireddy, S.; Shukla, S.; Yannetta, C.J.; Valentin, S.G.; Mishra, R.S.; Banerjee, R. Compositionally graded high entropy alloy with a strong front and ductile back. *Mater. Today Commun.* **2019**, *20*, 100602. https://doi.org/10.1016/j.mtcomm.2019.100602.
244. Nartu, M.S.K.K.Y.; Alam, T.; Dasari, S.; Mantri, S.A.; Gorsse, S.; Siller, H.; Dahotre, N.; Banerjee, R. Enhanced tensile yield strength in laser additively manufactured Al0.3CoCrFeNi high entropy alloy. *Materialia* **2020**, *9*, 100522. https://doi.org/10.1016/j.mtla.2019.100522.
245. Mohanty, A.; Sampreeth, J.K.; Bembalge, O.; Hascoet, J.Y.; Marya, S.; Immanuel, R.J.; Panigrahi, S.K. High temperature oxidation study of direct laser deposited $Al_xCoCrFeNi$ (X = 0.3, 0.7) high entropy alloys. *Surf. Coat. Technol.* **2019**, *380*, 125028. https://doi.org/10.1016/j.surfcoat.2019.125028.
246. Vikram, R.J.; Murty, B.S.; Fabijanic, D.; Suwas, S. Insights into micro-mechanical response and texture of the additively manufactured eutectic high entropy alloy $AlCoCrFeNi_{2.1}$. *J. Alloys Compd.* **2020**, *827*, 154034. https://doi.org/10.1016/j.jallcom.2020.154034.
247. Gwalani, B.; Soni, V.; Waseem, O.A.; Mantri, S.A.; Banerjee, R. Laser additive manufacturing of compositionally graded $AlCrFeMoV_x$ (x = 0 to 1) high-entropy alloy system. *Opt. Laser Technol.* **2019**, *113*, 330–337. https://doi.org/10.1016/j.optlastec.2019.01.009.
248. Guan, S.; Solberg, K.; Wan, D.; Berto, F.; Welo, T.; Yue, T.M.; Chan, K.C. Formation of fully equiaxed grain microstructure in additively manufactured $AlCoCrFeNiTi_{0.5}$ high entropy alloy. *Mater. Des.* **2019**, *184*, 108202. https://doi.org/10.1016/j.matdes.2019.108202.
249. Malatji, N.; Popoola, A.P.I.; Lengopeng, T.; Pityana, S. Tribological and corrosion properties of laser additive manufactured AlCrFeNiCu high entropy alloy. *Mater. Today Proc.* **2020**, *28*, 944–948. https://doi.org/10.1016/j.matpr.2019.12.330.
250. Dada, M.; Patricia, P.; Mathe, N.; Pityana, S.; Adeosun, S.; Lengopeng, T. Fabrication and Hardness Behaviour of High Entropy Alloys. In Proceedings of the TMS 2020 149th Annual Meeting & Exhibition Supplemental Proceedings, San Diego, USA, February 23-27, 2020; pp. 1581–1591.
251. Dada, M.; Popoola, P.; Mathe, N.; Pityana, S.; Adeosun, S. Effect of laser parameters on the properties of high entropy alloys: A preliminary study. *Mater. Today Proc.* **2020**, *38*, 756–761. https://doi.org/10.1016/j.matpr.2020.04.198.
252. Moorehead, M.; Bertsch, K.; Niezgoda, M.; Parkin, C.; Elbakhshwan, M.; Sridharan, K.; Zhang, C.; Thoma, D.; Couet, A. High-throughput synthesis of Mo-Nb-Ta-W high-entropy alloys via additive manufacturing. *Mater. Des.* **2020**, *187*, 108358. https://doi.org/10.1016/j.matdes.2019.108358.
253. Kunce, I.; Polanski, M.; Bystrzycki, J. Microstructure and hydrogen storage properties of a TiZrNbMoV high entropy alloy synthesized using Laser Engineered Net Shaping (LENS). *Int. J. Hydrogen Energy* **2014**, *39*, 9904–9910. https://doi.org/10.1016/j.ijhydene.2014.02.067.
254. Dobbelstein, H.; Gurevich, E.L.; George, E.P.; Ostendorf, A.; Laplanche, G. Laser metal deposition of a refractory TiZrNbHfTa high-entropy alloy. *Addit. Manuf.* **2018**, *24*, 386–390. https://doi.org/10.1016/j.addma.2018.10.008.
255. Pegues, J.W.; Melia, M.A.; Puckett, R.; Whetten, S.R.; Argibay, N.; Kustas, A.B. Exploring additive manufacturing as a high-throughput screening tool for multiphase high entropy alloys. *Addit. Manuf.* **2021**, *37*, 101598. https://doi.org/10.1016/j.addma.2020.101598.
256. Li, H.; Huang, Y.; Jiang, S.; Lu, Y.; Gao, X.; Lu, X.; Ning, Z.; Sun, J. Columnar to equiaxed transition in additively manufactured CoCrFeMnNi high entropy alloy. *Mater. Des.* **2021**, *197*, 109262. https://doi.org/10.1016/j.matdes.2020.109262.
257. Tong, Z.; Liu, H.; Jiao, J.; Zhou, W.; Yang, Y.; Ren, X. Improving the strength and ductility of laser directed energy deposited CrMnFeCoNi high-entropy alloy by laser shock peening. *Addit. Manuf.* **2020**, *35*, 101417. https://doi.org/10.1016/j.addma.2020.101417.
258. Shen, Q.; Kong, X.; Chen, X.; Yao, X.; Deev, V.B.; Prusov, E.S. Powder plasma arc additive manufactured $CoCrFeNi(SiC)_x$ high-entropy alloys: Microstructure and mechanical properties. *Mater. Lett.* **2021**, *282*, 128736. https://doi.org/10.1016/j.matlet.2020.128736.
259. Cai, Y.; Zhu, L.; Cui, Y.; Han, J. Manufacturing of FeCoCrNi + FeCoCrNiAl laminated high-entropy alloy by laser melting deposition (LMD). *Mater. Lett.* **2021**, *289*, 129445. https://doi.org/10.1016/j.matlet.2021.129445.
260. Zhang, H.; Zhao, Y.; Cai, J.; Ji, S.; Geng, J.; Sun, X.; Li, D. High-strength $NbMoTa_x$ refractory high-entropy alloy with low stacking fault energy eutectic phase via laser additive manufacturing. *Mater. Des.* **2021**, *201*, 109462. https://doi.org/10.1016/j.matdes.2021.109462.
261. Peng, H.; Xie, S.; Niu, P.; Zhang, Z.; Yuan, T.; Ren, Z.; Wang, X.; Zhao, Y.; Li, R. Additive manufacturing of $Al_{0.3}CoCrFeNi$ high-entropy alloy by powder feeding laser melting deposition. *J. Alloys Compd.* **2021**, *863*, 158286. https://doi.org/10.1016/j.jallcom.2020.158286.
262. Kuzminova, Y.O.; Firsov, D.G.; Dagesyan, S.A.; Konev, S.D.; Sergeev, S.N.; Zhilyaev, A.P.; Kawasaki, M.; Akhatov, I.S.; Evlashin, S.A. Fatigue behavior of additive manufactured CrFeCoNi medium-entropy alloy. *J. Alloys Compd.* **2021**, *863*, 158609. https://doi.org/10.1016/j.jallcom.2021.158609.
263. Malatji, N.; Lengopeng, T.; Pityana, S.; Popoola, A.P.I. Effect of heat treatment on the microstructure, microhardness, and wear characteristics of AlCrFeCuNi high-entropy alloy. *Int. J. Adv. Manuf. Technol.* **2020**, *111*, 2021–2029. https://doi.org/10.1007/s00170-020-06220-x.

264. Dong, B.; Wang, Z.; Pan, Z.; Muránsky, O.; Shen, C.; Reid, M.; Wu, B.; Chen, X.; Li, H. On the development of pseudo-eutectic $AlCoCrFeNi_{2.1}$ high entropy alloy using Powder-bed Arc Additive Manufacturing (PAAM) process. *Mater. Sci. Eng. A* **2021**, *802*, 140639. https://doi.org/10.1016/j.msea.2020.140639.
265. Zhou, K.; Wang, Z.; He, F.; Liu, S.; Li, J.; Kai, J. jung; Wang, J. A precipitation-strengthened high-entropy alloy for additive manufacturing. *Addit. Manuf.* **2020**, *35*, 101410. https://doi.org/10.1016/j.addma.2020.101410.
266. Zheng, M.; Li, C.; Zhang, X.; Ye, Z.; Yang, X.; Gu, J. The influence of columnar to equiaxed transition on deformation behavior of FeCoCrNiMn high entropy alloy fabricated by laser-based directed energy deposition. *Addit. Manuf.* **2020**, *37*, 101660. https://doi.org/10.1016/j.addma.2020.101660.
267. Luo, S.; Wang, Z.; Zeng, X. Study on the formability, microstructures and mechanical properties of AlCrCuFeNi high-entropy alloys prepared by selective laser melting. In Proceedings of the Solid Freeform Fabrication 2019: Proceedings of the 30th Annual International Solid Freeform Fabrication Symposium—An Additive Manufacturing Conference, Wuhan, China, 12–14 August 2019; pp. 625–635.
268. Jiang, F.; Zhao, C.; Liang, D.; Zhu, W.; Zhang, Y.; Pan, S.; Ren, F. In-situ formed heterogeneous grain structure in spark-plasma-sintered CoCrFeMnNi high-entropy alloy overcomes the strength-ductility trade-off. *Mater. Sci. Eng. A* **2020**, *771*, 138625. https://doi.org/10.1016/j.msea.2019.138625.
269. Rogal, Ł.; Kalita, D.; Tarasek, A.; Bobrowski, P.; Czerwinski, F. Effect of SiC nano-particles on microstructure and mechanical properties of the CoCrFeMnNi high entropy alloy. *J. Alloys Compd.* **2017**, *708*, 344–352. https://doi.org/10.1016/j.jallcom.2017.02.274.
270. Yim, D.; Sathiyamoorthi, P.; Hong, S.J.; Kim, H.S. Fabrication and mechanical properties of TiC reinforced CoCrFeMnNi high-entropy alloy composite by water atomization and spark plasma sintering. *J. Alloys Compd.* **2019**, *781*, 389–396. https://doi.org/10.1016/j.jallcom.2018.12.119.
271. Rogal, Ł.; Kalita, D.; Litynska-Dobrzynska, L. CoCrFeMnNi high entropy alloy matrix nanocomposite with addition of Al_2O_3. *Intermetallics* **2017**, *86*, 104–109. https://doi.org/10.1016/j.intermet.2017.03.019.
272. Li, X.; Feng, Y.; Liu, B.; Yi, D.; Yang, X.; Zhang, W.; Chen, G.; Liu, Y.; Bai, P. Influence of NbC particles on microstructure and mechanical properties of AlCoCrFeNi high-entropy alloy coatings prepared by laser cladding. *J. Alloys Compd.* **2019**, *788*, 485–494. https://doi.org/10.1016/j.jallcom.2019.02.223.
273. Chen, S.; Chen, X.; Wang, L.; Liang, J.; Liu, C. Laser cladding FeCrCoNiTiAl high entropy alloy coatings reinforced with self-generated TiC particles. *J. Laser Appl.* **2017**, *29*, 012004. https://doi.org/10.2351/1.4966052.
274. Fan, Q.C.; Li, B.S.; Zhang, Y. The microstructure and properties of (FeCrNiCo)AlxCuy high-entropy alloys and their TiC-reinforced composites. *Mater. Sci. Eng. A* **2014**, *598*, 244–250. https://doi.org/10.1016/j.msea.2014.01.044.
275. Jiang, L.; Jiang, H.; Lu, Y.; Wang, T.; Cao, Z.; Li, T. Mechanical properties improvement of $AlCrFeNi_2Ti_{0.5}$ high entropy alloy through annealing design and its relationship with its particle-reinforced microstructures. *J. Mater. Sci. Technol.* **2015**, *31*, 397–402. https://doi.org/10.1016/j.jmst.2014.09.011.
276. Guo, L.; Ou, X.; Ni, S.; Liu, Y.; Song, M. Effects of carbon on the microstructures and mechanical properties of FeCoCrNiMn high entropy alloys. *Mater. Sci. Eng. A* **2019**, *746*, 356–362. https://doi.org/10.1016/j.msea.2019.01.050.
277. Zhu, S.; Yu, Y.; Zhang, B.; Zhang, Z.; Yan, X.; Wang, Z. Microstructure and wear behaviour of in-situ TiN-Al_2O_3 reinforced CoCrFeNiMn high-entropy alloys composite coatings fabricated by plasma cladding. *Mater. Lett.* **2020**, *272*, 127870. https://doi.org/10.1016/j.matlet.2020.127870.
278. Lim, K.R.; Kwon, H.J.; Kang, J.H.; Won, J.W.; Na, Y.S. A novel ultra-high-strength duplex Al–Co–Cr–Fe–Ni high-entropy alloy reinforced with body-centered-cubic ordered-phase particles. *Mater. Sci. Eng. A* **2020**, *771*, 138638. https://doi.org/10.1016/j.msea.2019.138638.
279. Fu, A.; Guo, W.; Liu, B.; Cao, Y.; Xu, L.; Fang, Q.; Yang, H.; Liu, Y. A particle reinforced NbTaTiV refractory high entropy alloy based composite with attractive mechanical properties. *J. Alloys Compd.* **2020**, *815*, 152466. https://doi.org/10.1016/j.jallcom.2019.152466.
280. Wang, L.; Wang, L.; Tang, Y.C.; Luo, L.; Luo, L.S.; Su, Y.Q.; Guo, J.J.; Fu, H.Z. Microstructure and mechanical properties of $CoCrFeNiW_x$ high entropy alloys reinforced by μ phase particles. *J. Alloys Compd.* **2020**, *843*, 155997. https://doi.org/10.1016/j.jallcom.2020.155997.
281. Jinhong, P.; Ye, P.; Hui, Z.; Lu, Z. Microstructure and properties of AlCrFeCuNi x ($0.6 \le x \le 1.4$) high-entropy alloys. *Mater. Sci. Eng. A* **2012**, *543*, 228–233. https://doi.org/10.1016/j.msea.2011.11.063.
282. He, J.Y.; Liu, W.H.; Wang, H.; Wu, Y.; Liu, X.J.; Nieh, T.G.; Lu, Z.P. Effects of Al addition on structural evolution and tensile properties of the FeCoNiCrMn high-entropy alloy system. *Acta Mater.* **2014**, *62*, 105–113. https://doi.org/10.1016/j.actamat.2013.09.037.
283. Senkov, O.N.; Wilks, G.B.; Miracle, D.B.; Chuang, C.P.; Liaw, P.K. Refractory high-entropy alloys. *Intermetallics* **2010**, *18*, 1758–1765. https://doi.org/10.1016/j.intermet.2010.05.014.
284. Senkov, O.N.; Wilks, G.B.; Scott, J.M.; Miracle, D.B. Mechanical properties of $Nb_{25}Mo_{25}Ta_{25}W_{25}$ and $V_{20}Nb_{20}Mo_{20}Ta_{20}W_{20}$ refractory high entropy alloys. *Intermetallics* **2011**, *19*, 698–706. https://doi.org/10.1016/j.intermet.2011.01.004.
285. Chu, S.; Majumdar, A. Opportunities and challenges for a sustainable energy future. *Nature* **2012**, *488*, 294–303.
286. Yvon, P.; Carré, F. Structural materials challenges for advanced reactor systems. *J. Nucl. Mater.* **2009**, *385*, 217–222. https://doi.org/10.1016/j.jnucmat.2008.11.026.
287. Allen, T.; Busby, J.; Meyer, M.; Petti, D. Materials challenges for nuclear systems. *Mater. Today* **2010**, *13*, 14–23.

288. Murty, K.L.; Charit, I. Structural materials for Gen-IV nuclear reactors: Challenges and opportunities. *J. Nucl. Mater.* **2008**, *383*, 189–195. https://doi.org/10.1016/j.jnucmat.2008.08.044.
289. Zinkle, S.J.; Boutard, J.L.; Hoelzer, D.T.; Kimura, A.; Lindau, R.; Odette, G.R.; Rieth, M.; Tan, L.; Tanigawa, H. Development of next generation tempered and ODS reduced activation ferritic/martensitic steels for fusion energy applications. *Nucl. Fusion* **2017**, *57*, 092005. https://doi.org/10.1088/1741-4326/57/9/092005.
290. Zinkle, S.J.; Busby, J.T. Structural materials for fission & fusion energy. *Mater. Today* **2009**, *12*, 12–19. https://doi.org/10.1016/S1369-7021(09)70294-9.
291. Li, C. *Characterization of Radiation Effects and* Ab Initio *Modeling of Defects in a High Entropy Alloy for Nuclear Power Application*; The University of Tennessee: Knoxville, TN, USA, 2018.
292. Hoffman, A.K. Development and characterization of nanostructured steels and high entropy alloys for nuclear applications. *J. Mater. Res.* **2019**, *33*, 3077–3091.
293. King, D.J.M. *Investigation of High-Entropy Alloys for Use in Advanced Nuclear Applications*; University of Technology Sydney: Sydney, Australia, 2016.
294. Yeh, J.W.; Lin, S.J. Breakthrough applications of high-entropy materials. *J. Mater. Res.* **2018**, *33*, 3129–3137. https://doi.org/10.1557/jmr.2018.283.
295. Xia, S. qin; Wang, Z.; Yang, T. fei; Zhang, Y. Irradiation Behavior in High Entropy Alloys. *J. Iron Steel Res. Int.* **2015**, *22*, 879–884.
296. Barron, P.J.; Carruthers, A.W.; Fellowes, J.W.; Jones, N.G.; Dawson, H.; Pickering, E.J. Towards V-based high-entropy alloys for nuclear fusion applications. *Scr. Mater.* **2020**, *176*, 12–16. https://doi.org/10.1016/j.scriptamat.2019.09.028.
297. Xiang, C.; Fu, H.M.; Zhang, Z.M.; Han, E.H.; Zhang, H.F.; Wang, J.Q.; Hu, G.D. Effect of Cr content on microstructure and properties of $Mo_{0.5}VNbTiCr_x$ high-entropy alloys. *J. Alloys Compd.* **2020**, *818*, 153352. https://doi.org/10.1016/j.jallcom.2019.153352.
298. Yang, T.; Guo, W.; Poplawsky, J.D.; Li, D.; Wang, L.; Li, Y.; Hu, W.; Crespillo, M.L.; Yan, Z.; Zhang, Y.; et al. Structural damage and phase stability of $Al_{0.3}$CoCrFeNi high entropy alloy under high temperature ion irradiation. *Acta Mater.* **2020**, *188*, 1–15. https://doi.org/10.1016/j.actamat.2020.01.060.
299. Zhang, W.; Wang, M.; Wang, L.; Liu, C.H.; Chang, H.; Yang, J.J.; Liao, J.L.; Yang, Y.Y.; Liu, N. Interface stability, mechanical and corrosion properties of AlCrMoNbZr/(AlCrMoNbZr)N high-entropy alloy multilayer coatings under helium ion irradiation. *Appl. Surf. Sci.* **2019**, *485*, 108–118. https://doi.org/10.1016/j.apsusc.2019.04.192.
300. Xiang, C.; Han, E.H.; Zhang, Z.M.; Fu, H.M.; Wang, J.Q.; Zhang, H.F.; Hu, G.D. Design of single-phase high-entropy alloys composed of low thermal neutron absorption cross-section elements for nuclear power plant application. *Intermetallics* **2019**, *104*, 143–153. https://doi.org/10.1016/j.intermet.2018.11.001.
301. Jawaharram, G.S.; Barr, C.M.; Monterrosa, A.M.; Hattar, K.; Averback, R.S.; Dillon, S.J. Irradiation induced creep in nanocrystalline high entropy alloys. *Acta Mater.* **2020**, *182*, 68–76. https://doi.org/10.1016/j.actamat.2019.10.022.
302. Lu, C.; Yang, T.; Jin, K.; Gao, N.; Xiu, P.; Zhang, Y.; Gao, F.; Bei, H.; Weber, W.J.; Sun, K.; et al. Radiation-induced segregation on defect clusters in single-phase concentrated solid-solution alloys. *Acta Mater.* **2017**, *127*, 98–107. https://doi.org/10.1016/j.actamat.2017.01.019.
303. Barr, C.M.; Nathaniel, J.E.; Unocic, K.A.; Liu, J.; Zhang, Y.; Wang, Y.; Taheri, M.L. Exploring radiation induced segregation mechanisms at grain boundaries in equiatomic CoCrFeNiMn high entropy alloy under heavy ion irradiation. *Scr. Mater.* **2018**, *156*, 80–84. https://doi.org/10.1016/j.scriptamat.2018.06.041.
304. Lu, C.; Niu, L.; Chen, N.; Jin, K.; Yang, T.; Xiu, P.; Zhang, Y.; Gao, F.; Bei, H.; Shi, S.; et al. Enhancing radiation tolerance by controlling defect mobility and migration pathways in multicomponent single-phase alloys. *Nat. Commun.* **2016**, *7*, 13564. https://doi.org/10.1038/ncomms13564.
305. Tong, Y.; Velisa, G.; Zhao, S.; Guo, W.; Yang, T.; Jin, K.; Lu, C.; Bei, H.; Ko, J.Y.P.; Pagan, D.C.; et al. Evolution of local lattice distortion under irradiation in medium- and high-entropy alloys. *Materialia* **2018**, *2*, 73–81. https://doi.org/10.1016/j.mtla.2018.06.008.
306. Jin, K.; Lu, C.; Wang, L.M.; Qu, J.; Weber, W.J.; Zhang, Y.; Bei, H. Effects of compositional complexity on the ion-irradiation induced swelling and hardening in Ni-containing equiatomic alloys. *Scr. Mater.* **2016**, *119*, 65–70. https://doi.org/10.1016/j.scriptamat.2016.03.030.
307. Chen, W.Y.; Liu, X.; Chen, Y.; Yeh, J.W.; Tseng, K.K.; Natesan, K. Irradiation effects in high entropy alloys and 316H stainless steel at 300 °C. *J. Nucl. Mater.* **2018**, *510*, 421–430. https://doi.org/10.1016/j.jnucmat.2018.08.031.
308. Wang, Y.; Zhang, K.; Feng, Y.; Li, Y.; Tang, W.; Wei, B. Evaluation of radiation response in CoCrFeCuNi high-entropy alloys. *Entropy* **2018**, *20*, 835. https://doi.org/10.3390/e20110835.
309. He, M.R.; Wang, S.; Shi, S.; Jin, K.; Bei, H.; Yasuda, K.; Matsumura, S.; Higashida, K.; Robertson, I.M. Mechanisms of radiation-induced segregation in CrFeCoNi-based single-phase concentrated solid solution alloys. *Acta Mater.* **2017**, *126*, 182–193. https://doi.org/10.1016/j.actamat.2016.12.046.
310. Yang, T. ni; Lu, C.; Velisa, G.; Jin, K.; Xiu, P.; Zhang, Y.; Bei, H.; Wang, L. Influence of irradiation temperature on void swelling in NiCoFeCrMn and NiCoFeCrPd. *Scr. Mater.* **2019**, *158*, 57–61. https://doi.org/10.1016/j.scriptamat.2018.08.021.
311. Yang, L.; Ge, H.; Zhang, J.; Xiong, T.; Jin, Q.; Zhou, Y.; Shao, X.; Zhang, B.; Zhu, Z.; Zheng, S.; et al. High He-ion irradiation resistance of CrMnFeCoNi high-entropy alloy revealed by comparison study with Ni and 304SS. *J. Mater. Sci. Technol.* **2019**, *35*, 300–305. https://doi.org/10.1016/j.jmst.2018.09.050.

312. Hashimoto, N.; Ono, Y. Mobility of point defects in CoCrFeNi-base high entropy alloys. *Intermetallics* **2021**, *133*, 107182. https://doi.org/10.1016/j.intermet.2021.107182.
313. Zhang, Y.; Tunes, M.A.; Crespillo, M.L.; Zhang, F.; Boldman, W.L.; Rack, P.D.; Jiang, L.; Xu, C.; Greaves, G.; Donnelly, S.E.; et al. Thermal stability and irradiation response of nanocrystalline CoCrCuFeNi high-entropy alloy. *Nanotechnology* **2019**, *30*, 294004. https://doi.org/10.1088/1361-6528/AB1605.
314. Yang, T. ni; Lu, C.; Jin, K.; Crespillo, M.L.; Zhang, Y.; Bei, H.; Wang, L. The effect of injected interstitials on void formation in self-ion irradiated nickel containing concentrated solid solution alloys. *J. Nucl. Mater.* **2017**, *488*, 328–337. https://doi.org/10.1016/j.jnucmat.2017.02.026.
315. Abhaya, S.; Rajaraman, R.; Kalavathi, S.; David, C.; Panigrahi, B.K.; Amarendra, G. Effect of dose and post irradiation annealing in Ni implanted high entropy alloy FeCrCoNi using slow positron beam. *J. Alloys Compd.* **2016**, *669*, 117–122. https://doi.org/10.1016/j.jallcom.2016.01.242.
316. Sellami, N.; Debelle, A.; Ullah, M.W.; Christen, H.M.; Keum, J.K.; Bei, H.; Xue, H.; Weber, W.J.; Zhang, Y. Effect of electronic energy dissipation on strain relaxation in irradiated concentrated solid solution alloys. *Curr. Opin. Solid State Mater. Sci.* **2019**, *23*, 107–115. https://doi.org/10.1016/j.cossms.2019.02.002.
317. Chen, D.; Tong, Y.; Li, H.; Wang, J.; Zhao, Y.L.; Hu, A.; Kai, J.J. Helium accumulation and bubble formation in FeCoNiCr alloy under high fluence He^+ implantation. *J. Nucl. Mater.* **2018**, *501*, 208–216. https://doi.org/10.1016/j.jnucmat.2018.01.041.
318. Kombaiah, B.; Jin, K.; Bei, H.; Edmondson, P.D.; Zhang, Y. Phase stability of single phase $Al_{0.12}$CrNiFeCo high entropy alloy upon irradiation. *Mater. Des.* **2018**, *160*, 1208–1216. https://doi.org/10.1016/j.matdes.2018.11.006.
319. Lu, C.; Yang, T.; Jin, K.; Velisa, G.; Xiu, P.; Song, M.; Peng, Q.; Gao, F.; Zhang, Y.; Bei, H.; et al. Enhanced void swelling in NiCoFeCrPd high-entropy alloy by indentation-induced dislocations. *Mater. Res. Lett.* **2018**, *6*, 584–591. https://doi.org/10.1080/21663831.2018.1504136.
320. Tunes, M.A.; Edmondson, P.D.; Vishnyakov, V.M.; Donnelly, S.E. Displacement damage and self-healing in high-entropy alloys: A TEM with in situ ion irradiation study. *Fusion Mater. Res. Oak Ridge Natl. Lab. Fisc. Year 2017* **2017**, *1*, 62–64. https://doi.org/10.2172/1427637.
321. AlTabbaa, O.; Ankrah, S. University of Huddersfield Repository. *Technol. Forecast. Soc. Chang.* **2016**, *104*, 1–15.
322. Fan, Z.; Zhong, W.; Jin, K.; Bei, H.; Osetsky, Y.N.; Zhang, Y. Diffusion-mediated chemical concentration variation and void evolution in ion-irradiated NiCoFeCr high-entropy alloy. *J. Mater. Res.* **2021**, *36*, 298–310. https://doi.org/10.1557/s43578-020-00071-8.
323. Lyu, P.; Peng, T.; Miao, Y.; Liu, Z.; Gao, Q.; Zhang, C.; Jin, Y.; Qingfeng Guan, J.C. Microstructure and properties of CoCrFeNiMo$_{0.2}$ high-entropy alloy enhanced by high-current pulsed electron beam. *Surf. Coat. Technol.* **2021**, *410*, 126911.
324. Xu, Q.; Zhu, T.; Zhong, Z.H.; Cao, X.Z.; Tsuchida, H. Investigation of irradiation resistance characteristics of precipitation strengthened high-entropy alloy $(CoCrFeNi)_{95}Ti_1Nb_1Al_3$ using slow positron beam. *J. Alloys Compd.* **2021**, *888*, 161518. https://doi.org/10.1016/j.jallcom.2021.161518.
325. Cao, P.P.; Wang, H.; He, J.Y.; Xuc, C.; Jiang, S.H.; Du, J.L.; Cao, X.Z.; Fu, E.G.; Lu, Z.P. Effects of nanosized precipitates on irradiation behavior of CoCrFeNi high entropy alloys. *J. Alloys Compd.* **2021**, *859*, 158291.
326. Tolstolutskaya, G.D.; Rostova, G.Y.; Voyevodin, V.N.; Velikodnyi, A.N.; Tikhonovsky, M.A.; Tolmachova, G.N.; Kalchenko, A.S.; Vasilenko, R.L.; Kopanets, I.E. Section 2 thermal and fast reactor materials hardening of Cr-Fe-Ni-Mn high-entropy alloys caused by the irradiation with argon ions. *Probl. At. Sci. Technol.* **2017**, *5*, 40–47. https://doi.org/123456789/136159.
327. Kumar, N.A.P.K.; Li, C.; Leonard, K.J.; Bei, H.; Zinkle, S.J. Microstructural stability and mechanical behavior of FeNiMnCr high entropy alloy under ion irradiation. *Acta Mater.* **2016**, *113*, 230–244. https://doi.org/10.1016/j.actamat.2016.05.007.
328. Li, C.; Hu, X.; Yang, T.; Kumar, N.K.; Wirth, B.D.; Zinkle, S.J. Neutron irradiation response of a Co-free high entropy alloy. *J. Nucl. Mater.* **2019**, *527*, 151838. https://doi.org/10.1016/j.jnucmat.2019.151838.
329. Voyevodin, V.N.; Karpov, S.A.; Tolstolutskaya, G.D.; Tikhonovsky, M.A.; Velikodnyi, A.N.; Kopanets, I.E.; Tolmachova, G.N.; Kalchenko, A.S.; Vasilenko, R.L.; Kolodiy, I. V. Effect of irradiation on microstructure and hardening of Cr–Fe–Ni–Mn high-entropy alloy and its strengthened version. *Philos. Mag.* **2020**, *100*, 822–836. https://doi.org/10.1080/14786435.2019.1704091.
330. Dias, M.; Antão, F.; Catarino, N.; Galatanu, A.; Galatanu, M.; Ferreira, P.; Correia, J.B.; da Silva, R.C.; Gonçalves, A.P.; Alves, E. Sintering and irradiation of copper-based high entropy alloys for nuclear fusion. *Fusion Eng. Des.* **2020**, *146*, 1824–1828. https://doi.org/10.1016/j.fusengdes.2019.03.044.
331. Gromov, V.; Ivanov, Y.; Konovalov, S.; Osintsev, K.; Semin, A.; Rubannikova, Y. Modification of high-entropy alloy AlCoCrFeNi by electron beam treatment. *J. Mater. Sci. Technol.* **2021**, *13*, 787–797. https://doi.org/10.1016/j.jmrt.2021.05.012.
332. Yang, T.; Xia, S.; Guo, W.; Hu, R.; Poplawsky, J.D.; Sha, G.; Fang, Y.; Yan, Z.; Wang, C.; Li, C.; et al. Effects of temperature on the irradiation responses of Al0.1CoCrFeNi high entropy alloy. *Scr. Mater.* **2018**, *144*, 31–35. https://doi.org/10.1016/j.scriptamat.2017.09.025.
333. Zhou, J.; Islam, M.I.; Guo, S.; Zhang, Y.; Lu, F. Radiation-induced grain growth of nanocrystalline alxcocrfeni high-entropy alloys. *J. Phys. Chem. C* **2021**, *125*, 3509–3516. https://doi.org/10.1021/acs.jpcc.0c09061.
334. Zhou, J. *Radiation Effects in Apatite and High Entropy Alloy under Energetic Ions and Electrons*; Louisiana State University and Agricultural and Mechanical College: Baton Rouge, LA, USA, 2020.
335. Zhou, J.; Kirk, M.; Baldo, P.; Guo, S.; Lu, F. Phase stability of novel HfNbTaTiVZr refractory high entropy alloy under ion irradiation. *Mater. Lett.* **2021**, *305*, 130789. https://doi.org/10.1016/j.matlet.2021.130789.

336. Moschetti, M.; Xu, A.; Schuh, B.; Hohenwarter, A.; Couzinié, J.P.; Kruzic, J.J.; Bhattacharyya, D.; Gludovatz, B. On the Room-Temperature Mechanical Properties of an Ion-Irradiated TiZrNbHfTa Refractory High Entropy Alloy. *JOM* **2020**, *72*, 130–138. https://doi.org/10.1007/s11837-019-03861-6.
337. Sadeghilaridjani, M.; Ayyagari, A.; Muskeri, S.; Hasannaeimi, V.; Salloom, R.; Chen, W.Y.; Mukherjee, S. Ion irradiation response and mechanical behavior of reduced activity high entropy alloy. *J. Nucl. Mater.* **2020**, *529*, 151955. https://doi.org/10.1016/j.jnucmat.2019.151955.
338. Li, D.; Jia, N.; Huang, H.; Chen, S.; Dou, Y.; He, X.; Yang, W.; Xue, Y.; Hua, Z.; Zhang, F.; et al. Helium ion irradiation enhanced precipitation and the impact on cavity formation in a HfNbZrTi refractory high entropy alloy. *J. Nucl. Mater.* **2021**, *552*, 153023. https://doi.org/10.1016/j.jnucmat.2021.153023.
339. Kareer, A.; Waite, J.C.; Li, B.; Couet, A.; Armstrong, D.E.J.; Wilkinson, A.J. Short communication: 'Low activation, refractory, high entropy alloys for nuclear applications.' *J. Nucl. Mater.* **2019**, *526*, 151744. https://doi.org/10.1016/j.jnucmat.2019.151744.
340. Wang, Y.; Zhang, K.; Feng, Y.; Li, Y.; Tang, W.; Zhang, Y.; Wei, B.; Hu, Z. Excellent irradiation tolerance and mechanical behaviors in high-entropy metallic glasses. *J. Nucl. Mater.* **2019**, *527*, 151785. https://doi.org/10.1016/j.jnucmat.2019.151785.
341. El-Atwani, O.; Li, N.; Li, M.; Devaraj, A.; Baldwin, J.K.S.; Schneider, M.M.; Sobieraj, D.; Wróbel, J.S.; Nguyen-Manh, D.; Maloy, S.A.; et al. Outstanding radiation resistance of tungsten-based high-entropy alloys. *Sci. Adv.* **2019**, *5*, eaav2002. https://doi.org/10.1126/sciadv.aav2002.
342. Komarov, F.F.; Konstantinov, S. V.; Pogrebnyak, A.D. Effect of high-fluence ion irradiation on the structure and mechanical properties of coatings based on nanostructured nitrides of high-entropy alloys (Ti, Hf, Zr, V, Nb). *Dokl. Natsional'noj Akad. Nauk Belarusi* **2015**, *48*, 24–30. https://doi.org/10.29235/1561-8323-2019-63-6-761-768.
343. Gandy, A.S.; Jim, B.; Coe, G.; Patel, D.; Hardwick, L.; Akhmadaliev, S.; Reeves-McLaren, N.; Goodall, R. High temperature and ion implantation-induced phase transformations in novel reduced activation si-fe-v-cr (-mo) high entropy alloys. *Front. Mater.* **2019**, *6*, 146. https://doi.org/10.3389/fmats.2019.00146.
344. Patel, D.; Richardson, M.D.; Jim, B.; Akhmadaliev, S.; Goodall, R.; Gandy, A.S. Radiation damage tolerance of a novel metastable refractory high entropy alloy $V_{2.5}Cr_{1.2}WMoCo_{0.04}$. *J. Nucl. Mater.* **2020**, *531*, 152005. https://doi.org/10.1016/j.jnucmat.2020.152005.
345. Zhang, Z.; Han, E.H.; Xiang, C. Irradiation behaviors of two novel single-phase bcc-structure high-entropy alloys for accident-tolerant fuel cladding. *J. Mater. Sci. Technol.* **2021**, *84*, 230–238. https://doi.org/10.1016/j.jmst.2020.12.058.
346. Zhang, Z.; Han, E.H.; Xiang, C. Effect of helium ion irradiation on short-time corrosion behavior of two novel high-entropy alloys in simulated PWR primary water. *Corros. Sci.* **2021**, *191*, 109742. https://doi.org/10.1016/j.corsci.2021.109742.
347. El-Atwani, O.; Alvarado, A.; Unal, K.; Fensin, S.; Hinks, J.A.; Greaves, G.; Baldwin, J.K.S.; Maloy, S.A.; Martinez, E. Helium implantation damage resistance in nanocrystalline W-Ta-V-Cr high entropy alloys. *Mater. Today Energy* **2021**, *19*, 100599. https://doi.org/10.1016/j.mtener.2020.100599.
348. Garner, F.A.; Toloczko, M.B.; Sencer, B.H. Comparison of swelling and irradiation creep behavior of fcc-austenitic and bcc-ferritic/martensitic alloys at high neutron exposure. *J. Nucl. Mater.* **2000**, *276*, 123–142. https://doi.org/10.1016/S0022-3115(99)00225-1.
349. Zinkle, S.J.; Was, G.S. Materials challenges in nuclear energy. *Acta Mater.* **2013**, *61*, 735–758. https://doi.org/10.1016/j.actamat.2012.11.004.
350. Egami, T.; Guo, W.; Rack, P.D.; Nagase, T. Irradiation resistance of multicomponent alloys. *Metall. Mater. Trans. A Phys. Metall. Mater. Sci.* **2014**, *45*, 180–183. https://doi.org/10.1007/s11661-013-1994-2.
351. Tsai, M.H.; Yeh, J.W. High-entropy alloys: A critical review. *Mater. Res. Lett.* **2014**, *2*, 107–123. https://doi.org/10.1080/21663831.2014.912690.
352. Kasar, A.K.; Scalaro, K.; Menezes, P.L. Tribological properties of high-entropy alloys under dry conditions for a wide temperature range—a review. Materials (Basel). **2021**, *14*, 5814. https://doi.org/10.3390/ma14195814.
353. Menghani, J.; Vyas, A.; Patel, P.; Natu, H.; More, S. Wear, erosion and corrosion behavior of laser cladded high entropy alloy coatings—A review. *Mater. Today Proc.* **2020**, *38*, 2824–2829.
354. Ayyagari, A.; Hasannaeimi, V.; Grewal, H.S.; Arora, H.; Mukherjee, S. Corrosion, erosion andwear behavior of complex concentrated alloys: A review. *Metals* **2018**, *8*, 603, ISBN 1940565294.
355. Joseph, J.; Haghdadi, N.; Annasamy, M.; Kada, S.; Hodgson, P.D.; Barnett, M.R.; Fabijanic, D.M. On the enhanced wear resistance of CoCrFeMnNi high entropy alloy at intermediate temperature. *Scr. Mater.* **2020**, *186*, 230–235. https://doi.org/10.1016/j.scriptamat.2020.05.053.
356. Wang, H.; Ren, K.; Xie, J.; Zhang, C.; Tang, W. Friction and wear behavior of single-phase high-entropy alloyFeCoNiCrMn under MoS_2-oil lubrication. *Ind. Lubr. Tribol.* **2019**, *2019*, 2–9. https://doi.org/10.1108/ILT-08-2019-0303.
357. Xiao, J.K.; Tan, H.; Wu, Y.Q.; Chen, J.; Zhang, C. Microstructure and wear behavior of FeCoNiCrMn high entropy alloy coating deposited by plasma spraying. *Surf. Coat. Technol.* **2020**, *385*, 125430. https://doi.org/10.1016/j.surfcoat.2020.125430.
358. Jones, M.R.; Nation, B.L.; Wellington-Johnson, J.A.; Curry, J.F.; Kustas, A.B.; Lu, P.; Chandross, M.; Argibay, N. Evidence of Inverse Hall-Petch Behavior and Low Friction and Wear in High Entropy Alloys. *Sci. Rep.* **2020**, *10*, 14336. https://doi.org/10.1038/s41598-020-66701-7.
359. Zhu, S.; Zhang, B.; Tao, X.; Yu, Y.; Zhang, Z.; Wang, Z.; Lu, B. Microstructure and tribology performance of plasma clad intermetallics reinforced CoCrFeMnNi-based high-entropy alloy composite coatings. *Tribol. Trans.* **2020**, *64*, 264–274. https://doi.org/10.1080/10402004.2020.1832289.

360. Deng, G.; Tieu, A.K.; Su, L.; Wang, P.; Wang, L.; Lan, X.; Cui, S.; Zhu, H. Investigation into reciprocating dry sliding friction and wear properties of bulk CoCrFeNiMo high entropy alloys fabricated by spark plasma sintering and subsequent cold rolling processes: Role of Mo element concentration. *Wear* **2020**, *460–461*, 203440. https://doi.org/10.1016/j.wear.2020.203440.
361. Lindner, T.; Löbel, M.; Saborowski, E.; Rymer, L.M.; Lampke, T. Wear and corrosion behaviour of supersaturated surface layers in the high-entropy alloy systems CrMnFeCoNi and CrFeCoNi. *Crystals* **2020**, *10*, 110. https://doi.org/10.3390/cryst10020110.
362. Sha, C.; Zhou, Z.; Xie, Z.; Munroe, P. FeMnNiCoCr-based high entropy alloy coatings: Effect of nitrogen additions on microstructural development, mechanical properties and tribological performance. *Appl. Surf. Sci.* **2020**, *507*, 145101. https://doi.org/10.1016/j.apsusc.2019.145101.
363. Xiao, J.K.; Tan, H.; Chen, J.; Martini, A.; Zhang, C. Effect of carbon content on microstructure, hardness and wear resistance of CoCrFeMnNiCx high-entropy alloys. *J. Alloys Compd.* **2020**, *847*, 156533. https://doi.org/10.1016/j.jallcom.2020.156533.
364. Cheng, H.; Fang, Y.; Xu, J.; Zhu, C.; Dai, P.; Xue, S. Tribological properties of nano/ultrafine-grained $FeCoCrNiMnAl_x$ high-entropy alloys over a wide range of temperatures. *J. Alloys Compd.* **2020**, *817*, 153305. https://doi.org/10.1016/j.jallcom.2019.153305.
365. Joseph, J.; Haghdadi, N.; Shamlaye, K.; Hodgson, P.; Barnett, M.; Fabijanic, D. The sliding wear behaviour of CoCrFeMnNi and $Al_xCoCrFeNi$ high entropy alloys at elevated temperatures. *Wear* **2019**, *428–429*, 32–44. https://doi.org/10.1016/j.wear.2019.03.002.
366. Liu, X.; Yin, H.; Xu, Y. Microstructure, mechanical and tribological properties of Oxide Dispersion Strengthened high-entropy alloys. *Materials* **2017**, *10*, 1312. https://doi.org/10.3390/ma10111312.
367. Wang, J.; Zhang, B.; Yu, Y.; Zhang, Z.; Zhu, S.; Lou, X.; Wang, Z. Study of high temperature friction and wear performance of $(CoCrFeMnNi)_{85}Ti_{15}$ high-entropy alloy coating prepared by plasma cladding. *Surf. Coat. Technol.* **2020**, *384*, 125337. https://doi.org/10.1016/j.surfcoat.2020.125337.
368. Zhang, A.; Han, J.; Su, B.; Meng, J. A novel CoCrFeNi high entropy alloy matrix self-lubricating composite. *J. Alloys Compd.* **2017**, *725*, 700–710. https://doi.org/10.1016/j.jallcom.2017.07.197.
369. Geng, Y.; Chen, J.; Tan, H.; Cheng, J.; Yang, J.; Liu, W. Vacuum tribological behaviors of CoCrFeNi high entropy alloy at elevated temperatures. *Wear* **2020**, *456*, 203368. https://doi.org/10.1016/j.wear.2020.203368.
370. Zhang, A.; Han, J.; Su, B.; Li, P.; Meng, J. Microstructure, mechanical properties and tribological performance of CoCrFeNi high entropy alloy matrix self-lubricating composite. *Mater. Des.* **2017**, *114*, 253–263. https://doi.org/10.1016/j.matdes.2016.11.072.
371. Brownlie, F.; Hodgkiess, T.; Fanicchia, F. Erosion-corrosion behaviour of CoCrFeNiMo0.85 and Al0.5CoCrFeNi complex concentrated alloys produced by laser metal deposition. *Surf. Coatings Technol.* **2021,** *423,* 127634. https://doi.org/10.1016/j.surfcoat.2021.127634.
372. Zhang, M.; Zhang, W.; Liu, Y.; Liu, B.; Wang, J. FeCoCrNiMo high-entropy alloys prepared by powder metallurgy processing for diamond tool applications. *Powder Metall.* **2018**, *61*, 123–130. https://doi.org/10.1080/00325899.2018.1429044.
373. Huang, L.; Wang, X.; Jia, F.; Zhao, X.; Huang, B.; Ma, J.; Wang, C. Effect of Si element on phase transformation and mechanical properties for FeCoCrNiSix high entropy alloys. *Mater. Lett.* **2021**, *282*, 128809. https://doi.org/10.1016/j.matlet.2020.128809.
374. Cui, G.; Han, B.; Yang, Y.; Wang, Y.; Chunyang, H. Microstructure and tribological property of CoCrFeMoNi High entropy alloy treated by ion sulfurization. *J. Mater. Res. Technol.* **2020**, *9*, 2598–2609. https://doi.org/10.1016/j.jmrt.2019.12.090.
375. Li, T.; Liu, Y.; Liu, B.; Guo, W.; Xu, L. Microstructure and wear behavior of FeCoCrNiMo0.2 high entropy coatings prepared by air plasma spray and the high velocity oxy-fuel spray processes. *Coatings* **2017**, *7*, 5–8. https://doi.org/10.3390/coatings7090151.
376. Ji, X.; Zhao, J.; Wang, H.; Luo, C. Sliding wear of spark plasma sintered CrFeCoNiCu high entropy alloy coatings with MoS2 and WC additions. *Int. J. Adv. Manuf. Technol.* **2018**, *96*, 1685–1691. https://doi.org/10.1007/s00170-017-0794-z.
377. Verma, A.; Tarate, P.; Abhyankar, A.C.; Mohape, M.R.; Gowtam, D.S.; Deshmukh, V.P.; Shanmugasundaram, T. High temperature wear in $CoCrFeNiCu_x$ high entropy alloys: The role of Cu. *Scr. Mater.* **2019**, *161*, 28–31. https://doi.org/10.1016/j.scriptamat.2018.10.007.
378. Liu, D.; Zhao, J.; Li, Y.; Zhu, W.; Lin, L. Effects of boron content on microstructure and wear properties of $FeCoCrNiB_x$ high-entropy alloy coating by laser cladding. *Appl. Sci.* **2020**, *10*, 49. https://doi.org/10.3390/app10010049.
379. Jiang, H.; Jiang, L.; Qiao, D.; Lu, Y.; Wang, T.; Cao, Z.; Li, T. Effect of Niobium on Microstructure and Properties of the $CoCrFeNb_xNi$ High Entropy Alloys. *J. Mater. Sci. Technol.* **2017**, *33*, 712–717. https://doi.org/10.1016/j.jmst.2016.09.016.
380. Yu, Y.; He, F.; Qiao, Z.; Wang, Z.; Liu, W.; Yang, J. Effects of temperature and microstructure on the triblogical properties of $CoCrFeNiNb_x$ eutectic high entropy alloys. *J. Alloys Compd.* **2019**, *775*, 1376–1385. https://doi.org/10.1016/j.jallcom.2018.10.138.
381. Liu, X.; Zhou, S.; Xu, Y. Microstructure and tribological performance of $Fe_{50}Mn_{30}Co_{10}Cr_{10}$ high-entropy alloy based self-lubricating composites. *Mater. Lett.* **2018**, *233*, 142–145. https://doi.org/10.1016/j.matlet.2018.08.100.
382. Wang, J.; Yang, H.; Liu, Z.; Li, R.; Ruan, J.; Ji, S. Synergistic effects of WC nanoparticles and MC nanoprecipitates on the mechanical and tribological properties of $Fe_{40}Mn_{40}Cr_{10}Co_{10}$ medium-entropy alloy. *J. Mater. Res. Technol.* **2019**, *8*, 3550–3564. https://doi.org/10.1016/j.jmrt.2019.06.031.
383. Derimow, N.; MacDonald, B.E.; Lavernia, E.J.; Abbaschian, R. Duplex phase hexagonal-cubic multi-principal element alloys with high hardness. *Mater. Today Commun.* **2019**, *21*, 100658.
384. Guo, Y.; Li, C.; Zeng, M.; Wang, J.; Deng, P.; Wang, Y. In-situ TiC reinforced CoCrCuFeNiSi0.2 high-entropy alloy coatings designed for enhanced wear performance by laser cladding. *Mater. Chem. Phys.* **2020**, *242*, 122522. https://doi.org/10.1016/j.matchemphys.2019.122522.

385. Zhang, Y.; Han, T.; Xiao, M.; Shen, Y. Tribological behavior of diamond reinforced FeNiCoCrTi$_{0.5}$ carbonized high-entropy alloy coating. *Surf. Coat. Technol.* **2020**, *401*, 126233. https://doi.org/10.1016/j.surfcoat.2020.126233.
386. Erdoğan, A.; Gök, M.S.; Zeytin, S. Analysis of the high-temperature dry sliding behavior of CoCrFeNiTi$_{0.5}$Al$_x$ high-entropy alloys. *Friction* **2020**, *8*, 198–207. https://doi.org/10.1007/s40544-019-0278-2.
387. Liu, Y.; Xie, Y.; Cui, S.; Yi, Y.; Xing, X.; Wang, X.; Li, W. Effect of mo element on the mechanical properties and tribological responses of cocrfenimox high-entropy alloys. *Metals* **2021**, *11*, 486. https://doi.org/10.3390/met11030486.
388. Moazzen, P.; Toroghinejad, M.R.; Cavaliere, P. Effect of Iron content on the microstructure evolution, mechanical properties and wear resistance of Fe$_x$CoCrNi high-entropy alloy system produced via MA-SPS. *J. Alloys Compd.* **2021**, *870*, 159410. https://doi.org/10.1016/j.jallcom.2021.159410.
389. Yang, Y.; Ren, Y.; Tian, Y.; Li, K.; Zhang, W.; Shan, Q.; Tian, Y.; Huang, Q.; Wu, H. Microstructure and properties of FeCoCrNi-MoSi$_x$ high-entropy alloys fabricated by spark plasma sintering. *J. Alloys Compd.* **2021**, *884*, 161070. https://doi.org/10.1016/j.jallcom.2021.161070.
390. Li, Y.; Liang, H.; Nie, Q.; Qi, Z.; Deng, D.; Jiang, H.; Cao, Z. Microstructures and Wear Resistance of CoCrFeNi$_2$V$_{0.5}$Ti$_x$ High-Entropy Alloy Coatings Prepared by Laser Cladding. *Crystals* **2020**, *10*, 352. https://doi.org/10.3390/cryst10050352.
391. Islak, S.; Eski, Ö.; Koç, V.; Özorak, C. Wear properties and synthesis of crfenimoti high entropy alloy coatings produced by TIG process. *Indian J. Eng. Mater. Sci.* **2020**, *27*, 659–664. https://nopr.niscair.res.in/handle/123456789/55244.
392. Wen, X.; Cai, Z.; Yin, B.; Cui, X.; Zhang, X.; Jin, G. Tribological and Corrosion Properties of Ni-Cr-Co-Ti-V Multi-Principal Element Alloy Prepared by Vacuum Hot-Pressing Sintering. *Adv. Eng. Mater.* **2019**, *21*, 1801239. https://doi.org/10.1002/adem.201801239.
393. Wang, X.R.; Wang, Z.Q.; He, P.; Lin, T.S.; Shi, Y. Microstructure and wear properties of CuNiSiTiZr high-entropy alloy coatings on TC11 titanium alloy produced by electrospark—computer numerical control deposition process. *Surf. Coat. Technol.* **2015**, *283*, 156–161. https://doi.org/10.1016/j.surfcoat.2015.10.013.
394. Cheng, J.; Sun, B.; Ge, Y.; Hu, X.; Zhang, L.; Liang, X.; Zhang, X. Nb doping in laser-cladded Fe$_{25}$Co25Ni25(B0.7Si0.3)25 high entropy alloy coatings: Microstructure evolution and wear behavior. *Surf. Coat. Technol.* **2020**, *402*, 126321. https://doi.org/10.1016/j.surfcoat.2020.126321.
395. Yadav, S.; Sarkar, S.; Aggarwal, A.; Kumar, A.; Biswas, K. Wear and mechanical properties of novel (CuCrFeTiZn)$_{100-x}$Pb$_x$ high entropy alloy composite via mechanical alloying and spark plasma sintering. *Wear* **2018**, *410–411*, 93–109. https://doi.org/10.1016/j.wear.2018.05.023.
396. Gou, Q.; Xiong, J.; Guo, Z.; Liu, J.; Yang, L.; Li, X. Influence of NbC additions on microstructure and wear resistance of Ti(C,N)-based cermets bonded by CoCrFeNi high-entropy alloy. *Int. J. Refract. Met. Hard Mater.* **2020**, *94*, 105375. https://doi.org/10.1016/j.ijrmhm.2020.105375.
397. Yadav, S.; Kumar, A.; Biswas, K. Wear behavior of high entropy alloys containing soft dispersoids (Pb, Bi). *Mater. Chem. Phys.* **2018**, *210*, 222–232. https://doi.org/10.1016/j.matchemphys.2017.06.020.
398. Cui, Y.; Shen, J.; Manladan, S.M.; Geng, K.; Hu, S. Wear resistance of FeCoCrNiMnAl$_x$ high-entropy alloy coatings at high temperature. *Appl. Surf. Sci.* **2020**, *512*, 145736. https://doi.org/10.1016/j.apsusc.2020.145736.
399. Gwalani, B.; Torgerson, T.; Dasari, S.; Jagetia, A.; Nartu, M.S.K.K.Y.; Gangireddy, S.; Pole, M.; Wang, T.; Scharf, T.W.; Banerjee, R. Influence of fine-scale B2 precipitation on dynamic compression and wear properties in hypo-eutectic Al$_{0.5}$CoCrFeNi high-entropy alloy. *J. Alloys Compd.* **2021**, *853*, 157126. https://doi.org/10.1016/j.jallcom.2020.157126.
400. Chen, M.; Lan, L.; Shi, X.; Yang, H.; Zhang, M.; Qiao, J. The tribological properties of Al$_{0.6}$CoCrFeNi high-entropy alloy with the σ phase precipitation at elevated temperature. *J. Alloys Compd.* **2019**, *777*, 180–189. https://doi.org/10.1016/j.jallcom.2018.10.393.
401. Du, L.M.; Lan, L.W.; Zhu, S.; Yang, H.J.; Shi, X.H.; Liaw, P.K.; Qiao, J.W. Effects of temperature on the tribological behavior of Al$_{0.25}$CoCrFeNi high-entropy alloy. *J. Mater. Sci. Technol.* **2019**, *35*, 917–925. https://doi.org/10.1016/j.jmst.2018.11.023.
402. Chen, M.; Shi, X.H.; Yang, H.J.; Liaw, P.K.; Gao, M.C.; Hawk, J.A. Wear behavior of Al$_{0.6}$CoCrFeNi high-entropy alloy : Effect of environments. *J. Mater. Res.* **2018**, *33*, 3310–3320. https://doi.org/10.1557/jmr.2018.279.
403. Ji, X.; Duan, H.; Zhang, H.; Ma, J. Slurry Erosion Resistance of Laser Clad NiCoCrFeAl3 High-Entropy Alloy Coatings. *Tribol. Trans.* **2015**, *58*, 1119–1123. https://doi.org/10.1080/10402004.2015.1044148.
404. Haghdadi, N.; Guo, T.; Ghaderi, A.; Hodgson, P.D.; Barnett, M.R.; Fabijanic, D.M. The scratch behaviour of Al$_x$CoCrFeNi (x = 0.3 and 1.0) high entropy alloys. *Wear* **2019**, *428–429*, 293–301. https://doi.org/10.1016/j.wear.2019.03.026.
405. Fang, Y.; Chen, N.; Du, G.; Zhang, M.; Zhao, X.; Cheng, H.; Wu, J. High-temperature oxidation resistance, mechanical and wear resistance properties of Ti(C,N)-based cermets with Al0.3CoCrFeNi high-entropy alloy as a metal binder. *J. Alloys Compd.* **2020**, *815*, 152486. https://doi.org/10.1016/j.jallcom.2019.152486.
406. Wu, Y.H.; Yang, H.J.; Guo, R.P.; Wang, X.J.; Shi, X.H.; Liaw, P.K.; Qiao, J.W. Tribological behavior of boronized Al$_{0.1}$CoCrFeNi high-entropy alloys under dry and lubricated conditions. *Wear* **2020**, *460–461*, 203452. https://doi.org/10.1016/j.wear.2020.203452.
407. Nair, R.B.; Arora, H.S.; Boyana, A. V.; Saiteja, P.; Grewal, H.S. Tribological behavior of microwave synthesized high entropy alloy claddings. *Wear* **2019**, *436–437*, 203028. https://doi.org/10.1016/j.wear.2019.203028.
408. Kumar, S.; Rani, P.; Patnaik, A.; Pradhan, A.K.; Kumar, V. Effect of cobalt content on wear behaviour of Al$_{0.4}$FeCrNiCo$_x$ (x = 0, 0.25, 0.5, 1.0 mol) high entropy alloys tested under demineralised water with and without 3.5% NaCl solution. *Mater. Res. Express* **2019**, *6*, 0865b3. https://doi.org/10.1088/2053-1591/ab20b5.

409. Mu, Y.; Zhang, L.; Xu, L.; Prashanth, K.; Zhang, N.; Ma, X.; Jia, Y.; Xu, Y.; Jia, Y.; Wang, G. Frictional wear and corrosion behavior of AlCoCrFeNi high-entropy alloy coatings synthesized by atmospheric plasma spraying. *Entropy* **2020**, *22*, 740. https://doi.org/10.3390/e22070740.
410. Wu, M.; Chen, K.; Xu, Z.; Li, D.Y. Effect of Ti addition on the sliding wear behavior of AlCrFeCoNi high-entropy alloy. *Wear* **2020**, *462–463*, 203493. https://doi.org/10.1016/j.wear.2020.203493.
411. Zhao, D.; Yamaguchi, T.; Wang, W. Fabrication and wear performance of $Al_{0.8}$FeCrCoNi high entropy alloy coating on magnesium alloy by resistance seam welding. *Mater. Lett.* **2020**, *265*, 127250. https://doi.org/10.1016/j.matlet.2019.127250.
412. Kumar, S.; Patnaik, A.; Pradhan, A.K.; Kumar, V. Room temperature wear study of $Al_{0.4}$FeCrNiCo_x (x = 0, 0.25, 0.5, 1.0 mol) high-entropy alloys under oil lubricating conditions. *J. Mater. Res.* **2019**, *34*, 841–853. https://doi.org/10.1557/jmr.2018.499.
413. Li, Y.; Shi, Y. Phase assemblage and wear resistance of laser-cladding $Al_{0.8}$FeCoNiCr$Cu_{0.5}Si_x$ high-entropy alloys on aluminum. *Mater. Res. Express* **2020**, *7*, 086504. https://doi.org/10.1088/2053-1591/aba9f7.
414. Kafexhiu, F.; Podgornik, B.; Feizpour, D. Tribological behavior of as-cast and aged AlCoCrFeNi$_{2.1}$ CCA. *Metals* **2020**, *10*, 208. https://doi.org/10.3390/met10020208.
415. Miao, J.; Liang, H.; Zhang, A.; He, J.; Meng, J.; Lu, Y. Tribological behavior of an AlCoCrFeNi$_{2.1}$ eutectic high entropy alloy sliding against different counterfaces. *Tribol. Int.* **2021**, *153*, 106599. https://doi.org/10.1016/j.triboint.2020.106599.
416. Ye, F.; Yang, Y.; Lou, Z.; Feng, L.; Guo, L.; Yu, J. Microstructure and wear resistance of TiC reinforced AlCoCrFeNi$_{2.1}$ eutectic high entropy alloy layer fabricated by micro-plasma cladding. *Mater. Lett.* **2021**, *284*, 128859. https://doi.org/10.1016/j.matlet.2020.128859.
417. Wang, Y.; Yang, Y.; Yang, H.; Zhang, M.; Ma, S.; Qiao, J. Microstructure and wear properties of nitrided AlCoCrFeNi high-entropy alloy. *Mater. Chem. Phys.* **2018**, *210*, 233–239. https://doi.org/10.1016/j.matchemphys.2017.05.029.
418. Liu, Y.; Ma, S.; Gao, M.C.; Zhang, C.; Zhang, T.; Yang, H.; Wang, Z.; Qiao, J. Tribological Properties of AlCrCuFeNi$_2$ High-Entropy Alloy in Different Conditions. *Metall. Mater. Trans. A Phys. Metall. Mater. Sci.* **2016**, *47*, 3312–3321. https://doi.org/10.1007/s11661-016-3396-8.
419. Kong, D.; Guo, J.; Cui, X.; Zhang, X. Effect of superheating on microstructure and wear resistance of high-entropy Al1.8CrCuFeNi2 alloy. *Mater. Lett.* **2020**, *274*, 128021. https://doi.org/10.1016/j.matlet.2020.128021.
420. Wang, Y.; Yang, Y.; Yang, H.; Zhang, M.; Qiao, J. Effect of nitriding on the tribological properties of $Al_{1.3}$CoCuFeNi$_2$ high-entropy alloy. *J. Alloys Compd.* **2017**, *725*, 365–372. https://doi.org/10.1016/j.jallcom.2017.07.132.
421. Xiao, J.K.; Wu, Y.Q.; Chen, J.; Zhang, C. Microstructure and tribological properties of plasma sprayed FeCoNiCrSiAl_x high entropy alloy coatings. *Wear* **2020**, *448–449*, 203209. https://doi.org/10.1016/j.wear.2020.203209.
422. Liu, H.; Sun, S.; Zhang, T.; Zhang, G.; Yang, H.; Hao, J. Effect of Si addition on microstructure and wear behavior of AlCoCrFeNi high-entropy alloy coatings prepared by laser cladding. *Surf. Coat. Technol.* **2020**, *405*, 126522. https://doi.org/10.1016/j.surfcoat.2020.126522.
423. Hsu, C.Y.; Yeh, J.W.; Chen, S.K.; Shun, T.T. Wear resistance and high-temperature compression strength of Fcc CuCoNiCr$Al_{0.5}$Fe alloy with boron addition. *Metall. Mater. Trans. A Phys. Metall. Mater. Sci.* **2004**, *35A*, 1465–1469. https://doi.org/10.1007/s11661-004-0254-x.
424. Chen, M.R.; Lin, S.J.; Yeh, J.W.; Chen, S.K.; Huang, Y.S.; Tu, C.P. Microstructure and properties of Al0.5CoCrCuFeNiTix (x = 0-2.0) high-entropy alloys. *Mater. Trans.* **2006**, *47*, 1395–1401. https://doi.org/10.2320/matertrans.47.1395.
425. Löbel, M.; Lindner, T.; Mehner, T.; Lampke, T. Microstructure and wear resistance of AlCoCrFeNiTi high-entropy alloy coatings produced by HVOF. *Coatings* **2017**, *7*, 144. https://doi.org/10.3390/coatings7090144.
426. Kane, S.N.; Mishra, A.; Dutta, A.K. Preface: International Conference on Recent Trends in Physics (ICRTP 2016). *J. Phys. Conf. Ser.* **2016**, *755*, 011001. https://doi.org/10.1088/1742-6596/755/1/011001.
427. Wu, C.L.; Zhang, S.; Zhang, C.H.; Zhang, H.; Dong, S.Y. Phase evolution and cavitation erosion-corrosion behavior of FeCoCrAlNiTi_x high entropy alloy coatings on 304 stainless steel by laser surface alloying. *J. Alloys Compd.* **2017**, *698*, 761–770. https://doi.org/10.1016/j.jallcom.2016.12.196.
428. Erdogan, A.; Döleker, K.M.; Zeytin, S. Effect of laser re-melting on electric current assistive sintered CoCrFeNiAl_xTi_y high entropy alloys: Formation, micro-hardness and wear behaviors. *Surf. Coat. Technol.* **2020**, *399*, 126179. https://doi.org/10.1016/j.surfcoat.2020.126179.
429. Xin, B.; Zhang, A.; Han, J.; Su, B.; Meng, J. Tuning composition and microstructure by doping Ti and C for enhancing mechanical property and wear resistance of $Al_{0.2}Co_{1.5}$CrFe$Ni_{1.5}Ti_{0.5}$ high entropy alloy matrix composites. *J. Alloys Compd.* **2020**, *836*, 155273. https://doi.org/10.1016/j.jallcom.2020.155273.
430. Moravcikova-Gouvea, L.; Moravcik, I.; Omasta, M.; Veselý, J.; Cizek, J.; Minárik, P.; Cupera, J.; Záděra, A.; Jan, V.; Dlouhy, I. High-strength $Al_{0.2}Co_{1.5}$CrFe$Ni_{1.5}$Ti high-entropy alloy produced by powder metallurgy and casting: A comparison of microstructures, mechanical and tribological properties. *Mater. Charact.* **2020**, *159*, 110046. https://doi.org/10.1016/j.matchar.2019.110046.
431. Chuang, M.H.; Tsai, M.H.; Wang, W.R.; Lin, S.J.; Yeh, J.W. Microstructure and wear behavior of AlxCo 1.5CrFeNi1.5Tiy high-entropy alloys. *Acta Mater.* **2011**, *59*, 6308–6317. https://doi.org/10.1016/j.actamat.2011.06.041.
432. Liu, H.; Liu, J.; Li, X.; Chen, P.; Yang, H.; Hao, J. Effect of heat treatment on phase stability and wear behavior of laser clad AlCoCrFeNi$Ti_{0.8}$ high-entropy alloy coatings. *Surf. Coat. Technol.* **2020**, *392*, 125758. https://doi.org/10.1016/j.surfcoat.2020.125758.

433. Yu, Y.; Liu, W.M.; Zhang, T.B.; Li, J.S.; Wang, J.; Kou, H.C.; Li, J. Microstructure and tribological properties of AlCoCrFeNiTi0.5 high-entropy alloy in hydrogen peroxide solution. *Metall. Mater. Trans. A Phys. Metall. Mater. Sci.* **2014**, *45*, 201–207. https://doi.org/10.1007/s11661-013-1982-6.
434. Löbel, M.; Lindner, T.; Lampke, T. High-temperature wear behaviour of $AlCoCrFeNiTi_{0.5}$ coatings produced by HVOF. *Surf. Coatings Technol.* **2020**, *403*, 126379. https://doi.org/10.1016/j.surfcoat.2020.126379.
435. Chen, L.; Bobzin, K.; Zhou, Z.; Zhao, L.; Öte, M.; Königstein, T.; Tan, Z.; He, D. Wear behavior of HVOF-sprayed $Al_{0.6}$TiCrFeCoNi high entropy alloy coatings at different temperatures. *Surf. Coat. Technol.* **2019**, *358*, 215–222. https://doi.org/10.1016/j.surfcoat.2018.11.052.
436. Yu, Y.; Wang, J.; Yang, J.; Qiao, Z.; Duan, H.; Li, J.; Li, J.; Liu, W. Corrosive and tribological behaviors of AlCoCrFeNi-M high entropy alloys under 90 wt. % H2O2 solution. *Tribol. Int.* **2019**, *131*, 24–32. https://doi.org/10.1016/j.triboint.2018.10.012.
437. Yu, Y.; Wang, J.; Li, J.; Kou, H.; Duan, H.; Li, J.; Liu, W. Tribological behavior of AlCoCrCuFeNi and $AlCoCrFeNiTi_{0.5}$ high entropy alloys under hydrogen peroxide solution against different counterparts. *Tribol. Int.* **2015**, *92*, 203–210. https://doi.org/10.1016/j.triboint.2015.06.013.
438. Jin, G.; Cai, Z.; Guan, Y.; Cui, X.; Liu, Z.; Li, Y.; Dong, M.; zhang, D. High temperature wear performance of laser-cladded FeNiCoAlCu high-entropy alloy coating. *Appl. Surf. Sci.* **2018**, *445*, 113–122. https://doi.org/10.1016/j.apsusc.2018.03.135.
439. Zhu, T.; Wu, H.; Zhou, R.; Zhang, N.; Yin, Y.; Liang, L.; Liu, Y.; Li, J.; Shan, Q.; Li, Q.; et al. Microstructures and Tribological Properties of TiC Reinforced FeCoNiCuAl High-Entropy Alloy at Normal and Elevated Temperature. *Metals* **2020**, *10*, 387. https://doi.org/10.3390/met10030387.
440. Wu, J.M.; Lin, S.J.; Yeh, J.W.; Chen, S.K.; Huang, Y.S.; Chen, H.C. Adhesive wear behavior of AlxCoCrCuFeNi high-entropy alloys as a function of aluminum content. *Wear* **2006**, *261*, 513–519. https://doi.org/10.1016/j.wear.2005.12.008.
441. Yan, G.; Zheng, M.; Ye, Z.; Gu, J.; Li, C.; Wu, C.; Wang, B. In-situ Ti(C, N) reinforced AlCoCrFeNiSi-based high entropy alloy coating with functional gradient double-layer structure fabricated by laser cladding. *J. Alloys Compd.* **2021**, *886*, 161252. https://doi.org/10.1016/j.jallcom.2021.161252.
442. Li, Z.; Fu, P.; Hong, C.; Chang, F.; Dai, P. Tribological behavior of Ti(C, N)-TiB_2 composite cermets using FeCoCrNiAl high entropy alloys as binder over a wide range of temperatures. *Mater. Today Commun.* **2021**, *26*, 102095. https://doi.org/10.1016/j.mtcomm.2021.102095.
443. Kumar, A.; Chandrakar, R.; Chandraker, S.; Rao, K.R.; Chopkar, M. Microstructural and mechanical properties of AlCoCrCuFeNiSi_x (x = 0.3 and 0.6) high entropy alloys synthesized by spark plasma sintering. *J. Alloys Compd.* **2021**, *184*, 158193.
444. Xin, B.; Zhang, A.; Han, J.; Meng, J. Improving mechanical properties and tribological performance of $Al_{0.2}Co_{1.5}CrFeNi_{1.5}Ti_{0.5}$ high entropy alloys via doping Si. *J. Alloys Compd.* **2021**, *869*, 159122. https://doi.org/10.1016/j.jallcom.2021.159122.
445. Karakaş, M.S.; Günen, A.; Çarboğa, C.; Karaca, Y.; Demir, M.; Altınay, Y.; Erdoğan, A. Microstructure, some mechanical properties and tribocorrosion wear behavior of boronized $Al_{0.07}Co_{1.26}Cr_{1.80}Fe_{1.42}Mn_{1.35}Ni_{1.10}$ high entropy alloy. *J. Alloys Compd.* **2021**, *886*, 161222. https://doi.org/10.1016/j.jallcom.2021.161222.
446. Xin, B.; Zhang, A.; Han, J.; Meng, J. The tribological properties of carbon doped $Al_{0.2}Co_{1.5}CrFeNi_{1.5}Ti_{0.5}$ high entropy alloys. *Wear* **2021**, *484*, 204045. https://doi.org/10.1016/j.wear.2021.204045.
447. Zhao, P.; Li, J.; Lei, R.; Yuan, B.; Xia, M.; Li, X.; Zhang, Y. Investigation into microstructure, wear resistance in air and nacl solution of alcrconifectax high-entropy alloy coatings fabricated by laser cladding. *Coatings* **2021**, *11*, 358. https://doi.org/10.3390/coatings11030358.
448. Ghanbariha, M.; Farvizi, M.; Ebadzadeh, T.; Alizadeh Samiyan, A. Effect of ZrO_2 particles on the nanomechanical properties and wear behavior of AlCoCrFeNi–ZrO_2 high entropy alloy composites. *Wear* **2021**, *484–485*, 204032. https://doi.org/10.1016/j.wear.2021.204032.
449. Li, Y.; Shi, Y. Microhardness, wear resistance, and corrosion resistance of Al_xCrFeCoNiCu high-entropy alloy coatings on aluminum by laser cladding. *Opt. Laser Technol.* **2021**, *134*, 106632. https://doi.org/10.1016/j.optlastec.2020.106632.
450. Cai, Z.; Wang, Z.; Hong, Y.; Lu, B.; Liu, J.; Li, Y.; Pu, J. Improved tribological behavior of plasma-nitrided AlCrTiV and AlCrTiVSi high-entropy alloy films. *Tribol. Int.* **2021**, *163*, 107195. https://doi.org/10.1016/j.triboint.2021.107195.
451. Chandrakar, R.; Kumar, A.; Chandraker, S.; Rao, K.R.; Chopkar, M. Microstructural and mechanical properties of AlCoCrCuFeNiSi_x (x = 0 and 0.9) high entropy alloys. *Vacuum* **2021**, *184*, 109943. https://doi.org/10.1016/j.vacuum.2020.109943.
452. Erdogan, A.; Sunbul, S.E.; Icin, K.; Doleker, K.M. Microstructure, wear and oxidation behavior of AlCrFeNi$_x$ (X = Cu, Si, Co) high entropy alloys produced by powder metallurgy. *Vacuum* **2021**, *187*, 110143. https://doi.org/10.1016/j.vacuum.2021.110143.
453. Duan, H.; Wu, Y.; Hua, M.; Yuan, C.; Wang, D.; Tu, J.; Kou, H.; Li, J. Tribological properties of AlCoCrFeNiCu high-entropy alloy in hydrogen peroxide solution and in oil lubricant. *Wear* **2013**, *297*, 1045–1051. https://doi.org/10.1016/j.wear.2012.11.014.
454. Chen, M.R.; Lin, S.J.; Yeh, J.W.; Chen, S.K.; Huang, Y.S.; Chuang, M.H. Effect of vanadium addition on the microstructure, hardness, and wear resistance of $Al_{0.5}$CoCrCuFeNi high-entropy alloy. *Metall. Mater. Trans. A Phys. Metall. Mater. Sci.* **2006**, *37*, 1363–1369. https://doi.org/10.1007/s11661-006-0081-3.
455. Gu, Z.; Xi, S.; Mao, P.; Wang, C. Microstructure and wear behavior of mechanically alloyed powder $Al_xMo_{0.5}NbFeTiMn_2$ high entropy alloy coating formed by laser cladding. *Surf. Coat. Technol.* **2020**, *401*, 126244. https://doi.org/10.1016/j.surfcoat.2020.126244.
456. Hsu, C.Y.; Sheu, T.S.; Yeh, J.W.; Chen, S.K. Effect of iron content on wear behavior of AlCoCrFex$Mo_{0.5}$Ni high-entropy alloys. *Wear* **2010**, *268*, 653–659. https://doi.org/10.1016/j.wear.2009.10.013.

457. Liang, H.; Miao, J.; Gao, B.; Deng, D.; Wang, T.; Lu, Y.; Cao, Z.; Jiang, H.; Li, T.; Kang, H. Microstructure and tribological properties of $AlCrFe_2Ni_2W_{0.2}Mo_{0.75}$ high-entropy alloy coating prepared by laser cladding in seawater, NaCl solution and deionized water. *Surf. Coat. Technol.* **2020**, *400*, 126214. https://doi.org/10.1016/j.surfcoat.2020.126214.
458. Qiu, X.W.; Liu, C.G. Microstructure and properties of $Al_2CrFeCoCuTiNi_x$ high-entropy alloys prepared by laser cladding. *J. Alloys Compd.* **2013**, *553*, 216–220. https://doi.org/10.1016/j.jallcom.2012.11.100.
459. Kanyane, L.R.; Popoola, A.P.; Malatji, N. Influence of Sintering Temperature on Microhardness and Tribological Properties of Equi-Atomic Ti-Al-Mo-Si-W Multicomponent Alloy. *IOP Conf. Ser. Mater. Sci. Eng.* **2019**, *538*, 012009. https://doi.org/10.1088/1757-899X/538/1/012009.
460. Huang, C.; Zhang, Y.; Vilar, R.; Shen, J. Dry sliding wear behavior of laser clad TiVCrAlSi high entropy alloy coatings on Ti-6Al-4V substrate. *Mater. Des.* **2012**, *41*, 338–343. https://doi.org/10.1016/j.matdes.2012.04.049.
461. Zhang, H.X.; Dai, J.J.; Sun, C.X.; Li, S.Y. Microstructure and wear resistance of TiAlNiSiV high-entropy laser cladding coating on Ti-6Al-4V. *J. Mater. Process. Technol.* **2020**, *282*, 116671. https://doi.org/10.1016/j.jmatprotec.2020.116671.
462. Lin, Y.C.; Cho, Y.H. Elucidating the microstructure and wear behavior for multicomponent alloy clad layers by in situ synthesis. *Surf. Coat. Technol.* **2008**, *202*, 4666–4672. https://doi.org/10.1016/j.surfcoat.2008.03.033.
463. Yadav, S.; Aggrawal, A.; Kumar, A.; Biswas, K. Effect of TiB2 addition on wear behavior of $(AlCrFeMnV)_{90}Bi_{10}$ high entropy alloy composite. *Tribol. Int.* **2019**, *132*, 62–74. https://doi.org/10.1016/j.triboint.2018.11.025.
464. Bhardwaj, V.; Zhou, Q.; Zhang, F.; Han, W.; Du, Y.; Hua, K.; Wang, H. Effect of Al addition on the microstructure, mechanical and wear properties of TiZrNbHf refractory high entropy alloys. *Tribol. Int.* **2021**, *160*, 107031. https://doi.org/10.1016/j.triboint.2021.107031.
465. Zhao, P.; Li, J.; Zhang, Y.; Li, X.; Xia, M.M.; Yuan, B.G. Wear and high-temperature oxidation resistances of $AlNbTaZr_x$ high-entropy alloys coatings fabricated on Ti6Al4V by laser cladding. *J. Alloys Compd.* **2021**, *862*, 158405. https://doi.org/10.1016/j.jallcom.2020.158405.
466. Tüten, N.; Canadinc, D.; Motallebzadeh, A.; Bal, B. Microstructure and tribological properties of TiTaHfNbZr high entropy alloy coatings deposited on Ti–6Al–4V substrates. *Intermetallics* **2019**, *105*, 99–106. https://doi.org/10.1016/j.intermet.2018.11.015.
467. Pole, M.; Sadeghilaridjani, M.; Shittu, J.; Ayyagari, A.; Mukherjee, S. High temperature wear behavior of refractory high entropy alloys based on 4-5-6 elemental palette. *J. Alloys Compd.* **2020**, *843*, 156004. https://doi.org/10.1016/j.jallcom.2020.156004.
468. Ye, Y.X.; Liu, C.Z.; Wang, H.; Nieh, T.G. Friction and wear behavior of a single-phase equiatomic TiZrHfNb high-entropy alloy studied using a nanoscratch technique. *Acta Mater.* **2018**, *147*, 78–89. https://doi.org/10.1016/j.actamat.2018.01.014.
469. Pogrebnjak, A.D.; Yakushchenko, I. V.; Abadias, G.; Chartier, P.; Bondar, O. V.; Beresnev, V.M.; Takeda, Y.; Sobol', O. V.; Oyoshi, K.; Andreyev, A.A.; et al. The effect of the deposition parameters of nitrides of high-entropy alloys (TiZrHfVNb)N on their structure, composition, mechanical and tribological properties. *J. Superhard Mater.* **2013**, *35*, 356–368. https://doi.org/10.3103/S106345761306004X.
470. Gong, P.; Li, F.; Deng, L.; Wang, X.; Jin, J. Research on nano-scratching behavior of TiZrHfBeCu(Ni) high entropy bulk metallic glasses. *J. Alloys Compd.* **2020**, *817*, 153240. https://doi.org/10.1016/j.jallcom.2019.153240.
471. Zhao, Y.Y.; Ye, Y.X.; Liu, C.Z.; Feng, R.; Yao, K.F.; Nieh, T.G. Tribological behavior of an amorphous $Zr_{20}Ti_{20}Cu_{20}Ni_{20}Be_{20}$ high-entropy alloy studied using a nanoscratch technique. *Intermetallics* **2019**, *113*, 1065601. https://doi.org/10.1016/j.intermet.2019.106561.
472. Jhong, Y.S.; Huang, C.W.; Lin, S.J. Effects of CH4 flow ratio on the structure and properties of reactively sputtered (CrNbSiTiZr)C_x coatings. *Mater. Chem. Phys.* **2018**, *210*, 348–352. https://doi.org/10.1016/j.matchemphys.2017.08.002.
473. Mathiou, C.; Poulia, A.; Georgatis, E.; Karantzalis, A.E. Microstructural features and dry—Sliding wear response of MoTaNbZrTi high entropy alloy. *Mater. Chem. Phys.* **2018**, *210*, 126–135. https://doi.org/10.1016/j.matchemphys.2017.08.036.
474. Petroglou, D.; Poulia, A.; Mathiou, C.; Georgatis, E.; Karantzalis, A.E. A further examination of MoTaxNbVTi (x = 0.25, 0.50, 0.75 and 1.00 at.%) high-entropy alloy system: Microstructure, mechanical behavior and surface degradation phenomena. *Appl. Phys. A Mater. Sci. Process.* **2020**, *126*, 364. https://doi.org/10.1007/s00339-020-03566-7.
475. Poulia, A.; Georgatis, E.; Lekatou, A.; Karantzalis, A.E. Microstructure and wear behavior of a refractory high entropy alloy. *Int. J. Refract. Met. Hard Mater.* **2016**, *57*, 50–63. https://doi.org/10.1016/j.ijrmhm.2016.02.006.
476. Poulia, A.; Georgatis, E.; Lekatou, A.; Karantzalis, A. Dry-Sliding Wear Response of MoTaWNbV High Entropy Alloy. *Adv. Eng. Mater.* **2017**, *19*, 1600535. https://doi.org/10.1002/adem.201600535.
477. Poulia, A.; Georgatis, E.; Karantzalis, A. Evaluation of the Microstructural Aspects, Mechanical Properties and Dry Sliding Wear Response of MoTaNbVTi Refractory High Entropy Alloy. *Met. Mater. Int.* **2019**, *25*, 1529–1540. https://doi.org/10.1007/s12540-019-00283-6.
478. Alvi, S.; Akhtar, F. High temperature tribology of CuMoTaWV high entropy alloy. *Wear* **2019**, *426–427*, 412–419. https://doi.org/10.1016/j.wear.2018.12.085.
479. Hua, N.; Wang, W.; Wang, Q.; Ye, Y.; Lin, S.; Zhang, L.; Guo, Q.; Brechtl, J.; Liaw, P.K. Mechanical, corrosion, and wear properties of biomedical Ti–Zr–Nb–Ta–Mo high entropy alloys. *J. Alloys Compd.* **2021**, *861*, 157997. https://doi.org/10.1016/j.jallcom.2020.157997.
480. Gu, Z.; Peng, W.; Guo, W.; Zhang, Y.; Hou, J.; He, Q.; Zhao, K.; Xi, S. Design and characterization on microstructure evolution and properties of laser-cladding $Ni_{1.5}CrFeTi_2B_{0.5}Mo_x$ high-entropy alloy coatings. *Surf. Coat. Technol.* **2021**, *408*, 126793. https://doi.org/10.1016/j.surfcoat.2020.126793.

481. Xin, B.; Yu, Y.; Zhou, J.; Wang, L.; Ren, S. Effect of copper molybdate on the lubricating properties of NiCrAlY laser clad coating at elevated temperatures. *Surf. Coat. Technol.* **2017**, *313*, 328–336. https://doi.org/10.1016/j.surfcoat.2017.01.098.
482. Archard, J.F. Contact and Rubbing of Flat Surfaces. *J. Appl. Phys.* **1953**, *24*, 981–988. https://doi.org/10.1063/1.1721448.
483. Mohan, S.; Agarwala, V.; Ray, S. Friction characteristics of stir-cast Al-Pb alloys. *Wear* **1992**, *157*, 9–17.
484. Ding, C.H.; Li, P.L.; Ran, G.; Tian, Y.W.; Zhou, J.N. Tribological property of self-lubricating PM304 composite. *Wear* **2007**, *262*, 575–581. https://doi.org/10.1016/j.wear.2006.07.003.